FEDERAL UNIVERSITY OF SANTA MARIA
TECHNOLOGY CENTER
POST-GRADUATION PROGRAM
IN ELECTRICAL ENGINEERING

Jelais Jean Francois

HIGH-VOLTAGE GAIN CONVERTERS USING COUPLED INDUCTOR AND RESONANT CELLS

Santa Maria, RS
2022

Jelais Jean Francois

HIGH-VOLTAGE GAIN CONVERTERS USING COUPLED INDUCTOR AND RESONANT CELLS

Dissertation submitted to the Post-Graduation Program in Electrical Engineering, Area of concentration in Energy Processing of Federal University of Santa Maria (UFSM) to obtain the **Master's Degree in Electrical Engineering**.

Advisor: Prof. Dr. António Manuel Santos Spencer Andrade
Co-Advisor: Prof. Dr. Fábio Ecke Bisogno

Santa Maria, RS
2022

Ficha catalográfica elaborada através do Programa de Geração Automática da
Biblioteca Central da UFSM, com os dados fornecidos pelo(a) autor(a).

```
Jean Francois, Jelais
   High-Voltage Gain Converters using Coupled Inductor and
Resonant Cells / Jelais Jean Francois - 2022
   113 p.; 30 cm

   Orientador:  António Manuel Santos Spencer Andrade
   Coorientador:  Fábio Ecke Bisogno
   Dissertation defense - Universidade Federal de Santa
Maria, Technology Center, Post-Graduation Program in
Electrical Engineering, RS, 2022

   1.  Electrical Engineering 2.  Power Electronic 3.
Renewable Energy 4.  ZVS Boost Flyback Converter I. ANDRADE,
NTÓNIO MANUEL SANTOS SPENCER II. Title.
```

Adress: Rua João Atilio Zampiere, Nº 631, Camobi, Santa Maria, RS, Brasil, CEP: 97105-490.
Email Adress: jelais-francois.jf@acad.ufsm.br

Jelais Jean Francois

HIGH-VOLTAGE GAIN CONVERTERS USING COUPLED INDUCTOR AND RESONANT CELLS

Dissertation submitted to the Post-Graduation Program in Electrical Engineering, Area of concentration in Energy Processing of Federal University of Santa Maria (UFSM) to obtain the **Master's Degree in Electrical Engineering**.

Approved on September 15 , 2022:

António Manuel Santos Spencer Andrade, Dr. (UFSM)
(Chairman/Advisor)

Fábio Ecke Bisogno, Dr. (UFSM)
(Co-Advisor)

Ronaldo Antonio Guisso, Dr. (Universidade Feevale-FEEVALE)

Mauricio Mendes da Silva, Dr. (Universidad Tecnológica del Uruguay-UTEC)

Santa Maria, RS
2022

ACKNOWLEDGMENTS

I thank all those who have contributed along this way, especially :

To God, to whom I owe my life.

To my wife Taira Jean, the love of my life, for the love, care and unconditional support in difficult moments.

To my father, Chariles Jean Francois, who gave me a healthy education and everything I needed since my childhood.

To my older sister Jerdine Chery, who always supports me in difficult moments.

To my dear aunts Hennecita Predesca and Emanise Chery.

To my cousins Alifaite Jean Francois, Lebens Ledix and Mona Jean Francois, with whom I am since the childhood and who will always be with me.

To my Advisor and Co-Advisor António Manuel Santos Spencer Andrade and Fábio Ecke Bisogno, for their guidance, patience and teachings that have made possible the development of this work.

To my Haitian friends and colleagues Lendy Louidor and Sylvain René, my gratitude for the moments of support and relax.

To the colleagues of the Power and Control Electronics Group (GEPOC) of UFSM, Ademir Toebe and Tiago Faistel for their availability whenever I needed help.

To the Post-Graduation Program in Electrical Engineering(PPGEE), SAI-UFSM, professors of the Laboratório Entrelínguas of UFSM, Federal University of Santa Maria (UFSM), for the opportunity received, the fair treatment during these learning years.

This work is supported by Coordenação de Aperfeiçoamento de Pessoal de Nível Superior - Brazil (CAPES/PROEX) - Funding Code 001 and Conselho National de Desenvolvimento Cientifico e tecnologico (CNPq), No. 425155/2018-8.

ABSTRACT

HIGH-VOLTAGE GAIN CONVERTERS USING COUPLED INDUCTOR AND RESONANT CELLS

Author: Jelais Jean Francois
Advisor: António Manuel Santos Spencer Andrade
Co-advisor: Fábio Ecke Bisogno

A high Step-Up Quadratic Boost Flyback Converter is presented in this work. This converter is designing by combining A boost converter and a flyback converter in stacked connection, the voltage gain can be adjusted by varying the turn ratio of the coupled inductor. A two components resonant cell is used to achieve Zero Voltage Switching at turn ON and turn OFF switching and to maintain Zero Current Switching on semiconductor diodes. To prevent reverse resonant inductor current flowing back to the source, an input boost cell is used, which allows not only to make higher the voltage gain but also to make better the efficiency. The prototype works with a conversion rate of over ten times of the input voltage and the efficiency is over 88% when using a 200W PV module.

Keywords: DC-DC converter, electrical engineering, quadratic boost flyback, renewable energy, zero current switching, zero voltage switching.

RESUMO

CONVERSORES DE ALTO GANHO DE TENSÃO USANDO INDUTOR ACOPLADO E CÉLULAS RESSONANTES

Autor: Jelais Jean Francois
Orientador: António Manuel Santos Spencer Andrade
Coorientador: Fábio Ecke Bisogno

Neste trabalho um conversor quadrático de alto ganho de tensão é apresentado. Este conversor está sendo projetado combinando um conversor boost e um conversor flyback em conexão empilhada, o ganho de tensão pode ser ajustado variando a relação de espiras do indutor acoplado. Uma célula ressonante composta de dois componentes é usada para obter a Comutação de Tensão Zero ao ligar e desligar da chave e para manter a Comutação de Corrente Zero nos diodos semicondutores. Para evitar que a corrente reversa do indutor ressonante volte à fonte, é usado uma célula boost na entrada, que permite não somente aumentar o ganho de tensão, mas também melhorar a eficiência. O protótipo funciona com uma taxa de conversão de mais de dez vezes da tensão de entrada e a eficiência é maior do que 88% quando se utiliza um módulo PV de 200W.

Palavras-chave: Conversor CC-CC, engenharia elétrica, quadrático boost flyback, energia renovável, comutação de corrente zero, comutação de tensão zero.

LIST OF FIGURES

LIST OF TABLES

LIST OF ACRONYMS AND ABBREVIATIONS

AC	Alternating Current
BJT	Bipolar Junction Transistor
CCM	Continuous Conduction Mode
CSP	Concentrating Solar Power
DC	Direct Current
DCM	Discontinuous Conduction Mode
DNI	Direct Normal Irradiation
EDH	Electricity of Haiti
EMI	Electromagnetic Interference
ESR	Equivalent Series Resistance
IGBT	Insulated Gate Bipolar Transistor
MIC	Module-Integrated Converter
MOSFET	Metal Oxide Semiconductor Field Effect Transistor
MPPT	Maximum Power Point Tracking
NRECA	National Rural Electric Cooperative Association
PV	Photovoltaic
PWM	Pulse Width Modulation
QZVSBFC	Quadratic Zero Voltage Switching Boost Flyback Converter
SHC	Solar Heating and Cooling
ZCS	Zero Current Switching
ZVS	Zero Voltage Switching

LIST OF SYMBOLS

A	Normalized Frequency
C_b	Output Boost capacitor
C_f	Output Flyback capacitor
C_r	Resonant capacitor
D_b	Boost diode
f_r	Resonant frequency
f_s	Switching frequency
h	Initaial switch and inductor current
L_r	Resonant inductor
M	Voltage gain
N	Turn ratio of the coupled inductor
P_i	Input power
V_i	Input voltage
V_o	Output voltage
W_r	Angular Frequency

CONTENTS

1 INTRODUCTION

This chapter presents an overview of fossil fuels and various greenhouse gases emitted to the atmosphere, of energetic sector (Generation, consumption) in Haiti and in the world. It highlights renewable energies and presents an analysis of photovoltaic energy, different structures of microinverters and Soft-Switching High Step-Up DC-DC converters.

1.1 OVERVIEW OF GLOBAL ENERGY CONSUMPTION, GENERATION AND CARBONE DIOXIDE EMISSIONS

In the last years, global warming has been a major issue due to the continuous growth of greenhouse gas emissions from different sources. Due to the world's continued reliance on fossil fuels as an energy source, greenhouse gas concentrations are steadily increasing in the atmosphere and warming the globe, It has been previously estimated that the global average temperature will increase between 1.4 and 5.8 °C by 2100 (WILLIAMS; JACKSON; KUTZBACH, 2007). The main cause of global warming is the excessive use of fossil fuels as an energy source. Gases such as carbon dioxide (CO2), chlorofluorocarbons (CFCs), methane (CH4), and nitrous oxide (N2O) are the main contributors to the greenhouse effect with an emission percentage of 55%, 24%, 15%, and 6% respectively (DEMIRBAS, 2005). Figure 1.1 shows the carbon dioxide emissions between 2010 and 2020 according to the British Petroleum annual report in 2021 (BRITISH PETROLEUM, 2021). During this period, carbon emissions to the atmosphere increase by 3.1%, with 31.045 Gt of carbon dioxide in 2010 and 32.018 Gt in 2020.

For many years, United States was the largest contributor, but recently, China, in the midst of industrial revolution, has become the largest CO2 emitter in the world, with 9899.3 million tons in 2020, compared to 4457.2 million tons for United States and 417.5 tons for Brazil. China alone emits about twice more carbon dioxide into the atmosphere than the United States in 2020. Figure 1.2 presents an histogram of carbon dioxide emission by region between 2010 and 2020. According to the data of (BRITISH PETROLEUM, 2021), it can be seen that the Asia Pacific region dominates with an estimated emission of 16787.4 million tonnes of carbon dioxide, which represents a growth rate of 20.11% compared to 2010, followed by Europe with an emission of 3596.8 million tonnes of CO_2, representing a decreasing rate of -23.1% compared to 2010, then come North, South and Central America, the Middle East, Independent Commonwealth States and Africa.

Global energy demand is increasing rapidly, as a result of population and economic growth, particularly in emerging market economies (OECD, 2011). Given the increasing number of consumers needing ever more energy resources, energy security issues will emerge. During the 20th century, the world's population increased by a factor of 4,

Figure 1.1 – Emission of carbon dioxide in the world

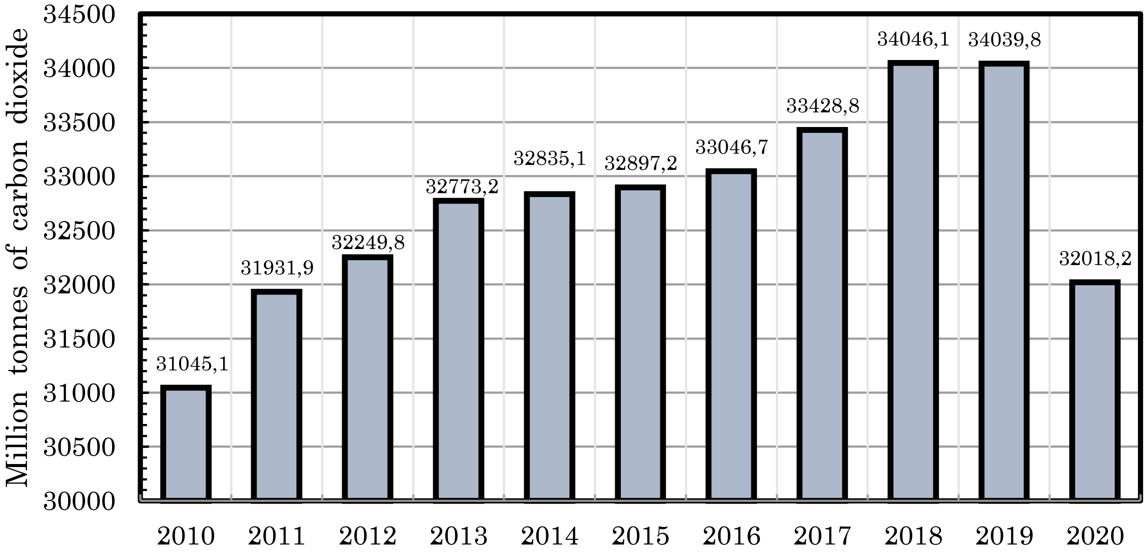

Source: Adapted from ((BRITISH PETROLEUM, 2021))

Figure 1.2 – Emission of carbon dioxide by region.

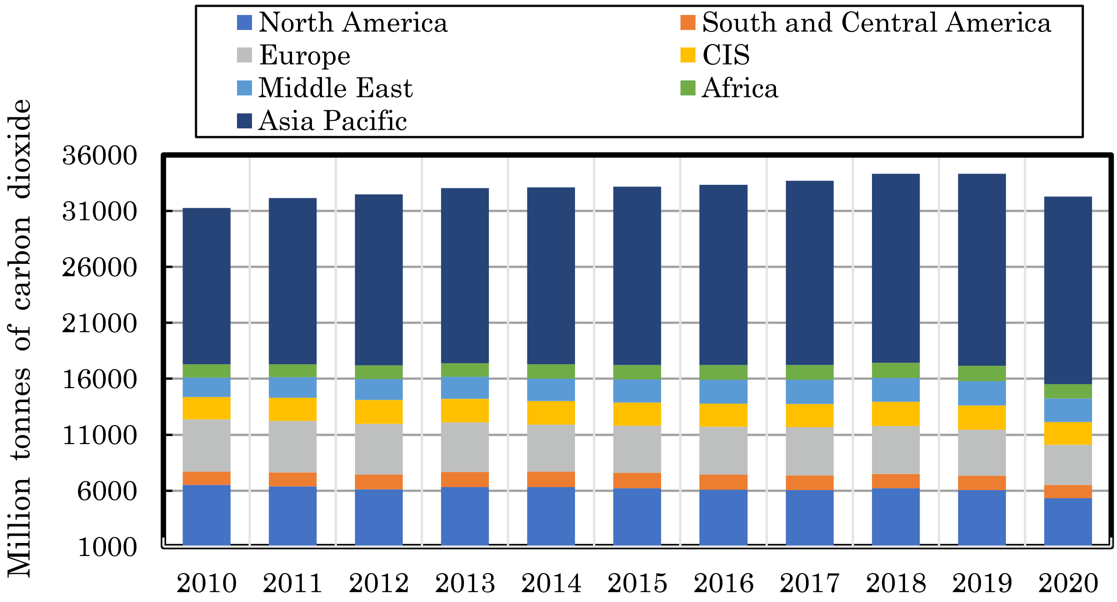

Source: Adapted from (BRITISH PETROLEUM, 2021)

economic production 22 times and fossil fuel consumption 14 times (UNEP, 2011). One of the challenges is to meet the energy and food demands of 9 billion people by 2050. Without new measures, a global economy 4 times larger than today would need to consume 80% more energy by 2050 (OECD, 2012). As people get richer and populations grow, energy demand increases in many countries around the world. Without offsetting this increased demand with improvements in energy efficiency, our global energy consumption will continue to grow year after year (Hannah Ritchie and Max Roser, 2020). Rising energy consumption creates a greater challenge to transition energy systems from fossil fuels to low-carbon energy sources: new low-carbon energy must meet this additional demand and attempt to replace existing fossil fuels in the energy mix.

Figure 1.3 – Global energy consumption between 2010 and 2020.

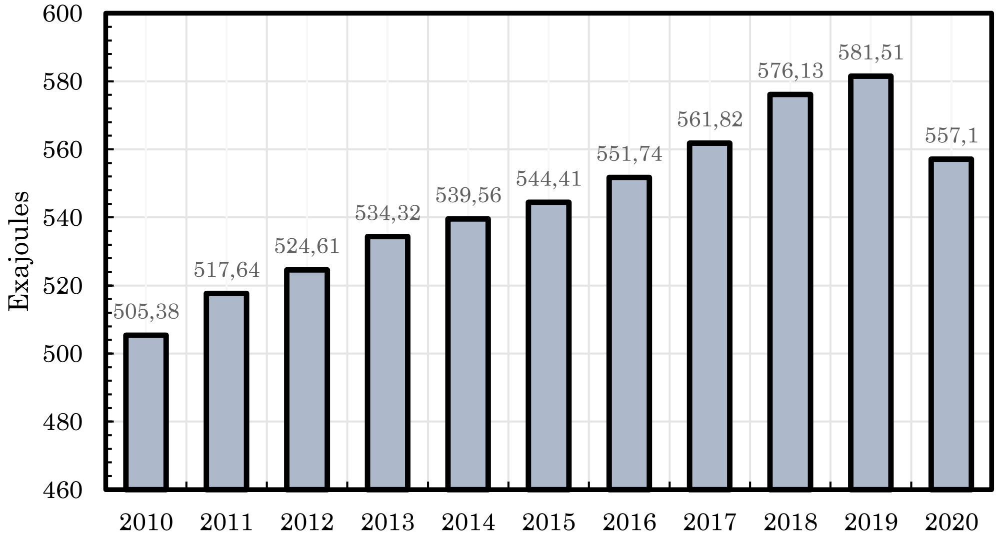

Source: Adapted from (BRITISH PETROLEUM, 2021)

Figure 1.3 shows the evolution of Global primary energy consumption between 2010 and 2020, Figure 1.4 shows the world energy consumption by fuel in 2019 and 2020. It is found that the world energy consumption grows by 10.23% between 2010 and 2020, yet slows down around 4 to 9% between 2019 and 2020 during the increased period of the Covid-19 pandemic. Electricity has become an indispensable part of human life, absolutely essential to modern life and business. Its disruption can cause major losses and create devastations in cities and urban centers; its disturbance, even transient, can cause enormous inconvenience, for this reason, the generation, distribution and utilization of electrical energy remains one of the most challenging and exciting areas of electrical engineering (KHATIB, 1996). The amazing technological developments of the 21st century are highly dependent on a safe, reliable, and economical supply of electrical energy. (GRIGSBY; HARLOW; MCDONALD, 2011). During the outbreak of the new coronavirus COVID-19 around the world in early 2020, human activities were significantly changed, almost all regions and sectors of the world were affected by the massive destruction of the disease (DABO et al., 2020). Due to some lockdown, social distancing, travel ban measures taken by authorities of various countries to prevent the spread of the disease, electricity industry is deeply affected, big factories and commercial electricity consumer are forced to shut down or switch to minimum operation levels. As a result, residential load is beginning to account for a larger proportion of global energy consumption. As a result,

Figure 1.4 – Global energy consumption by fuel in: (a) 2019 (b) 2020

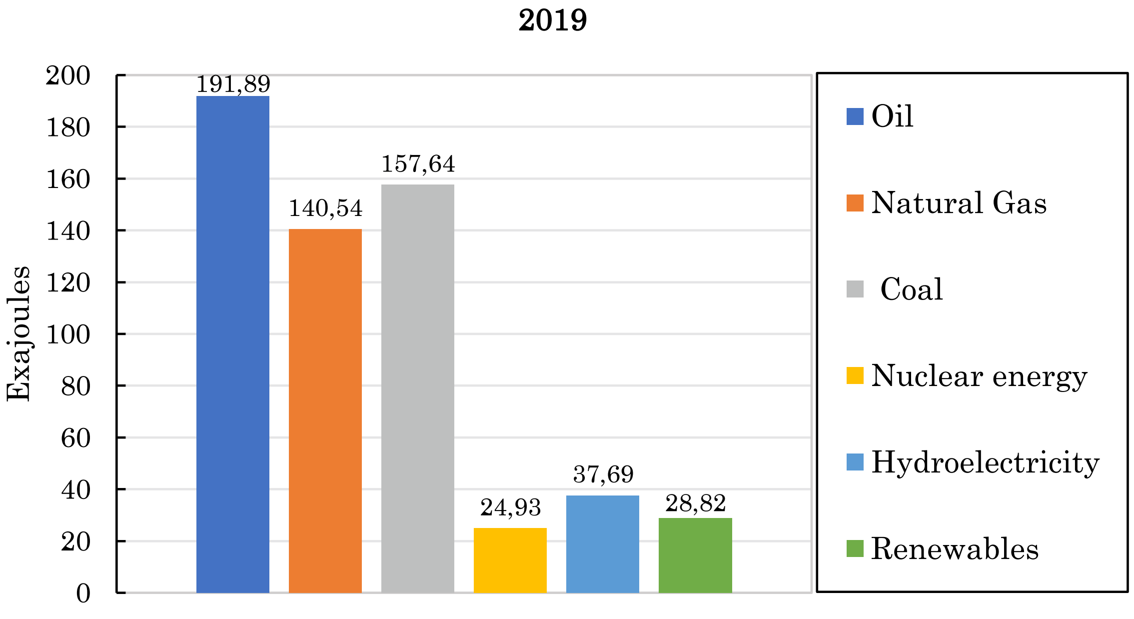

(a)

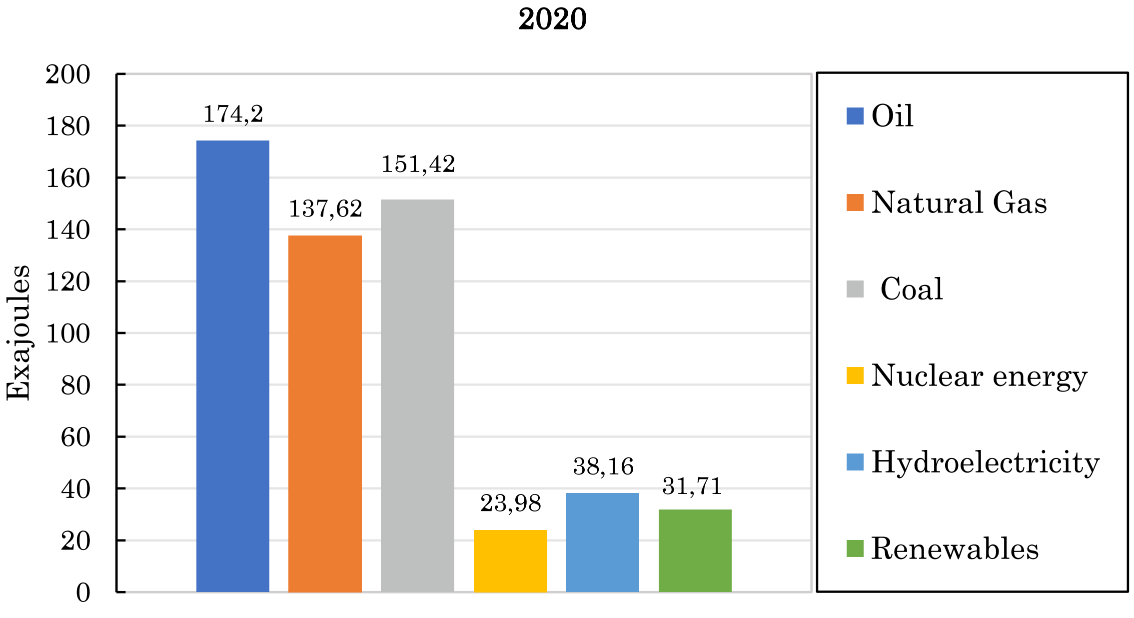

(b)

Source: Adapted from (BRITISH PETROLEUM, 2021)

electricity demand dropped dramatically by 4 to 5% in 2020 compared to 2019 according to (BRITISH PETROLEUM, 2021). Figure 1.5 shows energy production by region between 2010 and 2020 and Figure 1.6 shows the world's energy production by fuel oil in 2019 and 2020 (BRITISH PETROLEUM, 2021), it is observed that renewable production has increased while total electricity generation has decreased. This unbalance is due to the strong influence of the electricity market, the emergence of hybrid electric vehicles which; a) have lower net CO2 emissions than traditional gasoline engine cars, c) can use existing

Figure 1.5 – Global Electricity Generation by region.

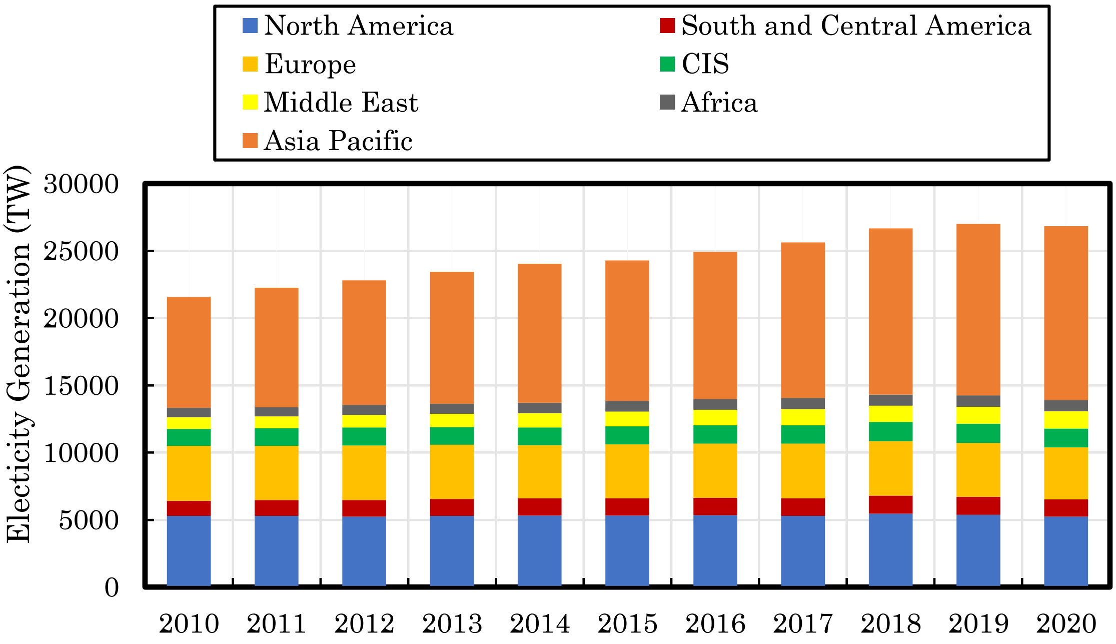

Source: Adapted from (BRITISH PETROLEUM, 2021)

electrical infrastructure for charging, d) have the potential to drive the shift to renewable energy sources and make the transportation sector more sustainable (DICKERMAN; HARRISON, 2010). According to Figure 1.5, Global Electricity Generation decreased by 0.65% between 2019 and 2020, the first decline in Electricity Generation since 2010. This decline is largely due to oil (-7.61%), followed by coal (-4.12%), Nuclear Energy (-3.45%), Natural Gas (-0.9%), Generation of all fuels decreased, apart from renewables (+12.82%) and hydroelectricity (+1.63%).

1.2 OVERVIEW OF ENERGETIC SECTOR IN HAITI

Haiti is located in the center of the Caribbean region next to Central America, covering the western part of Hispaniola Island with a total area of 27,750 km2 and is a direct neighbor of Dominican Republic. 75% of the country is mountainous and crossed by several mountain ranges, some of which reach more than 2,500 meters in altitude. Haiti is facing serious problems leading to accelerated degradation of its environment, degradation of natural capital and food insecurity, its forest cover and its natural resources. This situation is characterized by issues of environmental governance, rainfall variation, lack of environmental services at the watershed level, and food security.

Regarding to the energetic sector in Haiti, the structure of energy consumption is the following: firewood (55%), charcoal (16%), hydroelectricity (5%), bagasse (4%) and imported petroleum products (20%) (RINA, 2019). In fact, the energy sector is one

Figure 1.6 – Global Electricity Generation by fuel in: (a) 2019 (b) 2020

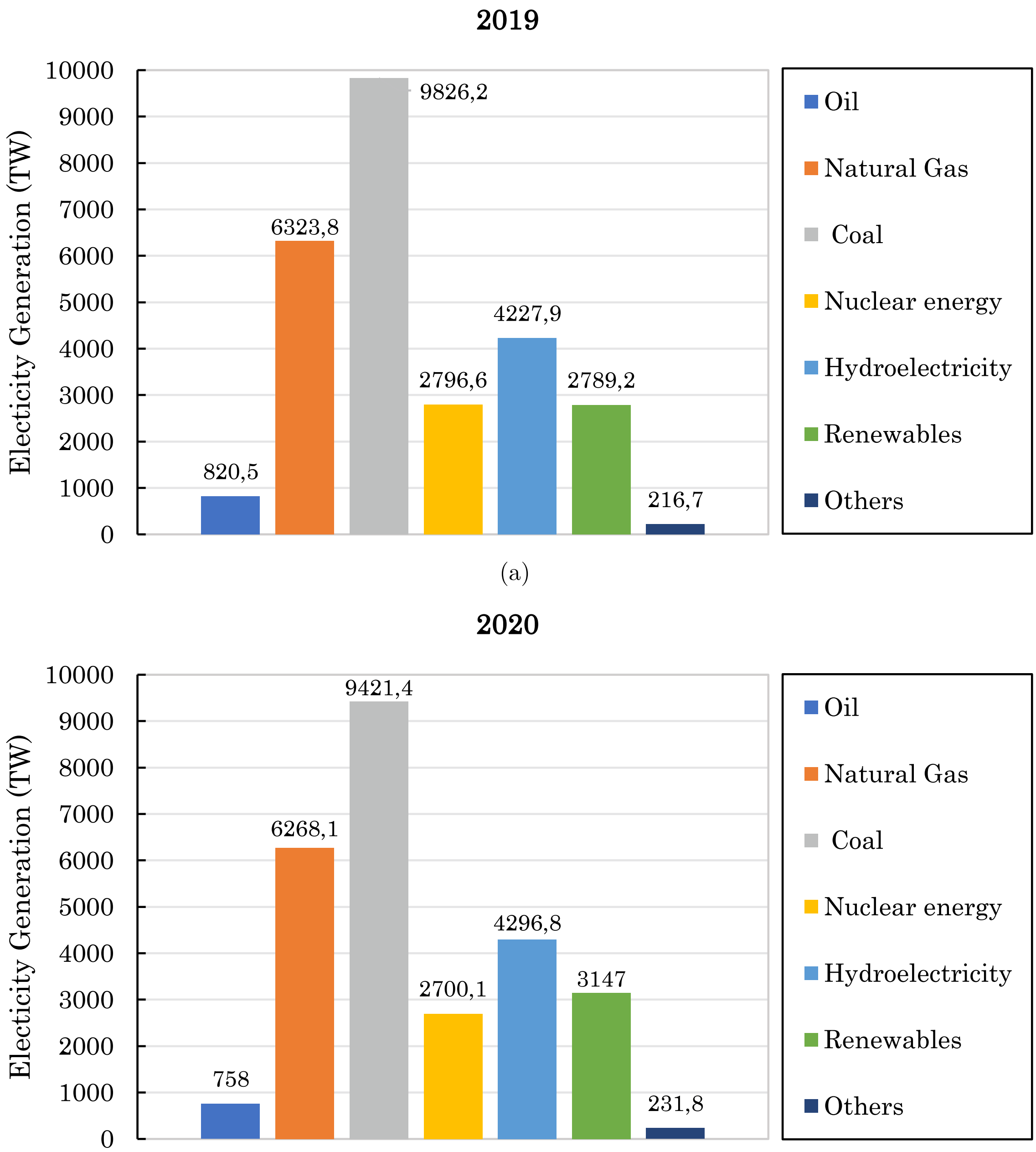

(a)

(b)

Source: Adapted from (BRITISH PETROLEUM, 2021)

of the priority areas targeted by Haitian authorities in their development and economic growth policy. The consumption of wood and its derivatives represents more than 80% of the national energy consumption (approximately 300 thousand tons of wood each year). The wood charcoal industry represents a turnover of more than 80 million US dollars, more than 50,000 jobs and covers 90% of the energy consumed in households for cooking (RINA, 2019). The impact of wood consumption for energy affects human health and is reflected in the growing number of chronic respiratory diseases caused by the burning of fuelwood and coal. Petroleum products represent only 20 to 25% of national energy supply (MTPTC, 2006). The Haitian Republic painfully pays a petroleum bill that represents between 35 and 50 percent of its export earnings (RINA, 2019). However, the quantity of imported petroleum products is considered too low to cover the demands of the Country, Gasoil dominates the list of imported petroleum products, accounting for 42 percent of the total, followed by gasoline (22 percent), kerosene (16 percent), fuel oil (10 percent), and liquefied petroleum gas (LPG) (6 percent) (RINA, 2019). The transport sector alone absorbs 62 percent of total imports. Since 1996, Haiti has imported only unleaded gasoline, minimizing the pollution risks associated with this sector. Haiti's energy landscape is characterized by: an estimated population of 11 million, 50.5% of whom live in rural areas located away from the national electricity grid controlled by EDH (FAYE, 2012). Electricity coverage in the country is about 38% (72% in urban areas and 15% in rural areas) (HAITILIBRE, 2018). High investment costs and some of the highest electricity costs in the Latin America and Caribbean region (US$ 0.30/kWh for residential customers) explain the low electrification rate. About 85% of Haiti's electricity is generated by burning imported fossil fuels (BELT; KASHI; ALLIEN, 2017). The current installed capacity of the Port-au-Prince grid is 250 megawatts (MW), where EDH owns the 54 MW Peligre hydroelectric power (recently renovated with funding from IDB, OFID, and KFW) and the Carrefour I, II, and III diesel plants (total 67.8 MW) (RINA, 2019).

Figure 1.7 – Electricity Generation by Department in Haiti in 2019.

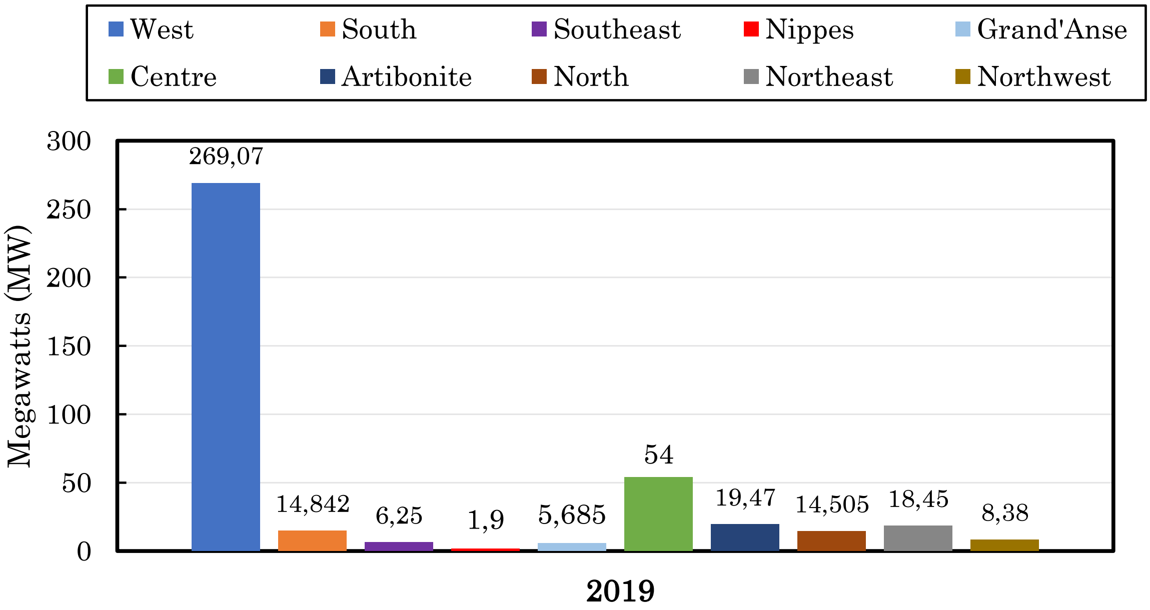

Source: Author

Haitian energy system has a total installed generation of 413.282' MW and is subdivided into 4 major electricity grids (Metropolitan Zone, the Far North, the Far South, Artibonite, and the Center-West) spread across the 10 departments of the country.Figure

1.7 shows electricity production in 2019 by department, and the areas served by the different networks throughout the country are shown in Table 1.1. EDH has approximately 1,700 km of transmission and distribution lines around the country. Haiti has abundant solar and wind energy resources. Decentralized renewable energy can be an important tool for increasing electricity coverage in off-grid communities and for generating electricity at a lower cost than that generated by fossil fuels. Recognizing the market opportunity presented by lower costs of PV systems, several private companies have started to develop innovative technological solutions to deliver electricity to off-grid communities. Various models have been promoted, such as Re-Volt (a pioneering start-up offering off-grid services), pay-per-use solar energy services (with more than 5,000 products sold in La Gonâve, one of the most isolated and poorest communities in Haiti), the Electric Cooperative of Côteaux District (a hybrid system (solar and diesel) supplying more than 1,600 households), EarthSpark (a hybrid generation mini-grid with a backup diesel-powered generator offering prepaid service), Sigora (a pay-per-use technology system through interconnected mini-grids designed for rapid deployment), and NRECA, a 10 MW thermal power plant located in Caracol Industrial Park (NorthEast department) implemented through cooperative agreements

1.3 RENEWABLE ENERGIES

Energy remains a key factor in socio-economic development of a society. It is becoming more and more problematic with the growth of oil prices and global energy demand in one hand (AYADI; COLAK; BULBUL, 2020) and the negative environmental effects induced by the use of fossil fuels which are considered as the main sources of energy in the other hand (BOURAIOU et al., 2015; DABOU et al., 2016). Therefore, many countries have made efforts to solve this problem. They have considered an appropriate and effective solution, which is based on renewable energy sources (AYADI; COLAK; BULBUL, 2020). Indeed, renewable energy considered as the main energy source for future electricity generation (NAVEEN R.AND P. P. REVANKAR, 2020) is defined as clean energy and it is derived from natural sources or from regularly renewing processes (OJO; AWOGBEMI; OJO, 2020). According to data published by the International Renewable Energy Agency (INTERNATIONAL RENEWABLE ENERGY AGENCY, 2021), the world added more than 260 GW of renewable energy capacity in 2020, representing a growth rate of 10.3% over 2019. As a result, global renewable energy capacity additions in 2020 surpassed previous records despite the economic downturn resulting from the Covid-19 pandemic. IRENA 2021's annual renewable capacity statistics shows that renewables' proportion of all new generation capacity increased significantly for the second consecutive year. Over 80% of all new electric capacity added last year was renewable, where solar

Table 1.1 – Distribution grid of 10 departments in Haiti.

Region	Grid Operators	Supply Area
WEST	EDH	Old Delmas, New delmas, Canapé Vert
		Toussaint Brave,Carrefour-Feuilles,Martissant
		Rivière-Froide,Croix des Missions,Croix des Bouquets
		Varreux,Tabarre
FAR NORTH	EDH of NORTH	Limbé, Port-Margot, Acul-du-Nord, Plaine du Nord
	EDH of NORTH	Quartier-Morin, Milot, Grande Rivière du Nord
	EDH of NORTH	Dondon, Cap-Haitien
	EDH of Fort-Liberté	Ouanaminthe, Malfeti, Ferrier, Fort-Liberté
	PPSELD NRECA	Terrier-rouge, Trou-du-Nord, Limonade
	PPSELD NRECA	Saint Suzanne, Caracol
	EDH of Port-de-Paix	Port-de-Paix, La Pointe des Palmistes
	SIGORA	Môle-Saint-Nicolas, Bombardopolis
FAR SOUTH	EDH of South	Les Cayes, Cavaillon, Saint-Louis-du-Sud
	EDH of South	Camp-Perrin, Maniche, Torbeck, Chantal
	EDH of South	RSt-Jean-du-Sud, Port-Salut, Arniquet
	CEAC Project	Roche-à-Bateau, Coteaux, Port-à-Piment
	EDH of Petit-Goâve	Petit-Goâve, Grand-Goâve, Miragoâne
	EDH of Petit-Goâve	Paillant, Petite-Rivière de Nippes
	EDH of Grand ’Anse	Jérémie
CENTRE	EDH (PELIGRE)	Thomonde, Hinche, Thomassique, Maissade
		Cerca-Carvajal, Pignon, La Victoire, Ranquitte
		Saint-Raphaël, Saint-Michel de l’Attalaye
		Boucan-Carré, Lascahobas, Belladère
		Marmelade, Mirebalais, Saut d’Eau, La Chapelle
ARTIBONITE	EDH	Gros-Morne, Ennery, Gonaïves, L’Estère
		Dessalines, Grande-Saline, Liancourt
		Petite-Rivière de l’Artibonite, Verrettes
		Desdunes, Saint-Marc, Montrouis

and wind accounted for 91% of new renewable energy (INTERNATIONAL RENEWABLE ENERGY AGENCY, 2021). By the end of 2020, Global renewable energy capacity totaled 2799 GW, with hydropower still accounting for the largest share (1211 GW), although solar and wind are catching up quickly (714 GW and 733 GW, respectively). Indeed, the two renewable energy sources dominated capacity expansion in 2020 with 127 GW and 111 GW of new solar and wind installations respectively. Installed solar capacity has now reached approximately the same level as wind capacity due largely to expansion in Asia (78 GW) in 2020 with significant capacity growth in China (49 GW) and Vietnam (11 GW). Japan also added more than 5 GW, India and the Korea Republic increased their solar capacity by more than 4 GW. The United States added 15 GW and Brazil added 3.3

GW of additional capacity in 2020. Figure 1.8 shows Global renewable energy capacity from 2011 to 2020 and renewable energy capacity additions by technology from 2019 to 2020.

Figure 1.8 – Global Renewable Energy Capacity; (a) From 2011 to 2020 (b) By sources added between 2019 and 2020

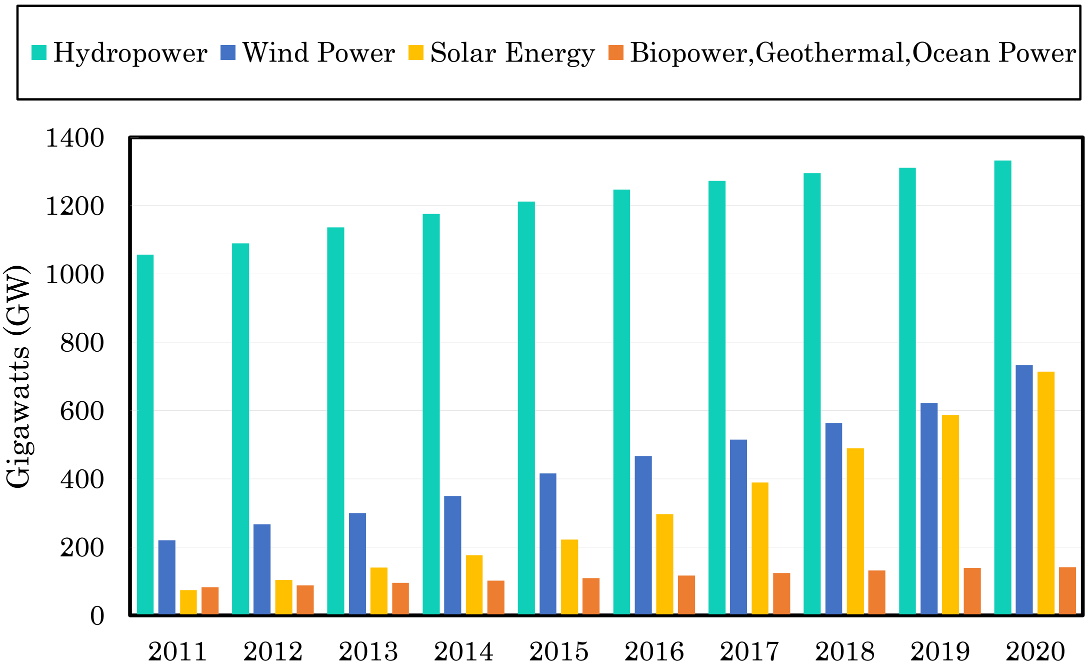

(a)

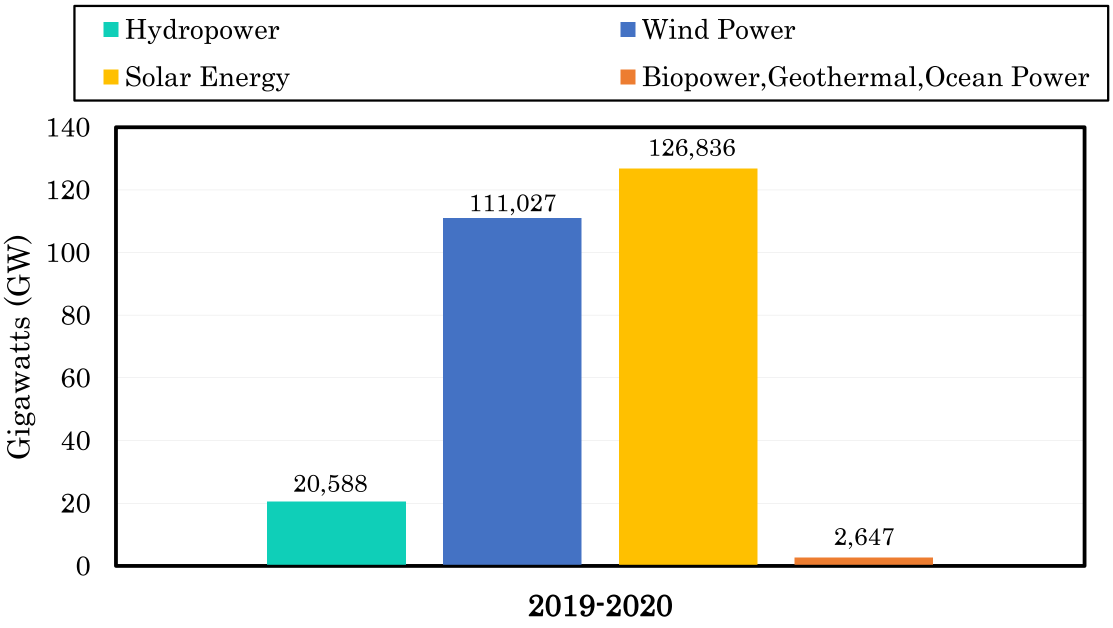

(b)

Source: Adapted from (INTERNATIONAL RENEWABLE ENERGY AGENCY, 2021)

The growing share of renewables is driven by the downgrading of fossil fuel power generation in Europe, North America, and for the first time in Eurasia (Armenia, Azerbaijan, Georgia, Russian Federation, and Turkey). Total fossil fuels additions have indeed dropped to 60 GW in 2020 from 64 GW in 2019 (INTERNATIONAL RENEWABLE ENERGY AGENCY, 2021), highlighting a continuous declining trend in fossil fuels expansion. According to Figure 1.8, solar photovoltaic power grew by 21.6% from 2019 to 2020, Windpower with a growth rate of 17.84%, followed by Biopower,Geothermal,Ocean Power and Hydropower with respective rates of 1.9% and 1.57%.

1.3.1 Solar Photovoltaic Energy

Photovoltaic energy has become one of the most competitive sources of renewable energy generation in the world. It is therefore set to play a major role in the low-carbon transition. The expected development could lead to the installation of 1.4 million modules worldwide every day. Although this development will require a large variety of mineral raw materials, economic, environmental and social risks associated with the deployment of PV modules are limited. Given the significant share of silver, silicon metal and tellurium consumption by PV, the deployment of PV will have a significant impact on the demand for these metals. The extent of this demand will depend on the PV technologies used and their evolution (evolution of energy yield per unit area, evolution of the material content of equipment, development or not of high value-added recycling,...). Since 2011, the global PV market has been growing at an accelerated pace, from 73.745 GWp of annual installed capacity in 2011 to approximately 713.97 GWp in 2020, which is about 10 times more. Initially located in Europe, photovoltaic capacity installed worldwide has expanded to the United States, Japan and China, and more recently to India. This exponential growth in installed capacity has not led to a substantial increase in the share of photovoltaics in global electricity production, which was 3% in 2020. Thus, electricity generation is still largely based on fossil fuels. Since the 2010s, PV systems have seen a drastic reduction in price, regardless of the PV technology involved. This price reduction concerns all components of the PV system. It has been particularly marked for crystalline modules, whose prices have been almost divided by 10 between 2009 and 2019 (from 2.15 dollars/Wp to 0.22 dollars/Wp) (UNITED NATIONS ENVIRONMENT PROGRAMME, 2020). This development is due to multiple factors:

a) Shifts in scale of component production (the PV industry has become a mass industry).

b) Production overcapacity.

c) A massive transfer of a large part of the upstream and intermediate value chain to low-cost countries, particularly China, accompanied by very significant subsidies.

d) Improvements in the efficiency of production processes: increasing the size of ingots, development of cutting methods to reduce material losses (diamond wire cutting).

1.3.2 Solar Energy Technologies

There are three primary technologies for harnessing solar energy: Photovoltaic (PV) systems, which convert sunlight directly into electricity; Concentrating Solar Power (CSP), which uses the sun's heat (thermal energy) to drive utility-scale electric turbines; and Solar Heating and Cooling (SHC) systems, which collect thermal energy to provide hot water and heating or air conditioning.

1.3.2.1 Solar Heating and Cooling (SHC)

Solar heating and cooling (SHC) technologies collect thermal energy from the sun and use that heat to provide hot water, heating, cooling and pool heating for residential, commercial and industrial applications. These technologies replace the need to use electricity or natural gas. In 2011, worldwide, approximately 750 solar cooling systems were installed, including small capacity (<20kW) installations (DANIEL; ULI, 2012).

Many regions of the world have sufficient solar resource to run solar heating and cooling technologies; even in the cloudiest regions, the resource can be adequate for some solar thermal technologies. The technical potential of solar energy for heating and cooling systems is therefore vast. In this case, the best resource areas are those with limited cloud cover, such as in deserts and subtropical regions. The deployment of this technical potential is mainly limited by the availability of land and/or roofs and by the proximity of heating and cooling demand, based on rather restrictive assumptions about roof availability, the technical potential for solar water heating has been estimated at 3,415 TWh/yr (or 123 EJ/yr) in the long term (INTERNATIONAL ENERGY AGENCY, 2012). Only one study is known to have estimated the technical potential of solar water heating based on available roof area for photovoltaic applications and irradiance by region (HOOGWIJK; GRAUS, 2008).

1.3.2.2 Concentrating Solar Power (CSP)

Concentrating solar power (CSP) plants use mirrors to concentrate the sun's energy to drive turbines or traditional steam engines to generate electricity (Ershun Du et al., 2018). The thermal energy concentrated in a CSP plant can be stored and used to generate electricity when needed, day or night. In 2020, approximately 6,5 Gigawatts (GW) of

CSP plants are installed in the world (INTERNATIONAL RENEWABLE ENERGY AGENCY, 2021).Concentrated Solar Power could meet up to 6% of the world's electricity demand by 2030 and 12% by 2050, as predicted by the European Solar Thermal Power Association (European Solar Thermal Electricity Association, 2016). Figure 1.10 shows the installed capacity of concentrated solar power between 2011 and 2020. Concentrating solar technologies concentrate sunlight from a large area opening to a small area using lenses or mirrors as shown in Figure 1.9. When the concentrated light is converted into heat, very high temperatures can be produced. The higher the concentration ratio, the higher the maximum temperature.

Figure 1.9 – The 110-megawatt Crescent Dunes Solar Energy Facility in Nevada is the first utility-scale concentrating solar plant that can provide electricity whenever it's needed most, even after dark. Credit: SolarReserve

Source: SolarReserve

The solar energy used by high-concentration solar technologies is measured as direct normal irradiance (DNI), which is the energy received directly from the sun on a surface tracked perpendicular to the sun's rays (INTERNATIONAL ENERGY AGENCY, 2010). Concentrating solar technologies require clear skies and sufficient DNI to achieve high performance levels. This requirement limits the favorable areas for its deployment.

Figure 1.10 – Installed capacity of Concentrated Solar Power between 2011 and 2020.

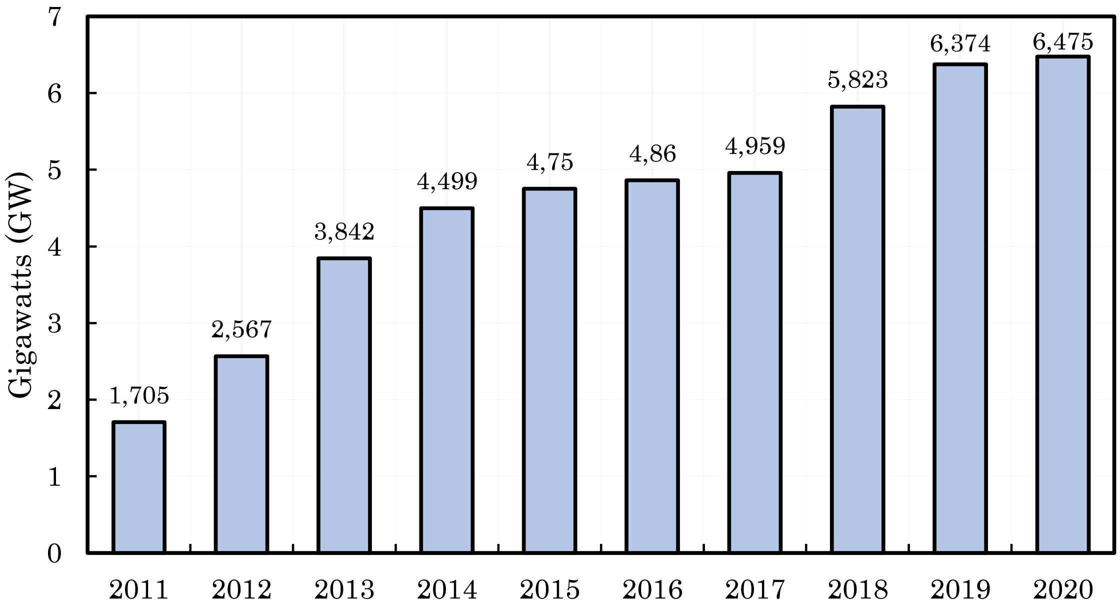

Source: Adapted from (INTERNATIONAL RENEWABLE ENERGY AGENCY, 2021)

1.3.2.3 Solar Photovoltaics

A PV generator is the whole of solar cells, connections, protection parts, supports (GOETZBERGERA; HEBLINGA; SCHOCKB, 2003). A photovoltaic cell is made of a semiconductor doped differently according to the faces: this doping consists in inserting impurities to induce an excess of electrons (material called N-doped as negative) or a deficit of electrons (material called P-doped as positive). The contact of the N-doped region with the P-doped region creates a junction and an electric field. These basic cells are connected to form solar PV modules.

On the other hand, the use of photovoltaic cells allows to transform into electricity the Photons emitted by the sun under photoelectric effect. The maximization of this photoelectric effect is based on the physical properties of semiconductors.

Photovoltaic cells are small (usually a square of about 15 cm on each side) and produce only a small electrical power, 1 to 5 W with a voltage of less than one volt. To produce more power, it is necessary to assemble these cells into modules. A module is generally made up of 60 cells (modules with 72 cells are also used), connected in series and in parallel, for an area of approximately 1.6 m^2.

1.3.2.4 Modeling of Solar Cell

The ideal solar cells behave like a current source connected in parallel with a diode, the output of the current source is directly proportional to the light falling on the cell (photocurrent Iph). During darkness, the solar cell is not an active device; it works as a diode, i.e. a p-n junction. It produces neither a current nor a voltage. This ideal model is completed with resistors to represent the losses and sometimes with additional diodes that takes into account other phenomena (WOLF; RAUSCHENBACH, 1963).

Figure 1.11 – Circuit diagram of Photovoltaic Cell

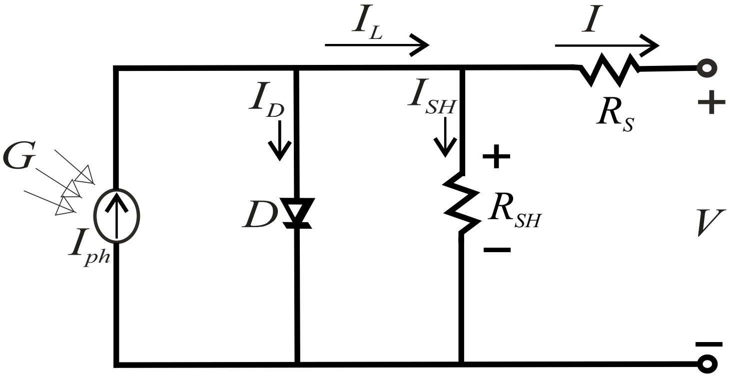

Source: Author

The most popular circuit equivalent to a solar cell/panel is shown in Figure 1.11 consist of;

a) A current source I_{ph}, which suggests the light generated current.

b) A Shunt resistance R_{SH}, in parallel with the diode, this corresponds to the leakage current to the ground and it is commonly neglected.

c) A Series resistance R_S, which gives a more accurate shape between the maximum power point and the open circuit voltage. This represents the internal losses due to the current flow.

In an ideal cell $R_s = R_{SH} = 0$, which is a relatively common assumption (MALEWSKI et al., 2000). The voltage generated at terminals V is the voltage of the PV module, which can be multiplied through series connected PV modules. Moreover, the current outflow from the PV terminals is I. The relationship between V and I can be expressed in equation (1.1).

The I-V behavior of the circuit equivalent model shown in Figure 1.12(a) is defined by equation 1.3 (KENNERUD, 1969).

$$I = I_{ph} - I_0 \left[e^{\left(\frac{V+IR_s}{aV_T}\right)} - 1 \right] - \frac{V + IR_S}{R_{SH}} \tag{1.1}$$

V_T is the thermal voltage of the diode and depends on the charge of the electron q, the Boltzmann constant k, the number of cells in series n and the temperature T.

$$V_T = n\frac{kT}{q} \tag{1.2}$$

Then;

$$I = I_{ph} - I_0\left[e^{\left(\frac{q(V+IR_s)}{akT}\right)} - 1\right] - \frac{V + IR_S}{R_{SH}} \tag{1.3}$$

where;

- I = Output current of the cell
- I_{ph} = Photocurrent delivered by the constant current source
- I_0 = Reverse saturation current corresponding to the diode D
- q = Electronic charge
- a = the ideality factor that takes into account the desviation of the diodes from the Shockley diffusion theory
- k = Boltzmann's constant
- T = Absolute temperature, K
- V = The voltage appearing at the cell terminals
- R_S = Series resistance
- R_{SH} = Shunt resistance.

The photocurrent I_{ph} and the saturation current of the diode I_0 depend on the temperature;

$$I_{ph} = I_{ph}(T_1) + K_0\left(T_2 - T_1\right) \tag{1.4}$$

with;

$$K_0 = \frac{I_{SC}\left(T_2\right) - I_{SC}\left(T_1\right)}{\left(T_2 - T_1\right)} \tag{1.5}$$

Then, the saturation current of the diode in terms of the given reference temperature is expressed by equation 1.6.

$$I_0 = I_0\left(T_1\right) \times \left(\frac{T}{T_1}\right)^{\frac{3}{a}} e^{\frac{qV_q(T_1)}{nk\left(\frac{1}{T}-\frac{1}{T_1}\right)}} \tag{1.6}$$

V_q is the band gap energy of the semiconductor, T is the real temperature and T_1, T_2 are the given reference temperatures. I_{SC} is the short circuit current when $V = 0$, then $I_{SC} = I_{ph}$. V_{OC} is the open circuit voltage, produced when the open circuit condition $I_{SC} = 0$

At the open-circuit point on an experimental $I - V$ curve, $V = V_{OC}$, and $I = 0$. by substituting these equalities in 1.3, the Open Circuit voltage expression can be obtained by this expression;

$$0 = I_{ph} - I_0 \left[e^{\left(\frac{q(V_{OC})}{akT} \right)} - 1 \right] - \frac{V_{OC}}{R_{SH}} \tag{1.7}$$

At the short-circuit point on the $I - V$ curve, $V = 0$ and $I = I_{SC}$. With these substitutions in 1.3, the short circuit current can be expressed by resolving this equation;

$$I_{SC} = I_{ph} - I_0 \left[e^{\left(\frac{q(I_{SC} R_s)}{akT} \right)} - 1 \right] - \frac{I_{SC} R_S}{R_{SH}} \tag{1.8}$$

Expression for the photocurrent I_{ph} and the Diode saturation current I_0 can be simplified by these equations below (CUBAS; PINDADO; VICTORIA, 2014).

$$I_{ph} = \frac{R_{SH} + R_S}{R_{SH}} I_{SC} \tag{1.9}$$

$$I_0 = \frac{(R_{SH} + R_S)\, I_{SC} - V_{OC}}{R_{SH} e^{\frac{qV_{OC}}{ankT}}} \tag{1.10}$$

Figure 1.12 shows the Current-Voltage and Power-Voltage curves(I-V curve and P-V curve) of the Soltech STH-215-9 photovoltaic module (MATLAB, Simulink) at a constant temperature of 25 °C.

.

1.3.3 Static PV Arrays

The size of a PV array can consist of a single PV module or panel connected together in a rooftop urban environment, or may consist of many hundreds of PV panels interconnected together in a field to provide power to an entire city or neighborhood. The flexibility of the modular photovoltaic array (PV system) allows designers to create solar energy systems capable to meet a wide variety of electrical needs, regardless of their size. To limit the effects of mismatch and shading, the PV array wiring scheme must be considered to identify an architecture with sufficient redundancy. Various possible PV array interconnection schemes were reported in (WANG; HSU, 2011). A simple S array can achieve high output voltage for low output current, while a P array can deliver the highest output current, but at a low output voltage. The S and P network are wired most simply. The SP array can provide both high voltage and high current, but has also a

Figure 1.12 – (a) I-V curve and (b) P-V curve at a fixed temperature of 25 °C and different levels of insolation from 0.2 to 1 kW/m^2

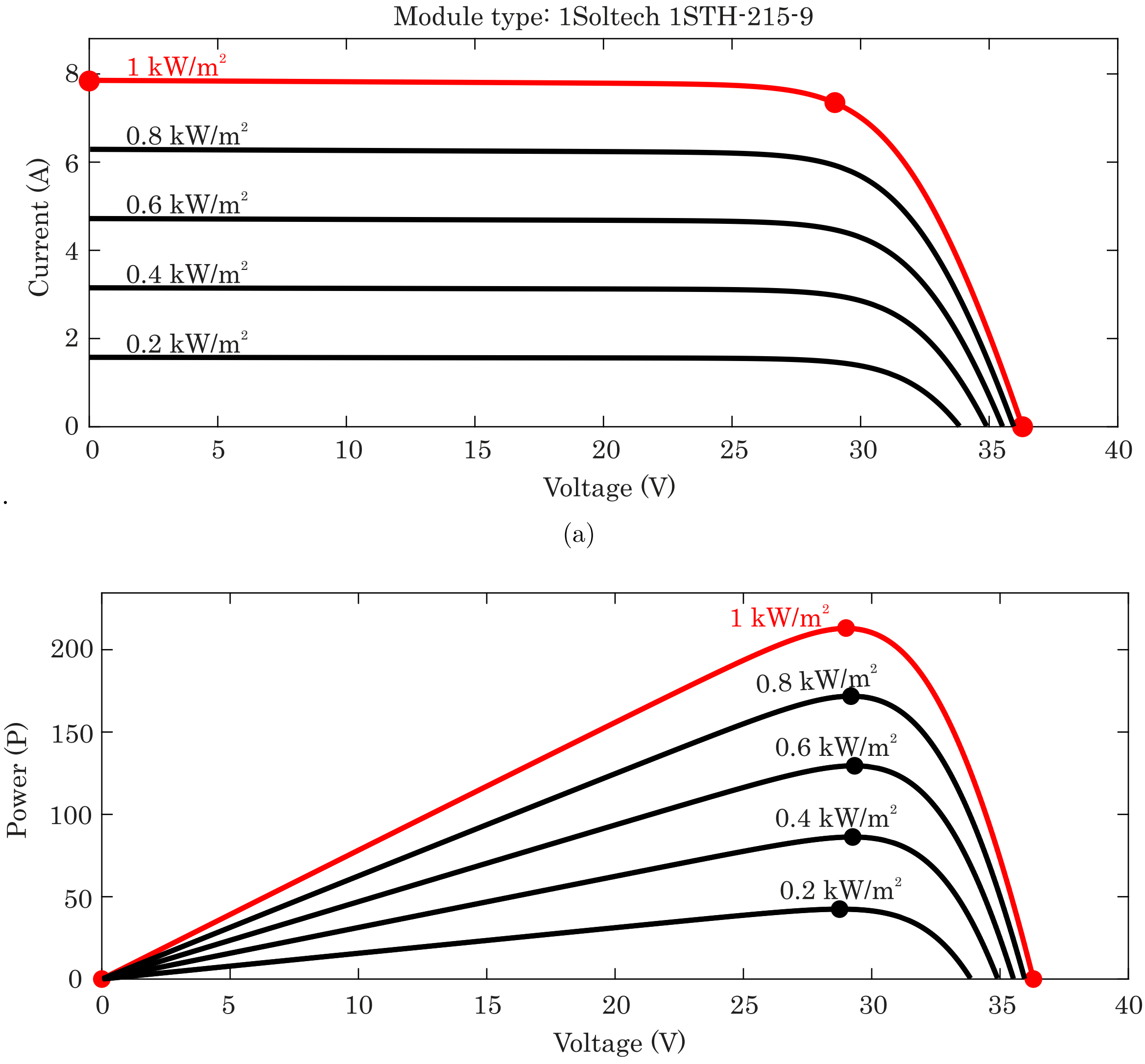

(a)

(b)

Source: Author

simple wiring. SPS array is formed by connecting in series multiple short SP sub-arrays (ABRAMOVITZ; SHMILOVITZ, 2021). Figure 1.13 presents four common configurations of PV Array.

1.3.4 Architecture Grid-Connected Photovoltaic Systems

PV energy is used in two application areas: off-grid PV and grid-connected PV. The implementation of the conversion schemes and the function of these two applications are very different. In the following, the topologies of grid-connected PV arrays and their

Figure 1.13 – Standard PV array configurations:(a) Serial; (b) Parallel; (c) Serial-Parallel; (d) Serial-Parallel-Serial

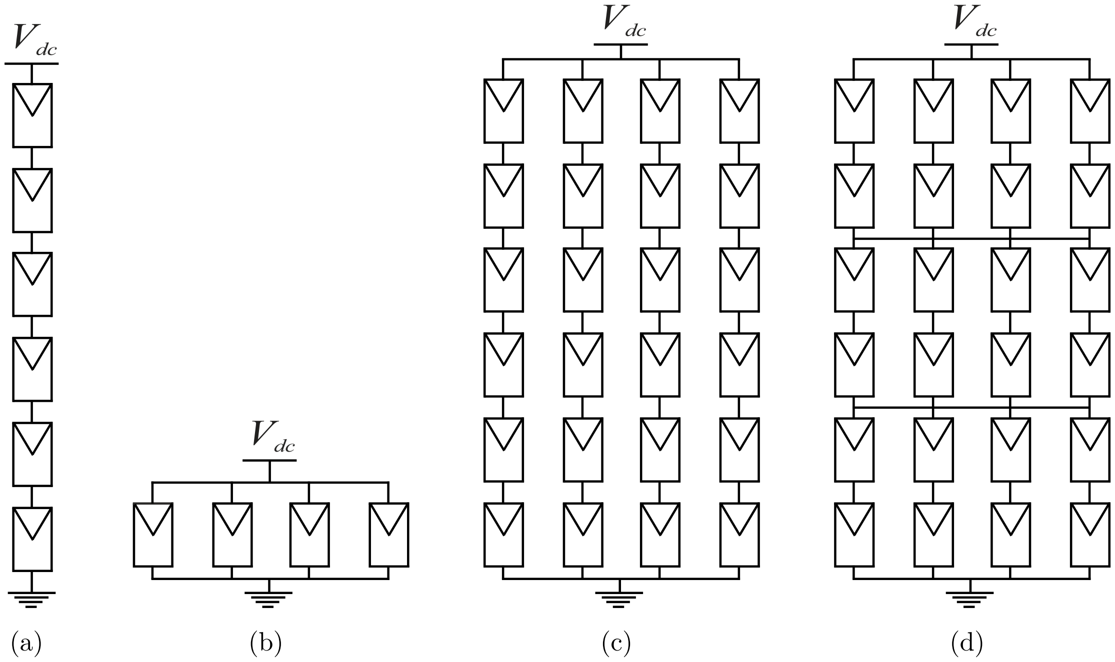

Source: Adapted from (ABRAMOVITZ; SHMILOVITZ, 2021)

function will be presented. Having as final goal the production of energy, a photovoltaic installation requires the implementation of a conversion chain from sunlight energy to electrical energy based on photovoltaic effect. Whatever its architecture, this conversion chain can be divided into several sub-systems according to their functionality. The electronic inverter is a very important part of any solar power system. It works as an intermediary between the solar energy and the grid. It provides a maximum power point tracking (MPPT) function to maximize the input energy. It converts the DC voltage obtained from the PV array into AC current and injects it into the grid according to power quality standards, raising the power factor and minimizing harmonic distortion.

Many approaches for grid-connected photovoltaic systems have been proposed and thus commercially implemented in the last decades, such as centralized, string, multi-string, module-integrated converters (MICs), etc. As a result, High Step-Up and High efficiency DC-DC converters have been defined as the technology to combine photovoltaic systems with the grid (KJAER; PEDERSEN; BLAABJERG, 2005). The following section focuses on a broad overview of these different topologies.

1.3.4.1 Centralized inverter

The centralized inverter, as shown in Figure 1.14, is the oldest and most classical topology for PV applications, consisting of a single inverter interfacing the grid and the PV array, the PV modules are divided into several strings connected in parallel, each string generating a sufficiently high voltage, thus eliminating any additional voltage rise. The advantage of the central inverter topology is its simplicity of implementation: only one inverter connected to the PV array is required. In addition, the central inverter requires a low investment cost while allowing for simple maintenance.

Figure 1.14 – Centralized inverter configuration

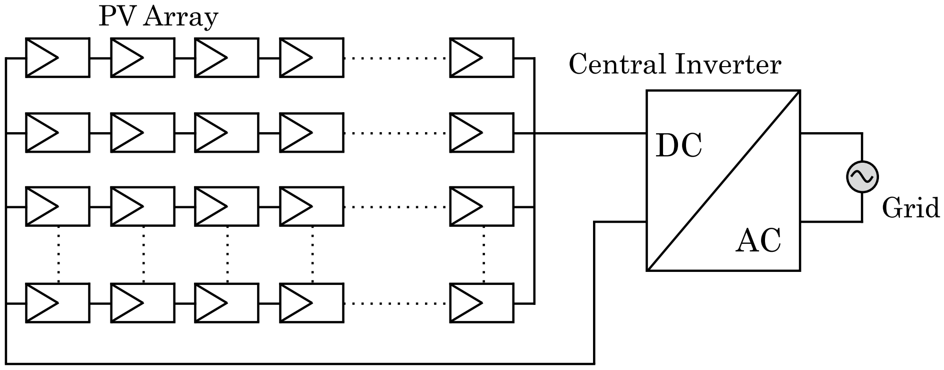

Source: Author

The simplicity of the installation also allows for a higher efficiency of the voltage conversion. Indeed, the series connection of several modules allows to obtain a low transformation ratio, which increases the efficiency of the inverter. This configuration is generally used for high power installations (20-400 kW) in which anti-reverse current protections are implemented per string. Although this topology is robust, very efficient and cheap, the main drawbacks of centralized inverters are the following (S. Bacha and D. Chatroux, 2006)

- Electrical losses and risks in DC cabling, the required DC cabling increases the cost and additional protection considerations.
- No continuous service in case of inverter failure.
- A panel exposed to partial shade can therefore significantly decrease the total production.
- No scalability.

Despite all these shortcomings in this architecture, the centralized inverter is widely used in high power ground mounted PV plants.

1.3.4.2 String inverter

As an improved version of the centralized inverter, the string inverter as shown in Figure 1.15 is one of the most widely used topologies today. This topology consists of implementing an inverter at the end of each string of PV modules to reach several hundred volts and several kilowatts of power (KJAER; PEDERSEN; BLAABJERG, 2005). The inverters are then connected in parallel to the electrical grid, which requires coordination between the inverters to avoid islanding and power swapping between the inverters. The string inverter topology allows to improve the control of available power per string through the MPPT of each inverter. In addition, continuous operation is improved because the failure of an inverter will not shut down the entire installation.

Figure 1.15 – String inverter configuration

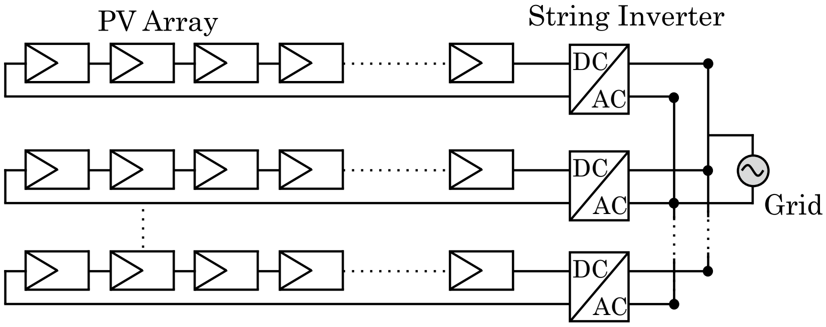

Source: Author

1.3.4.3 Multi-String inverter

The use of multiple conversion stages can improve the conversion efficiency and reliability of the system, according to (KJAER; PEDERSEN; BLAABJERG, 2005), by dissociating the functionality of the inverter. Multi-string inverter approach as shown in Figure 1.16 realizes the idea of an active SP grid. Low power DC/DC converters are stacked on a single string to maintain MPPT at the string level, multiple strings are connected in parallel to a DC bus through their individual DC/DC converters for higher output power. The DC bus then supplies power to the grid through a DC/AC converter. MPPT is done for each string, which limits the influence of the modules on each other (INTERNATIONAL ENERGY AGENCY - PHOTOVOLTAIC POWER SYSTEMS PROGRAMME, 2001). The assembly remains scalable, but continuous operation is not guaranteed in case of inverter failure. Compared to the "string" inverter, costs are likely to be reduced because each string inverter does not need to integrate voltage and grid current measurement and monitoring functionalities (MEINHARDT; CRAMER, 2000).

Figure 1.16 – Multi-String inverter configuration

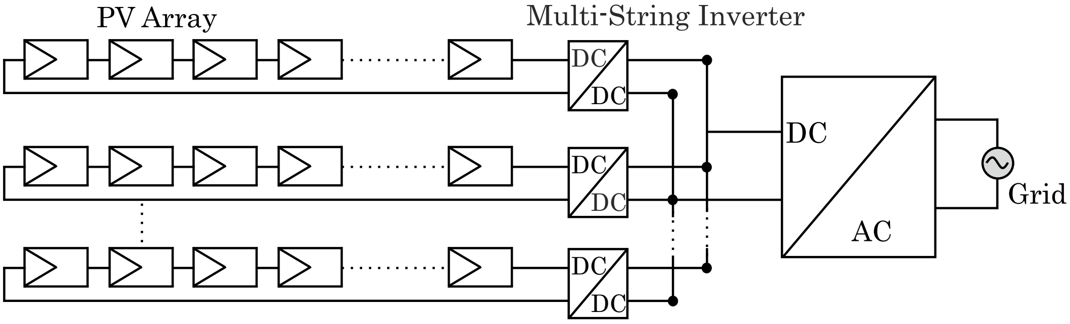

Source: Author

1.3.4.4 Micro-inverter

The AC module, also known as a module integrated converter (MIC) or simply a microinverter presented in Figure 1.17, is a dedicated low-power inverter designed to interface a single PV module directly to the grid (MYRZIK; CALAIS, 2003). This new technology has grown rapidly in recent years for several reasons; single MPPT for each PV panel eliminated the mismatch between different panels, so that the maximum power output was tapped even if some panels are partially shaded, parallel connection of these AC modules to the grid enabled a "plug in and play" device by reducing the installation costs (WALKER; PIERCE, 2006; LISERRE; TEODORESCU; BLAABJERG, 2004), it eliminates the need for bulky and expensive low frequency power transformers, it offers a very compact design in which the inverter can be attached to the back of the PV array (VLATKOVIC, 2004). This enhances energy harvesting and system efficiency, flexibility and scalability, and eliminates losses due to mismatch between PV modules.

Figure 1.17 – Microinverter configuration

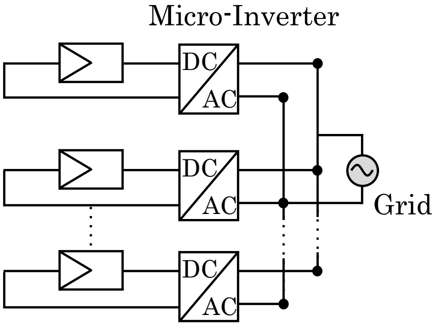

Source: Author

The main drawbacks of MIC are its higher cost per watt due to the voltage step-up requirements, which requires additional power processing and dedicated control, and its limited reliability issue mainly due to the limited lifetime of dc-ac decoupling electrolytic capacitors when exposed to the harsh field conditions of PV installations. Recent developments show promising solutions to the above problems and at the cost of increased hardware complexity (YOGESH; THORAT, 2013).

1.3.5 Review of Micro-inverter Topologies

The basic functions performed by a grid-connected microinverter consist of extracting the maximum power (MPPT), DC current from the panel, boosting the voltage to the grid voltage, and injecting sinusoidal current into the grid. Various microinverter topologies are illustrated in Figure 1.18. One of the common classifications is based on the number of stages of power processing. The conversion from DC to AC inside the PV module can be done in a single stage or in double stages. The block diagram of single and double-stage inverter topologies is shown in Figure 1.19 The following section discusses the characteristics of various existing topologies commonly used for microinverters.

Figure 1.18 – Microinverter topologies classification

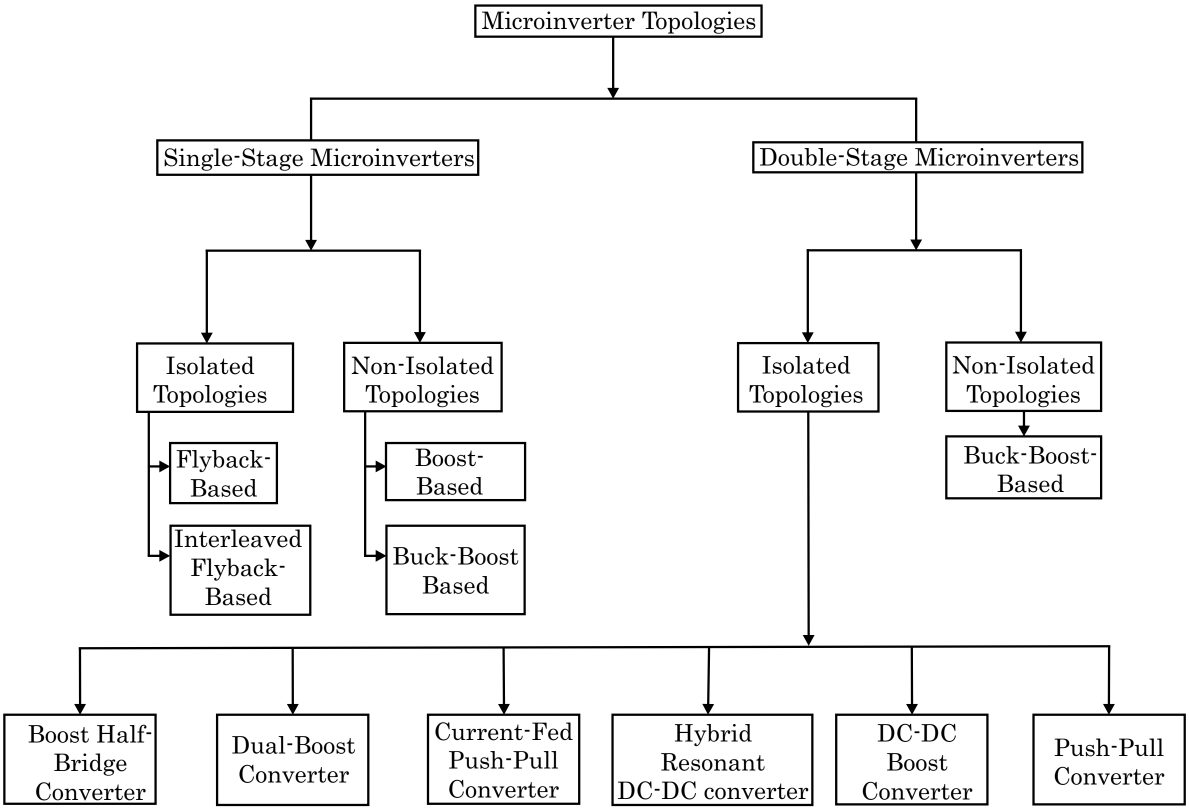

Source: Adapted from (ALLUHAYBI; BATARSEH; HU, 2020)

1.3.5.1 Single-Stage Microinverter

In a single-stage microinverter, the whole process is performed by a single DC-AC inverter. Therefore, the power conversion is achieved in a single stage. Single-stage microinverters can be classified into non-isolated single-stage topologies and isolated single-stage topologies. Compared to multi-stage inverters, the size of the inverter can be reduced due to the lower number of electronic components. A microinverter with a specific inverter for voltage amplification and an inverter for sinusoidal grid current generation increases the number of components and its overall size. With the recent trend of miniaturization, single-stage microinverters have become a topic of attention (CHEN; SMEDLEY, 2004; JAIN; AGARWAL, 2007). Since single-stage inverters do not have the ability to reduce the capacitor size at the DC link, power decoupling must be provided either by a large electrolytic capacitor at the input terminals or by using auxiliary circuits (SHINJO; WADA; SHIMIZU, 2007). The flyback inverter is one of the most common topologies for photovoltaic modules because it provides a simple circuit configuration to achieve direct conversion from DC power to AC power. The flyback topology has proven to be a reliable and cost-effective topology with a reduced number of semiconductor switches (KASA; LIDA; CHEN, 2005). Another important feature of the flyback topology is the providing of isolation through the use of a high frequency transformer. These advantages of a flyback inverter make it a viable solution for single-stage microinverters, In addition, the flyback inverter can operate in Continuous Conduction Mode (CCM) or Discontinuous Conduction Mode (DCM) to extract power. However, the CCM operation is not a feasible solution because the inverter tends to act as a voltage source independent of the load due to incomplete discharge of the magnetizing inductor of the transformer (JAIN; AGARWAL, 2007) and also the difficulties met to control the output current. Therefore, DCM has been a more attractive solution in the past for flyback inverters, even though the voltage and current constraints are higher on Turn-ON switching. Conventional flyback inverter is analyzed In (SHIMIZU; WADA; NAKAMURA, 2006).

1.3.5.2 Double-Stage Microinverter

In double-stage Microinverter topologies, tasks performed by the grid-connected system are divided into two stages. The extraction of the maximum power from the PV panel and the amplification of the voltage are usually carried out by a DC-DC converter in the first stage. The second stage is an inverter, which injects a high-quality current to the grid. The output of the first stage converter can be either a pure DC voltage or a rectified AC current. In the case of a pure DC output voltage, the DC-DC converter only needs to handle the rated power and the second stage inverter controls the grid current by means of pulse width modulation(PWM). The double-stage topology includes a boost DC-DC converter section that supplies the required voltage step-up at the DC link. Increasing the voltage at the DC link reduces the capacitance value at the link. Lower capacitance eliminates the need for electrolytic capacitors, which increases the life of the microinverter. A double-stage microinverter with a simple power stage and control scheme has been proposed in (MARTINS; DEMONTI, 2003). The topology consists of a DC-DC flyback converter as the first stage for voltage amplification and galvanic isolation. The second stage consists of a full bridge inverter which realizes the AC injection to the grid. Although it provided robust operation, it generates high switching losses because all power MOSFETs are hard switched in this topology.

Figure 1.19 – Types of Inverter based on processing stages:(a) Single-Stage Microinverter (b) Double-Stage Microinverter

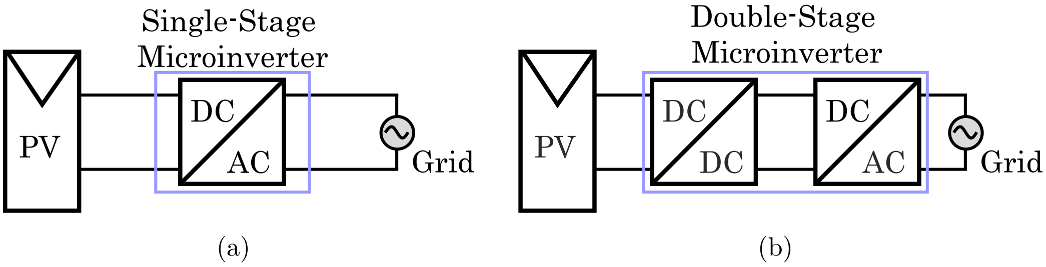

Source: Adapted from (ABRAMOVITZ; SHMILOVITZ, 2021)

1.4 HIGH STEP-UP DC-DC CONVERTER

With the depletion of fossil fuels, the constant increase in the price of oil and the considerable decrease in the price of photovoltaic panels, generation of electricity with renewable energies, in particular photovoltaic energy, becomes an essential feature in the world. However, photovoltaic modules deliver low output voltages, ranging from 12 to 70 V DC. To adjust it to the standards of the electrical grid, this voltage should be stepped up to the DC bus voltage of the system, around 200 VDC or 400 VDC depending on the requirements of the grid as shown in Figure 1.20 (TOMASZUK; KRUPA, 2011)). Therefore, high voltage gain and high-efficiency DC/DC converters are the major consideration to overcome this problem.

Step-up dc-dc converters are becoming increasingly important in applications such as low-voltage, low-power systems (distributed photovoltaic generation systems, power conversion systems, fuel cell power conversion systems, etc.) (ANDRADE; SCHUCH; MARTINS, 2017). Step-up DC-DC converters are used to increase the input voltage level to a higher output level. The conventional boost converter is used for step-up applications, it can ideally provide high voltage gain if the duty cycle reaches 1 in theory. However, in practice, the voltage gain of the boost converter is usually limited by the effects of the power switch, rectifier diode, and equivalent series resistance (ESR) of the inductor and capacitor (LIU; AIAND; LI, 2016). When the duty cycle increases, the conduction losses increases, which can cause reverse recovery problems, and the power rating of the power electronic devices automatically increases. But the overall efficiency decreases.

Despite its features such as simplicity of implementation, continuous input current, low number of components, the conventional Boost dc-dc converter has some limitations in high Step Up DC/DC conversion (SAVAKHANDE; BHATTAR; BHATTAR, 2017).

- Voltage stresses on power switches and diodes are equal to the high output voltage.
- The switching losses and reverse recovery losses of the output diode are large due to the hard switching operation and high switching voltage stress.

Due to these disadvantages of the conventional boost converter in voltage boosting applications, many techniques have been proposed to increase the voltage gain of conventional converters. Among these achievements, they can be classified into the followings: boost converter with quadratic circuit, boost converter with coupled inductor, boost converter with coupled inductor and switched capacitor, soft-switching boost DC-DC converter and so on. All these topologies will be presented in detail in the literature review in Chapter 2.

Figure 1.20 – Diagram of of Step Up from low voltage PV panels to the grid.

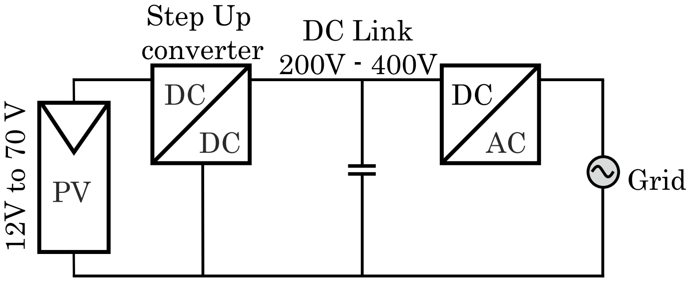

Source: Author

1.5 SOFT-SWITCHING AND HARD-SWITCHING LOSSES

For high voltage gain DC-DC applications, two types of DC-DC converters can be used, which are isolated and non-isolated DC-DC converters. Non-isolated power converters have a single circuit in which current can flow between the input and output, and are frequently used in applications where electrical isolation is not required, due to the fact that they are less bulky and expensive, and more efficient and reliable. Alternatively, isolated converters allow to isolate the input from the output by separating the circuit electrically and physically into two sections preventing DC current flow between the input and the output, usually achieved by using a transformer or a coupled inductor to achieve multiple goals such as voltage level shifting, multiple outputs and galvanic isolation. Isolated power converters achieve high voltage gain by adjusting the turn ratio of the coupled inductor or transformer ((ANSARI; MOGHANI; MOHAMMADI, 2019). However, as the transformation ratio increases, the leakage inductance increases, leading to high switching losses and voltage spikes, degrading the efficiency of this type of converter (HUI; CHENG; PRAKASH, 1997; ANSARI; MOGHANI; MOHAMMADI, 2019).

Power electronic converters are operated with switching devices that turn ON and OFF while converting energy from one form to another. They operate with high switching frequencies to reduce the size of inductors, transformers and capacitors in the converters. However, this high switching frequency operation increases the amount of energy lost due to switching losses and therefore reduces the efficiency of power converters. Switching losses are caused by the overlap of switching voltage and switching current during a switching transition. If, however, the voltage across a switch or the current through it is zero during a switching transition, there is no overlap in switching voltage and current, in other words, there are no switching losses. The techniques that achieve switching losses are called soft-switching techniques and there are two types: zero-voltage switching (ZVS) and zero-current switching (ZCS). For pulse-width modulated (PWM) DC-DC converters, ZVS and ZCS techniques are typically implemented with auxiliary circuits that enable the main power switches to operate with soft switching. While these auxiliary circuits help improve the efficiency of the converters, they increase the cost. So, there is an incentive to try to make these auxiliary circuits as simple and inexpensive as possible, such as the proposed converter in Figure 3.1.

1.5.1 Hard-Switching losses

Power converters generally consist of controlled semiconductor devices such as transistors and diodes, energy storage elements such as inductors and capacitors, and some uncontrolled devices (diodes). Controlled semiconductor devices such as BJTs (bipolar junction transistors), MOSFETs (metal oxide silicon field effect transistors), and IGBTs (insulated gate bipolar transistors) are used as switches in power electronic converters and are designed to work as switches that are either turned ON or turned OFF at a given time. These devices can operate at much higher switching frequencies, mainly to reduce the weight and size of the converters. As a result, switching losses tend to predominate, resulting in higher junction temperatures. The losses can be distributed as shown in Figure

1.21 Semiconductor switches used in power converters are not ideal and are represented as sources of energy losses. Conduction losses and switching losses are the most important losses associated with these switches and will be described in more detail below.

Figure 1.21 – Distributed Semiconductor losses

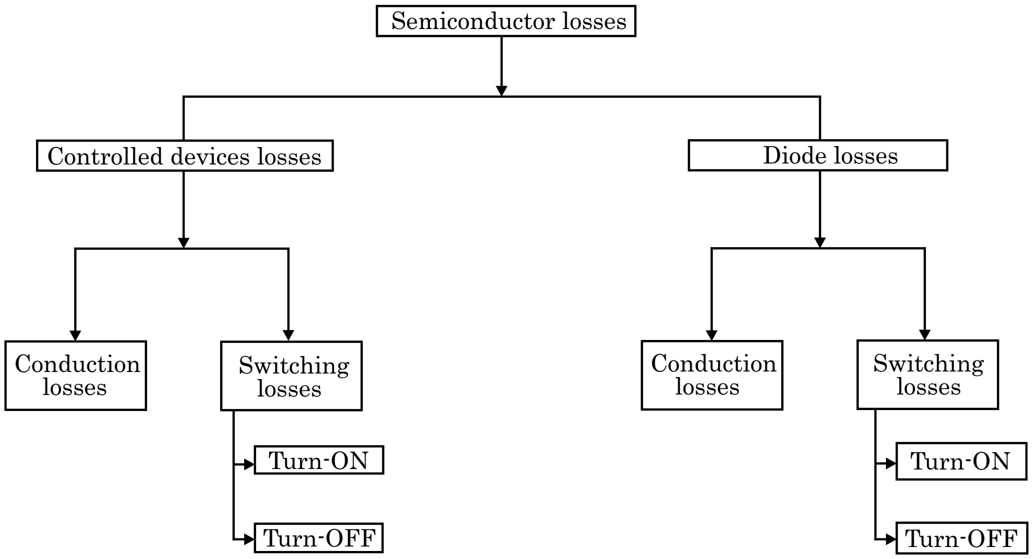

Source: Author

1.5.1.1 Conduction losses

The Conduction losses of power semiconductors are due to its behaving as a resistor when Turned ON, these losses are often calculated by including a voltage representing the voltage drop and a resistance $R_{DS_{ON}}$ representing the current dependence in series with the ideal device the resistance being equal to, the ON state drain to source resistance. The conduction losses of controlled semiconductor devices are related to the amount of current flowing in the device and $V_{CE_{sat}}$, the saturation voltage between collector and emitter.

1.5.1.2 Switching losses

When the transistor is turned ON or OFF, the transition time required to reach the next state is very short, but it is not instantaneous. The time required for a transistor to transition completely from the ON state to the OFF state produces wasted energy, known as switching losses as shown in Figure 1.22. The corresponding power loss during each switching instant is the area of overlap of the switch current and voltage waveforms at the instant the switch is turned ON or OFF. Since average power is defined as energy divided by period, therefore higher switching frequencies result in higher switching losses. Switching losses are responsible for a significant percentage of power converter losses.

1.5.2 Soft-Switching losses

Switching loss and electromagnetic interference (EMI) issues associated with hard-switching converter operation can be reduced by using soft switching. The term "soft switching" in power electronics refers to various techniques in which switching transitions become smoother in order to drive the voltage or current to zero during the switching transition. Electromagnetic interference is reduced by soft switching because switching transitions from ON to OFF and vice versa are gradual instead of abrupt. Switching losses are reduced because the power dissipated in a switch during a switching transition is proportional to the voltage overlap across the switch and the current flowing through it. Soft switching forces either the voltage or the current to be zero during the time of the transition; therefore, there is no overlap between voltage and current and (ideally) no switching loss. There are two types of soft switching: zero voltage switching (ZVS) and zero current switching (ZCS). Although there are many ZVS and ZCS techniques, there are general principles associated with each type which will be discussed more in the Literature review in Chapter 3. Figure 1.22 shows typical current and voltage waveforms of a soft switched device and its operating locus.

1.6 GOALS OF THE DISSERTATION

1.6.1 Main Goal

The main goal of this work is to propose, analyze, design and implement a Single Switch High Step-Up Soft-Switching Boost Converter using Coupled Inductor with the use of a Two-components Resonant Cell to achieve Zero Voltage Switching (ZVS) and Zero Current Switching (ZCS).

Figure 1.22 – Semiconductor devices; (a) Hard Switching losses; (b) Soft-Switching losses

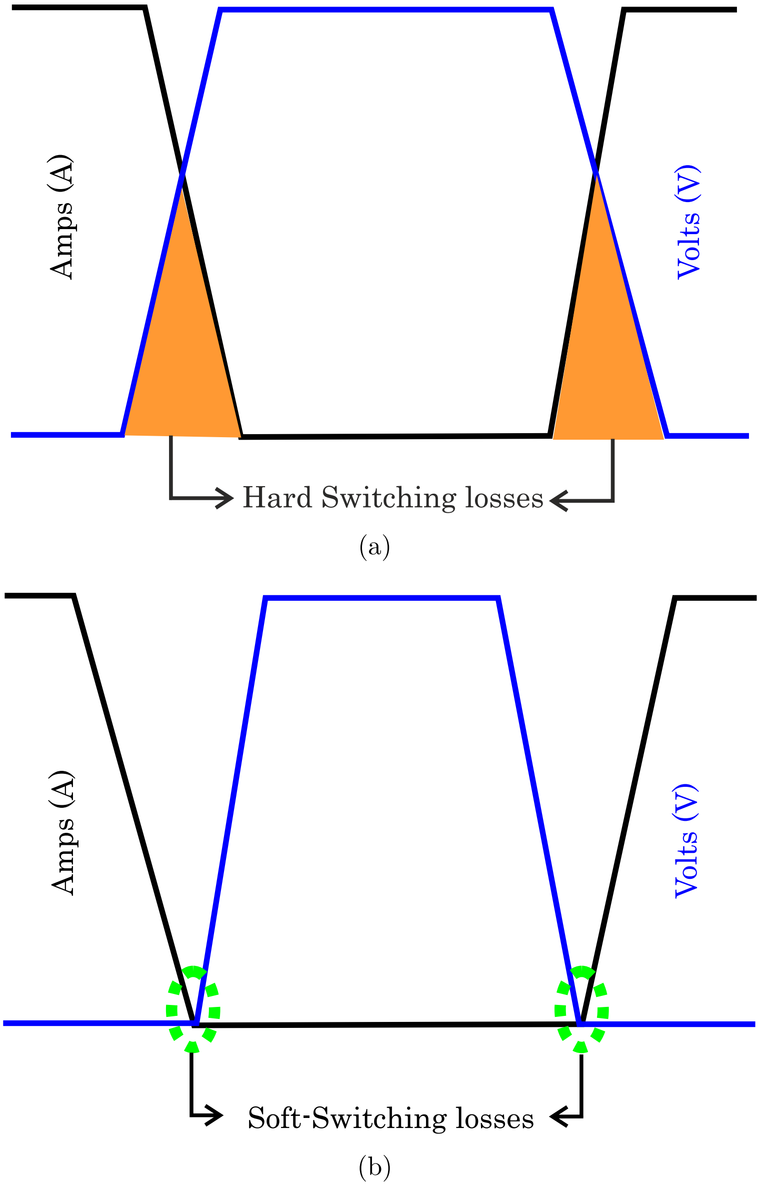

(a)

(b)

Source: Author

1.6.2 Specific Goals

To achieve the main objective of this work, some specific objectives must be defined, such as;

- Conduct a literature review about the main topologies of High Step-Up DC-DC converters and the topics addressed and definition of a topology for the converter from conventional topologies;
- Analyze voltage gain techniques and their application in the chosen topology;

- Propose a High Step-Up DC-DC converter with Coupled Inductor using ZVS technique;
- Analyze the operation principle of the derived converters and perform mathematical analysis of the converters;
- Design and dimensioning of the components and simulation of the converters in software;
- Implement the prototype of the converters and experimentally verify the operation.

1.7 WORK ORGANIZATION

This dissertation is organized as follows. Chapter 1 consists of an introduction, in which a synthetic view of global electrical energy generation and consumption and the situation of the energy system of Haiti is presented. Global warming is contextualized and the necessity to focus on renewable energies is highlighted. Then, Photovoltaic energy is presented as well as its growth during the last 10 years on the scale of global electrical energy generation. A brief review is presented on microinverters, high voltage gain and high efficiency DC-DC converters and a comparison between hard and soft switching losses in converters.

Chapter 2 presents a literature review of basic DC-DC converters and techniques for achieving high voltage gain and high efficiency.

Chapter 3 is dedicated to the analysis of the Quadratic ZVS Boost Flyback Converter where operation stages, voltage gain calculations, voltage and current stress of semiconductors and different waveforms are shown.

Chapter 4 presents the simulation and experimental results to validate the project analysis described in Chapter 3.

Chapter 5 presents the overall conclusion and a brief discussion of the objectives achieved and an outlook on topics that can be addressed in future work arising from this research.

2 LITERATURE REVIEW

This chapter presents a literature review about various techniques to achieve soft switching in high voltage gain converters, different techniques to increase the voltage gain; converters derived from conventional Quadratic Boost converter and those using coupled inductor method are presented in detail.

2.1 HIGH STEP-UP DC-DC CONVERTER BASED ON QUADRATIC BOOST CONVERTERS

The major disadvantage of conventional boost converters is their inability to operate with high duty cycle due to the limited switching frequency and minimum off-time of the transistors (HAIZHU; JIE, 2009; AXELROD; BERKOVICH; IOINOVICI, 2008). To overcome the above-mentioned drawbacks of the conventional boost converter, several techniques have been proposed to increase the voltage gain of conventional converters, such as; converters using inductor or/and switched capacitor cells, those using the voltage lift or/and voltage multiplier technique, converter based on conventional quadratic boost converter. The most studied group of high-gain converters is the ones based on coupled inductor. some converters based on quadratic circuit and coupled inductor method are presented below.

2.1.1 Conventional Quadratic Boost Converter

Conventional circuit diagram of Quadratic Boost Converter (QBC) is shown in Figure 2.1, is implemented by two series-connected converter with elimination of the second switch. Consisting of a single switch S, two inductors L_1, L_2, three diodes D_1, D_2 and Do and two capacitors C_i and C_o respectively. This quadratic boost converter can improve high voltage gain working with a single switch S (LEYVA-RAMOS; ORTIZ-LOPEZ; MORALES-SALDAñA, 2009). The QBC has two conduction modes of operation.

2.1.1.1 First Stage of operation

In the first stage of operation, the switch is ON, the diode D_2 is conducting, allowing the input inductor current i_i to flow through it, and the diodes D_1 and D_o are reverse biased. In this case, the inductor L_1 absorbs energy from the input source and the inductor

Figure 2.1 – Conventional Quadratic Boost converter

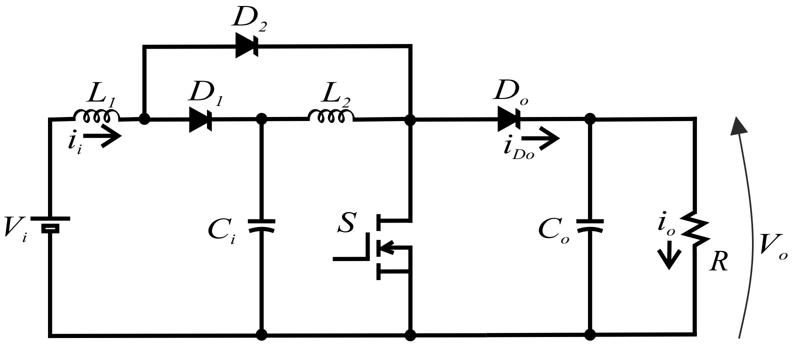

Source: Author

L_2 absorbs energy from the capacitor C_i. In the same time, the output capacitor C_o supplies energy to the load. The circuit topology for the first stage is given in Figure 2.2.

Figure 2.2 – Turn ON switching of conventional QBC

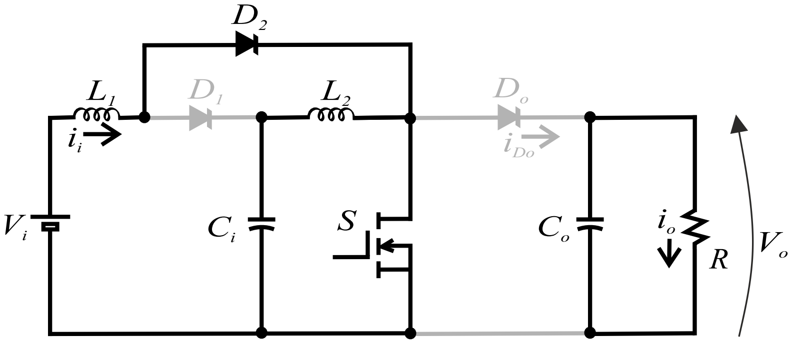

Source: Author

2.1.1.2 Second Stage of operation

At the end of the first stage of operation, the switch is turned OFF, diode D_2 is reverse biased, and diodes D_1 and D_o start conducting to allow the inductor L_1 and L_2 respectively charge capacitors C_i and C_o. Circuit diagrams for the turn OFF operation stage is shown in Figure 2.3.

By doing some mathematical analysis, passive components L_1, L_2, C_i and C_o can be designed by using these expressions below;

$$L_1 = \frac{V_i\,(1-D)^2}{2I_o f_s} \tag{2.1}$$

Figure 2.3 – Turn OFF switching of conventional QBC

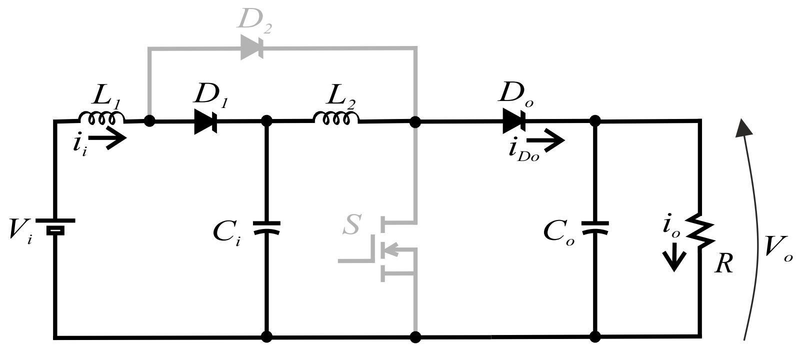

Source: Author

$$L_2 = \frac{V_i D}{2 I_o f_s} \tag{2.2}$$

$$C_i = \frac{I_o D}{(1-D)\,\Delta V_{C_i} f_s} \tag{2.3}$$

$$C_i = \frac{I_o D}{\Delta V_{C_i} f_s} \tag{2.4}$$

Where; D is the duty cycle, V_i and V_o are respectively the input and the output voltage, ΔV_{C_i} and ΔV_{C_o} respectively input and output capacitor ripple voltages and f_s the switching frequency.

2.1.1.3 Voltage Gain and Semiconductors Voltage and Current stresses

Voltage Gain, Voltage and Current stresses of Semiconductors can be expressed as follow (ANDRADE; MARTINS, 2017);

- Voltage Gain M;

$$M = \frac{V_o}{V_i} = \frac{1}{(1-D)^2} \tag{2.5}$$

- Voltage stress of the switch V_s;

$$V_s = \frac{V_i}{(1-D)^2} \tag{2.6}$$

- Current stress of the switch I_s;

$$I_s = 2 I_i \sqrt{D} \tag{2.7}$$

- Voltage stress of Output diode V_{D_o};

$$V_{D_o} = \frac{V_i}{(1-D)^2} \tag{2.8}$$

It can be noted as a disadvantage that, the efficiency of this converter is lower than the conventional boost converter due to the voltage stresses on the S switch is equal to the output voltage (WIJERATNE; MOSCHOPOULOS, 2012). However, by increasing the voltage gain of the conventional DC-DC boost converter, meaning that it requires a high duty cycle level, then its efficiency will drop significantly. In addition, the voltage stress on the switch will also increase (SAADAT; ABBASZADEH, 2016). Moreover, the high conversions ratio with the conventional converter causes electromagnetic interference due to the high level of duty cycle (PATIDAR; C.UMARIKAR, 2015). Also, as can be seen in equation 2.7, the current stress of the switch is twice the input current I_i. Since this converter operates in hard-switching mode, the switching losses will be high, consequently, the efficiency will decrease. However, this converter presents some advantage as simplicity of operation, single switch, continuous input current.

2.1.2 High step-up DC DC converter based on Conventional QBC

To avoid the mentioned limitations, several topology modifications of the conventional QBC have been investigated. Figure 2.4 depicts one of these topologies, which is a particular modification of the conventional quadratic Boost converter topology (JAHANGIRI; MOHAMMADPOUR; AJAMI, 2018). This high Step-Up DC-DC Boost converter with coupled inductor based on quadratic converters requires four diodes, three capacitors, one inductor, one coupled inductor with turn ratio N1/N2 and a single switch. In this converter, energy stored in the leakage inductor of the coupled inductor can be recycled through the passive voltage clamp circuit. Thus, the spike across the power switch is reduced and the conduction loss is decreased, leading to higher efficiency. Due to the fact that an input inductor is used in series with the input source, continuous current is flowing through it from the source. Consequently, a low current ripple is obtained.

2.1.2.1 Principle of Operation

There are four stages of operation for a switching period. The steady-state analysis of this converter is described in detail as follows.

Figure 2.4 – High Step-Up DC-DC Boost converter with coupled inductor based on quadratic converters

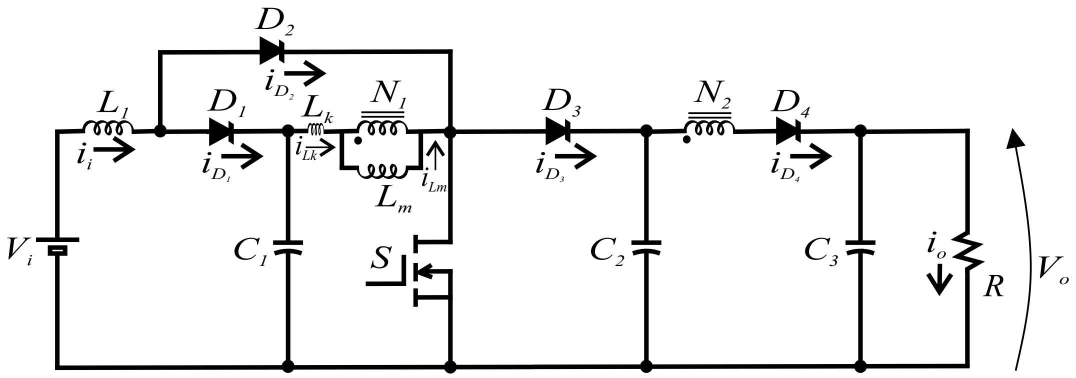

Source: Adapted from (JAHANGIRI; MOHAMMADPOUR; AJAMI, 2018)

- *Stage* 1 : $(t_0 \leq t \leq t_1)$;

During this stage, the switch S is ON and the diodes D_2 and D_4 are both forward biased. Magnetizing inductor current i_{L_m} decreases and the leakage inductor current i_{L_k} increases linearly. Capacitors C_1 and C_2 are discharged and the output capacitor C_3 is discharged to the load. This mode ends when the inductance currents i_{L_k} and i_{L_m} reach the same value.

- *Stage* 2 : $(t_1 \leq t \leq t_2)$;

In this stage, switch S and diode D_2 remain ON and diodes D_3 and D_4 are reverse biased. Capacitor C_1 is discharged towards the magnetizing inductor L_m and the leakage inductor L_k. From the input source, the input inductor is charged and capacitor C_3 is discharged to the load. This stage is ended when the switch is turned OFF.

- *Stage* 3 : $(t_2 \leq t \leq t_3)$;

During this stage, switch S is OFF and diodes D_1, D_3 and D_4 are forward biased. Capacitor C_1 is charged by the input source and the leakage inductor is discharged through diode D_3 to capacitor C_2. Energy from L_m is then released to C_3 through diode D_4 and the secondary winding of the coupled inductor. This stage is ended when the current of the leakage inductor drops to zero.

- *Stage* 4 : $(t_3 \leq t \leq T_s)$;

During the last stage, switch S is still OFF, diodes D_1 and D_4 are conducting and diodes D_2 and D_3 are reverse biased. From the input source, capacitor C_1 is charged. At the same time, capacitor C_1 is discharged and the energy of the magnetizing inductor is delivered to the load. This operation is terminated once the S switch is turned ON again to begin a new switching period.

By neglecting the leakage inductance, the voltage stress of the semiconductors during a Continuous Conduction Mode (CCM) operation are give by theses expressions below;

- Voltage Stress of the switch V_s;

$$V_s = \frac{V_o}{1 + ND} \tag{2.9}$$

- Voltage stress of diodes $V_{D_{i,i=1,..,4}}$;

$$V_{D_1} = \frac{DV_o}{1 + ND} \tag{2.10}$$

$$V_{D_2} = \frac{V_o\,(1 - ND)}{1 + ND} \tag{2.11}$$

$$V_{D_3} = \frac{V_o}{1 + ND} \tag{2.12}$$

$$V_{D_4} = \frac{V_o\,(2 - D + ND)}{1 + ND} \tag{2.13}$$

Voltage Gain and capacitor voltages are give by the following expressions;

- Voltage stress of diodes V_{C_i};

$$V_{C_1} = \frac{V_{in}}{1 - ND} \tag{2.14}$$

$$V_{C_2} = \frac{V_{in}}{(1 - D)^2} \tag{2.15}$$

- Voltage Gain M;

$$M = \frac{V_o}{V_i} = \frac{1 + ND}{(1 - D)^2} \tag{2.16}$$

This converter based on QBC can achieve high voltage gain compared to the conventional QBC shown in Figure 2.1, then it can be useful for PV applications due to the requirement of continuous current for renewable applications (CHEN; LIANG; CHEN, 2011).

The problem with this converter is the high value of current flowing through the switch and generates high losses in the leakage inductor of the coupled inductor.

2.2 HIGH STEP-UP DC-DC CONVERTER BASED ON COUPLED INDUCTOR

Coupling the inductor is the most practical way to achieve a higher conversion ratio. The development of new boost converters with coupled inductors is therefore the subject of much research. A coupled inductor has two or more windings on a common core. Coupled inductors operate in DC-DC converters by transferring energy from one winding to the other through the common core. They are available in a variety of sizes, inductance values and current ratings, and most are magnetically shielded to reduce electromagnetic interference (EMI). The windings may have equal (1:1) or unequal (1:N) turns. Some high voltage gain converters using coupled inductor are presented in this section.

2.2.1 Conventional Coupled Inductor-Based Boost Converter

The high voltage gain converter with coupled inductor shown in Figure 2.5 is derived from the conventional boost converter. A passive clamp circuit with one diode D_c and one capacitor C_c are added (ZHAO; LEE, 2003). Resonance may also be produced between the leakage inductor L_k and the capacitor C_c. Thus, during turn-off switching, when the inductor is not fully discharged in CCM, the leakage energy is first gathered in the capacitor C_c and then recycled to the output. This circuit is simple, and the switching voltage spike can be effectively blocked (PAULA; PEREIRA; TOFOLI, 2014). By adjusting the turn rate of the coupled inductor, a high voltage gain can be achieved for high turn ratio, however, the voltage spike across the D_o diode is very high, which results in using high cost semiconductors that intrinsically have a very high forward voltage drop and also a low switching speed.

The main features of this conventional boost based-on coupled inductor are the fact that it simple and effective, non-dissipative, and can achieve high conversion ratio and high efficiency with single switch and single magnetic element. Although it provides a higher voltage gain, its efficiency can be degraded due to the presence of the passive clamp circuit (LIU et al., 2016).

Figure 2.5 – High voltage gain boost converter with coupled inductor using passive clamp

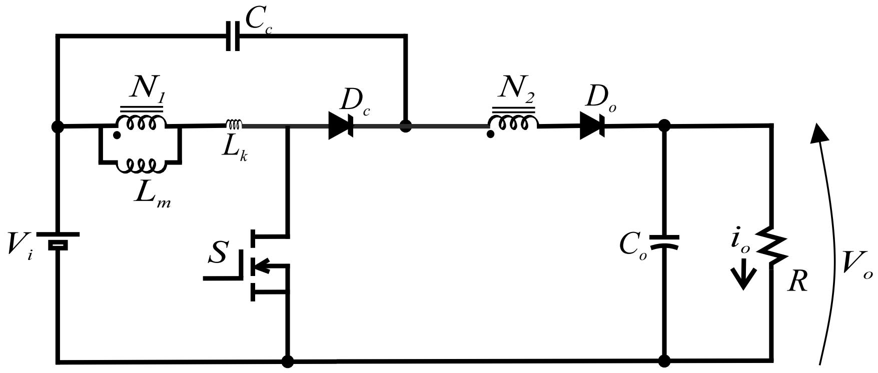

Source: Adapted from (ZHAO; LEE, 2003)

2.2.2 Stacked Boost-Flyback converter with coupled inductor

The flyback converter represents the isolated version of the buck-boost converter, it is a power supply topology that uses mutually coupled inductor, to store energy when current passes through and releasing the energy when the power is removed. Besides conferring galvanic isolation to the structure, provides a good feature in the static gain equation: its transformation ratio. Expression $\frac{ND}{1-D}$ allows determining the static gain of the ideal Flyback converter operating in CCM. It can be seen that, ideally, increasing the value of "N" allows increasing the value of the static gain without the need to increase the duty cycle too much. However, due to the high leakage inductor current of Flyback transformer which can degrade its efficiency, conventional Boost and Flyback converter can be associated in stacked connection as shown in Figure 2.6 (ZHAO; LEE, 2003) where the output terminal of Boost converter and output terminal of Flyback converter are serially connected to achieve high voltage Gain and avoid particular drawbacks of conventional converters mentioned above. Figure 2.6(a) shows the conventional stacked boost Flyback converter with coupled inductor, and its equivalent topology is depicted in Figure 2.6(b) where the primary side of the coupled inductor is designed as a controlled current source and the secondary side as a controlled voltage source to facilitate the mathematical analysis.

2.2.2.1 Operation analysis and mathematical analysis

To analyze the circuit, primary side and the secondary side of the coupled inductor are respectively designed as controlled current and voltage sources, the coupled inductor is modeled as an ideal transformer, which consists of a turn ratio of N_2/N_1, a magnetizing inductor L_m, and a leakage inductor L_k in the output of the secondary winding. The

Figure 2.6 – High step-up conventional Boost flyback converter with coupled inductor; (a) Basic circuit topology; (b) Equivalent circuit topology

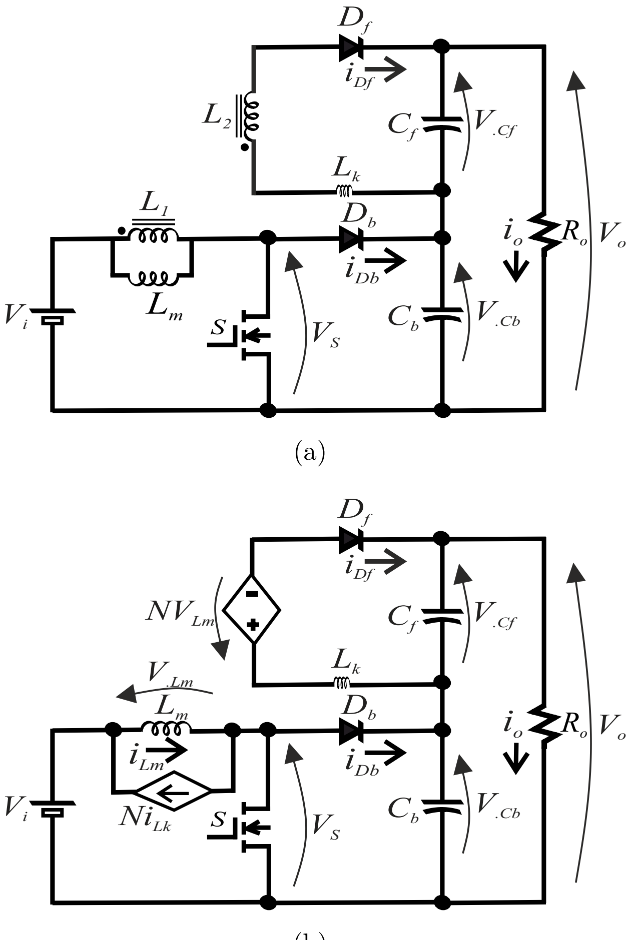

(a)

(b)

Source: Author

output capacitors C_b and C_f are supposed to be large enough to allow output voltages V_{C_b} and V_{C_f} to be considered constant throughout the switching cycle, thus, due to the stacked connection; $V_o = V_{C_b} + V_{C_f}$. Figure 2.7 shows theoretical waveforms of the converter operating in CCM, Figure 2.8 shows static gain waveforms by varying the turn ratio N using MATLAB software.

- *Stage* $1 : (t_0 \leq t \leq t_1)$;

At initial time, the switch is ON, Flyback diode starts to conduct. During this period, energy stored in the leakage inductor L_k is delivered to the load. By applying voltage divider, magnetizing inductor voltage is given by $(V_i L_m)/(L_m + L_k)$. At the end of this stage, Flyback diode is reverse biased, in the same time where the leakage energy is completely discharged magnetically to the load.

- *Stage* 2 : $(t_1 \leq t \leq t_2)$;

At t_1, the switch remains ON, diodes D_b and D_f are reverse-biased. Output capacitors C_b and C_f supply energy to the load. This stage will end when the magnetizing current reaches its peak value.

- *Stage* 3 : $(t_2 \leq t \leq t_3)$;

During the third mode of operation, the switch is turned OFF. Magnetizing current starts to charge the parasite capacitor of the switch, when the voltage of this capacitor is more than the output voltage of the boost capacitor, this stage is ended, and instantaneously Boost and Flyback diodes start to conduct.

- *Stage* 4 : $(t_3 \leq t \leq T_s)$;

In the last stage, diodes D_f and D_b are forward-biased. Diode D_b takes over all the current that was flowing through the switch, since the current at diode D_f has its growth limited by the leakage inductor L_k.

The output voltage is the sum of output voltage of Boost and Flyback capacitors.

$$V_{C_b} = \frac{1}{(1-D)} V_i \tag{2.17}$$

$$V_{C_f} = \frac{ND}{(1-D)} V_i \tag{2.18}$$

$$V_o = V_{C_b} + V_{C_f} = \frac{1+ND}{(1-D)} V_i \tag{2.19}$$

Converters shown in Figures 2.5 and 2.6 depend mostly on magnetic coupling to obtain high voltage gain. However, the Boost Flyback converter with coupled inductor can achieve high voltage gain due to its robust structure. Basic converters have several advantages for applications that require high voltage gain converters, such as;

- They have a simple structure, they operate with a single switch, and their implementation or system cost is low.
- The leakage inductance of the coupled inductor helps mitigate the reverse recovery problem of the rectifier diodes to enhance good efficiency.
- They provide a high step-up voltage gain according to equation (2.19) and the switching voltage stress is low according to equation (2.17).

Figure 2.7 – Theoretical waveforms of Conventional Boost Flyback converter with coupled inductor

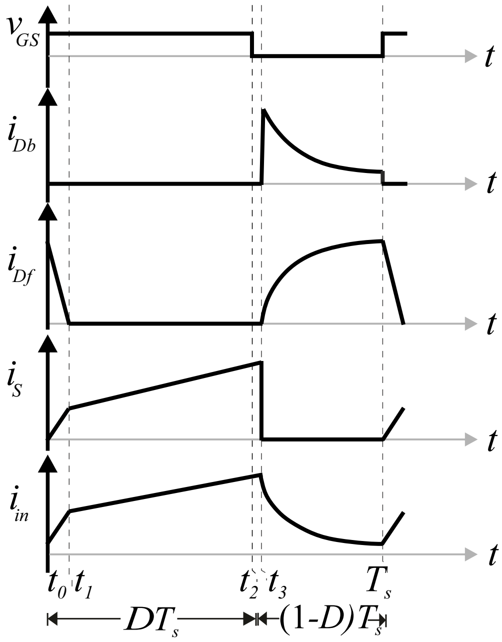

Source: Author

However, conventional coupled inductor boost converters always have the following drawbacks.

- The non-ideal coupling of the inductor unavoidably introduces a leakage inductance, which can cause high voltage spikes across the switch and diodes.
- The voltage gains of converters depend on the turn ratio of the coupled inductor. Several drawbacks occur when using the turn ratio to achieve extreme voltage gain, large magnetic core volume and large leakage inductance resulting in higher resonances and voltage spikes;
- high input current ripples, switching current stresses, conduction losses that can degrade the efficiency.
- Theoretical input current waveforms is shown in Figure 2.7. From this, it can be observed that the input current ripples is high, at high turns ratio in particular. High input current ripple can have many adverse effects, such as high conduction losses, impact on the lifetime of renewable energy devices, etc.

Due to these disadvantages suffered by conventional coupled inductor converters, a new high step-up DC-DC converter combining stacked boost flyback, quadratic circuit and a resonant cell to achieve soft switching and high voltage gain.

Figure 2.8 – Voltage Gain curve of Conventional Boost Flyback converter with coupled inductor by varying the turn ratio

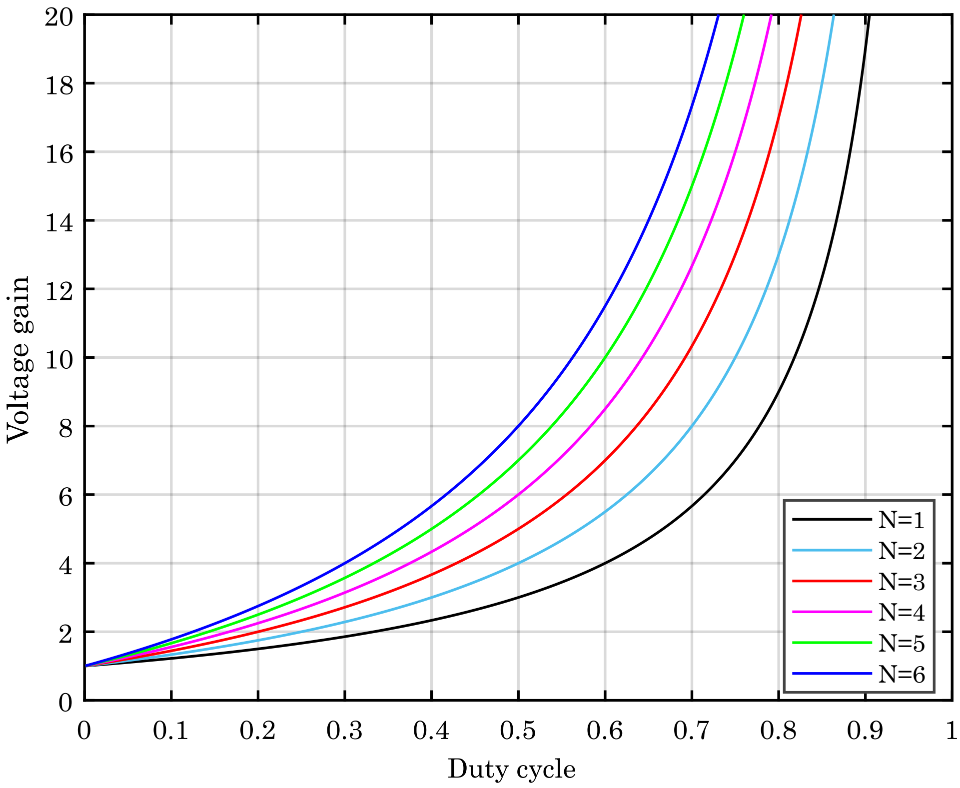

Source: Author

2.2.3 Stacked Boost-Flyback converter with coupled inductor and resonant cell

This converter shown in Figure 2.9 is obtained by adding a resonant cell to the conventional Boost Flyback converter. With this converter, was started this work at first, it was proposed in for this dissertation, but which will be modified later, due to some drawbacks.

A two components $L - C$ resonant cell is added, allows to achieve ZVS across the switch and ZCS through semiconductor diodes at switching transitions and also allows to achieve high voltage gain with low duty ratio. However, this converter has a significant drawback where the current from the switch is flowing back to the input source, which causes high losses decreasing the efficiency.

Figure 2.9 – Boost Flyback converter with coupled inductor and resonant cell

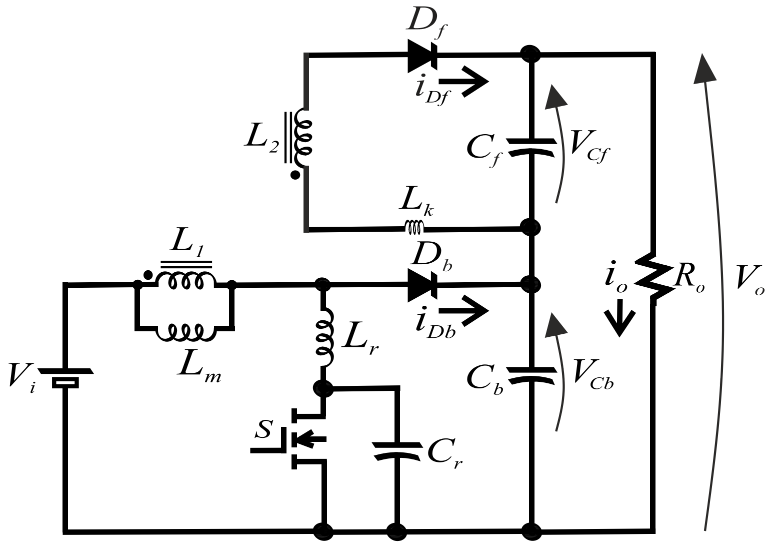

Source: Author

2.3 SOFT-SWITCHING TECHNIQUE

Switching power losses in power converters are due to the increasing of high level switching frequency, switching power losses cause rising temperature and reduce the efficiency of power conversion. Power dissipation through the switch arises because during the switching transition from ON to OFF or vice versa, the voltage across the switch and the current through it have non zero finite values (VITHAYATHIL, 1995). When the semiconductors are turned ON, their voltage decreases and their current increases at the same time. In contrast, when semiconductors turn OFF, their voltage increases and their current decreases at the same time. Device stress is increased as the switching locus moves into the active region of the safe operating area (AHMAD; SINGH, 2012). Zero current switching (ZCS), Zero voltage switching (ZVS), Zero voltage transition (ZVT), Zero current transition (ZCT) methods are commonly used to create soft switching in conventional pulse width modulation (PWM) converters using auxiliary circuits.

2.3.1 Zero Voltage Switching

Zero voltage switching can best be defined as conventional square wave power conversion during the switch's on-time with resonant switching transitions. In a ZVS resonant switch as shown in Figure 2.10(a) resonant inductor is in series with the parallel combination between the switch and resonant capacitor. ZVS is strongly used in high step-up DC-DC converter to overcome hard switching losses. At turn OFF of the switch, the current is diverted from the switch into the resonant capacitor, the gradual in increase of the voltage across the resonant capacitor minimizes overlapping to the current switch and voltage at turn OFF (TABISZ; LEE, 1989). ZVS can achieves some give feature for high step-up DC DC converter; Zero power losses in switching transition, reduce EMI at transition, high efficiency with high voltage, no higher peak current in semiconductors, eliminate power losses causes by the leakage inductance in converter based on coupled inductor.

2.3.2 Zero Current Switching

Quasi-resonant switching is a good technique for improving voltage-converter efficiency, but things can be further improved by implementing full soft switching. During soft switching the voltage falls to zero (rather than just a minimum) before the MOSFET is turned on or off, eliminating any overlap between voltage and current and minimizing losses(VITHAYATHIL, 1995). The technique can also be used to switch the MOSFET when current, rather than voltage, reaches zero. This is known as Zero Current Switching (ZCS). A ZCS topology is depicted in Figure 2.10(b)

Figure 2.10 – Soft-switching techniques using; (a) ZVS resonant circuit; (b) ZCS resonant circuit

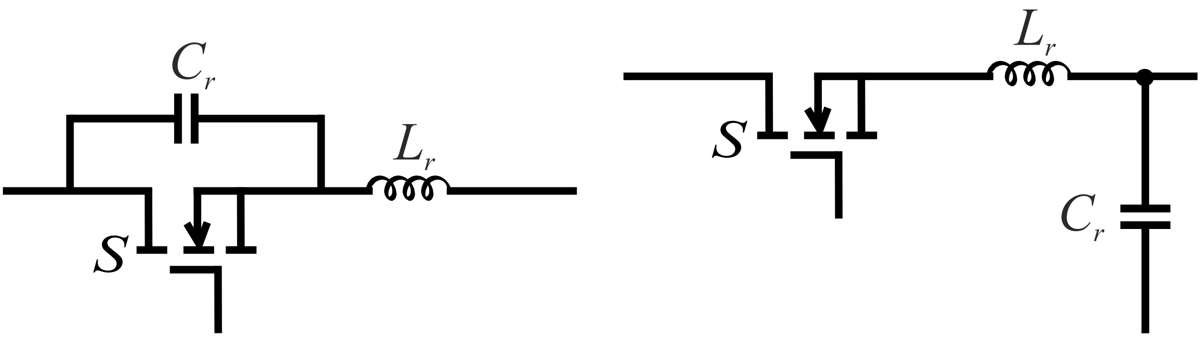

(a) (b)

Source: Author

Several two components resonant cell circuits depicted in Figure 2.11 (HUANG; FU; LEE, 2011) allow to apply better ZVS for high gain ratio and high efficiency.

Two components $L - C$ resonant circuit allow to form resonant tank to achieve ZVS and ZCS in power converters, there are eight combinations to form these resonant cell and can well perform either resonant frequency is less than switching frequency, either resonant frequency is more than switching frequency (HUANG; FU; LEE, 2011).

There are three fundamental resonant elements that are found in resonant converters: Series resonance, parallel resonance and notch resonance.

Figure 2.11 – Eight configurations of two storage elements resonant tank:(a) Tank A; (b) Tank B; (c) Tank C; (d) Tank D; (e) Tank E; (f) Tank F; (g) Tank G; (h) Tank H

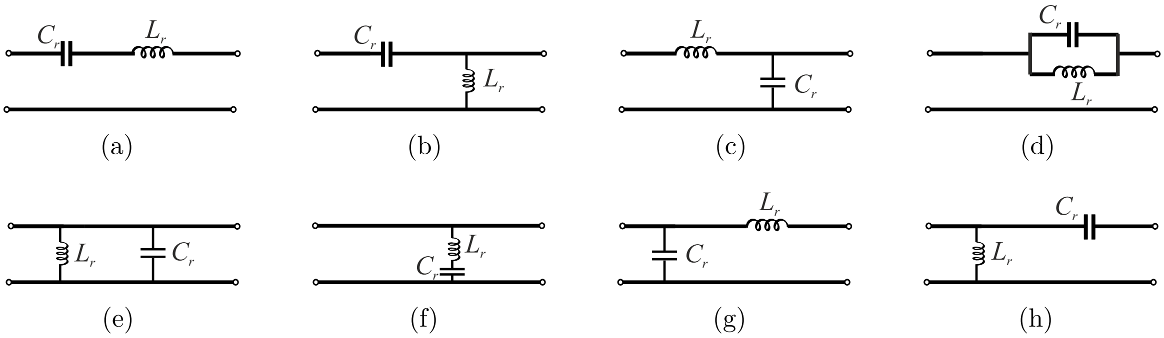

Source: Adapted from (HUANG; FU; LEE, 2011)

Basic series resonance consists of two series connected resonant elements between input and output. Series resonance doesn't help to amplify the input signal. Instead, it provides a buck function, in that the gain can only be unity or lower. Below and above the resonant frequency, the input-output gain is less than unity. Therefore, the series resonance provides a step-down function like a buck converter. A basic series resonant tank of Figure 2.11(a) and its gain curve are shown in Figure 2.12.

Figure 2.12 – Basic series resonant tank gain curves

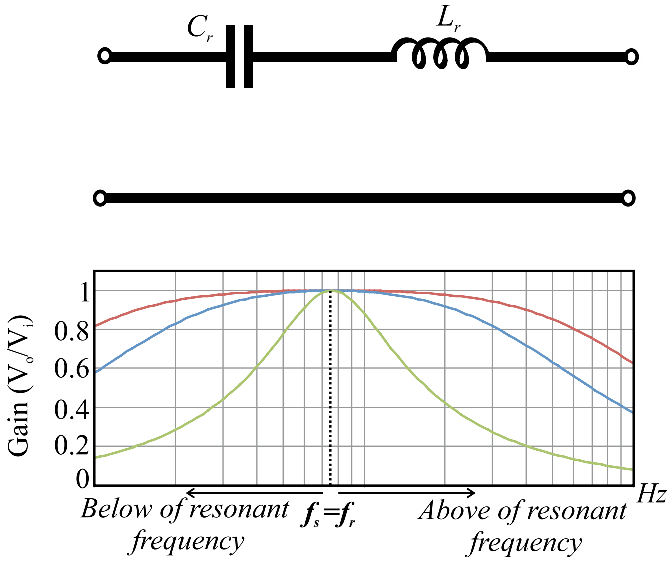

Source: Texas Instruments

Parallel resonance consists of at least one series connected resonant element between input and output and one parallel connected resonant element. Parallel resonance is able to amplify or boost the input signal and provide high gain nearby the resonant frequency. The basic parallel resonant tanks of Figures 2.11(b) and 2.11(c) and their gain curves are shown in Figure 2.13. They allow to achieve high voltage gain around the resonant frequency, ZVS above resonant frequency and ZCS below resonant frequency. They can be used in applications required a high voltage step-up function.

Figure 2.13 – Basic parallel resonant tanks and their gain curves.

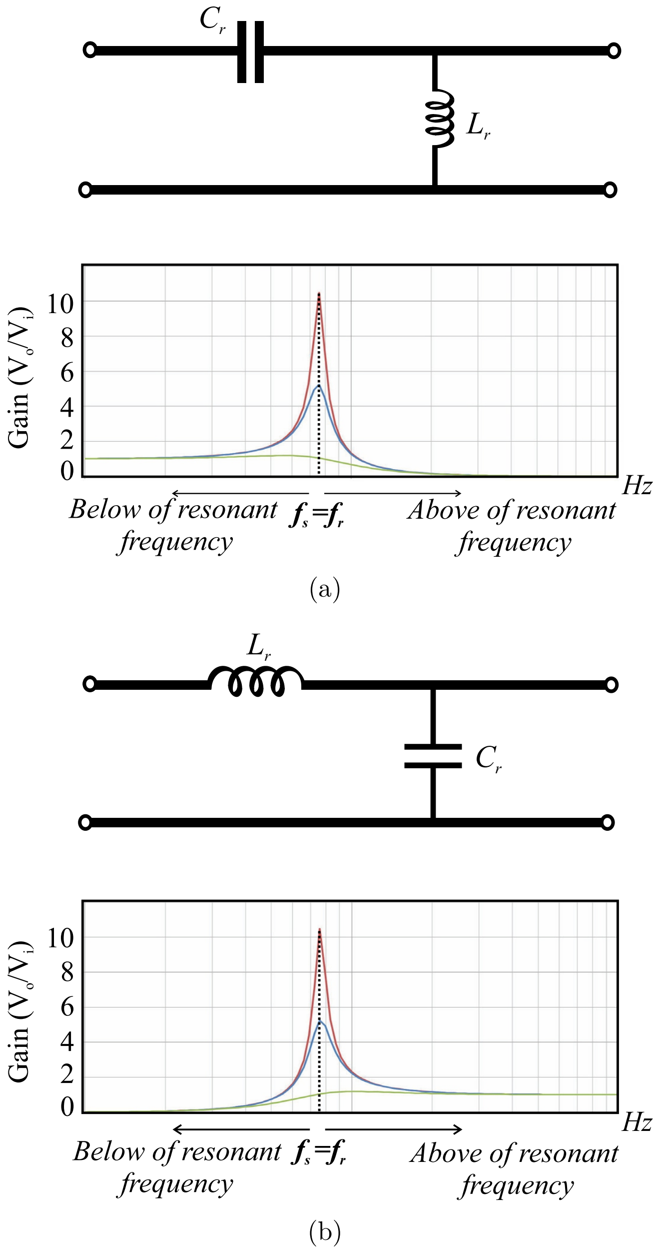

Source: Texas Instruments

Notch resonance consists of either two parallel connected resonant elements between the input and output or two series connected resonant elements with one end tied to the common node. Like series resonance, notch resonance provides unity or less than unity gain. However, unlike series resonance, the gain dramatically decreases nearby the notch resonant frequency. Basic notch resonant tank of Figure 2.11(d) and its gain curves is shown in Figure 2.14. Table 2.1 shows the advantages and disadvantages of the resonant tanks illustrated in Figure 2.11.

Figure 2.14 – Basic notch resonant tank gain curve

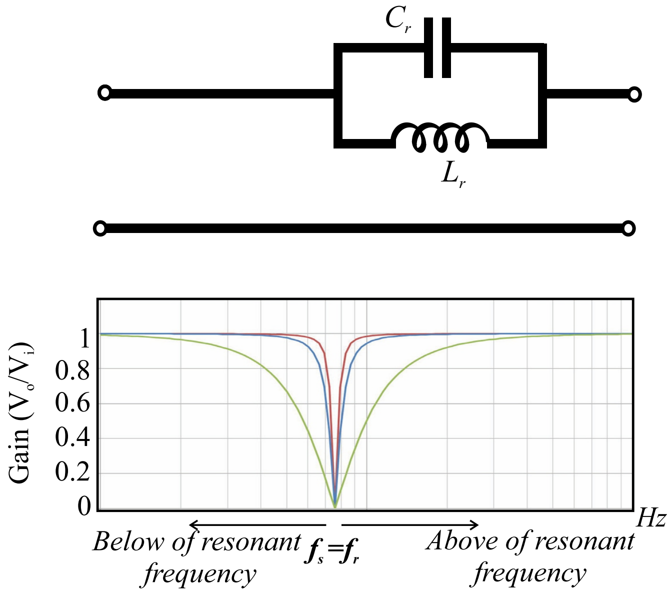

Source: Texas Instruments

Table 2.1 – Advantages and disadvantages of each resonant tank

Tank	Advantages	Disadvantages
Tank A	Zero Voltage Switching (ZVS) above resonant frequency Zero Current Switching (ZCS) below resonant frequency Low circulating energy turn OFF current at resonant frequency	Light load regulation High circulating energy Turn OFF current at high input voltage condition
Tank B and C	Zero Voltage Switching (ZVS) above resonant frequency Zero Current Switching (ZCS) below resonant frequency High voltage gain around resonant frequency	High circulating energy Turn OFF current at high input voltage condition
Tank D	Zero Voltage Switching (ZVS) above resonant frequency Zero Current Switching (ZCS) below resonant frequency	Becoming an open circuit at resonant frequency Voltage gain becomes zero at the resonant frequency
Tank E and F	Unity voltage gain for various switching frequency	Inability to regulate power transferred to the load.
Tank G	Close to Unity voltage gain at no load	Inability to regulate power transferred to the load. Voltage gain below 1 by increasing switching frequency
Tank H	Unity voltage gain by increasing switching frequency	No longer a resonant topology. Clamping of inductance by the voltage source Any resonance between inductor and capacitor

2.4 PARTIAL CONCLUSION

This chapter presents the analysis of some topologies of high voltage gain converters such as the conventional quadratic converter which certainly allows to find a high voltage gain value, but which is limited due to its high voltage stress which significantly decreases its efficiency, the Quadratic Boost converter with coupled inductor has also been analyzed, although it allows to reach a better voltage gain and a better efficiency than the conventional quadratic converter, The problem with this converter is that a high voltage gain means an increase of the turn ratio of the coupled inductor, which will increase the leakage inductance and will generate huge losses. A resonant tank has been added to the boost flyback converter to decrease losses due to leakage inductance, but when the switch is turned ON, its current is flowing back to the source, which decreases the efficiency of the converter.

3 ANALYSIS OF QUADRATIC ZVS BOOST-FLYBACK CONVERTER

This chapter presents the operating stages of the Quadratic ZVS Boost Flyback converter, its static gain, and semiconductor voltage and current stresses in continuous conduction mode (CCM). The circuit of the proposed converter is shown in Figure 3.1 consisting of a switch S, Two diodes D_b and D_f, two output capacitors C_b and C_f large enough to provide constant voltages, a dual-winding coupled inductor replaced by its electrical model with a leakage inductor placed in the secondary winding, a magnetizing inductor placed in parallel to a current source in the primary winding and a reverse voltage source at the secondary. A quadratic circuit consisting of an input inductor L_i , two diodes D_1 and D_2 and a filter capacitor C_i is added to the Zero Voltage Switching (ZVS) Boost-Flyback converter to block the reverse current flowing to the source, a resonant circuit composed by a resonant capacitor C_r in parallel with the switch S and a resonant inductor L_r in series with the parallel combination of the switch with the aim to achieve ZVS and soft-switching losses.

Figure 3.1 – Quadratic ZVS Boost-Flyback converter

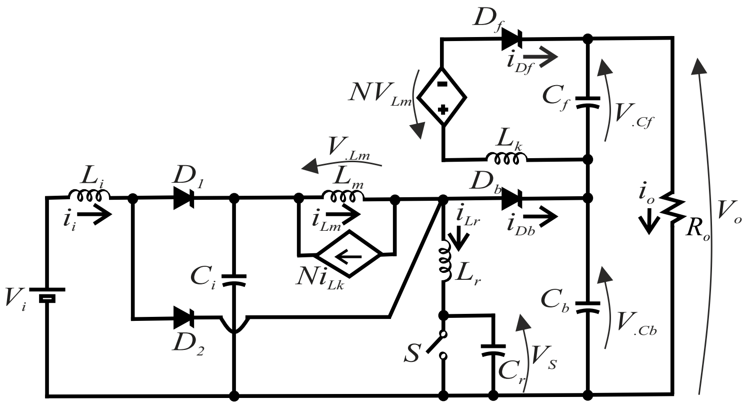

Source: Author

3.1 ZVS BEHAVIOR

To better understand the resonant tank, some terms are used for better analysis.

- Resonant and normalized switching frequency

The resonant frequency W_r of the two resonant circuit components $L_r - C_r$ is defined by:

$$w_r = 2\pi f_r = \frac{1}{\sqrt{L_r C_r}} \tag{3.1}$$

The normalized switching frequency A is the ratio of the operating angular frequency w_s and the resonant angular frequency w_r:

$$A = \frac{w_s}{w_r} = \frac{2\pi f_s}{2\pi f_r} = \frac{f_s}{f_r} \tag{3.2}$$

- Normalized initial resonant inductor and switch current

The factor h is the initial resonant inductor and switch currents when the switch turns on, it is the ratio of the initial current flowing in the switch $i_s(0)$ and the input current at turn-on switching I_i.

If $i_s(0) > 0$ then;

$$h = \frac{i_s(0)}{I_i} > 0 \tag{3.3}$$

If $i_s(0) < 0$ then;

$$h = \frac{i_s(0)}{I_i} < 0 \tag{3.4}$$

If $i_s(0) = 0$ then;

$$h = \frac{i_s(0)}{I_i} = 0 \tag{3.5}$$

The proposed converter can operate in three different modes depending on the value of the normalized initial resonant inductor and switch current h, which can decrease or increase the voltage gain.

- The first mode shown in Figure 3.2 is obtained when $h < 0$. In this mode the converter achieves ZVS. At turn ON of the switch S, the current of the switch is negative, which means that the current from the resonant inductor is flowing back to the input source. This option decreases the voltage gain of the converter.

- The second mode is represented by Figure 3.3 when $h > 0$. For this mode, the resonant switching frequency is very higher than switching frequency. Consequently the voltage of the switch achieves negative value. Besides that, at the turn ON of the switch, the switch presents a current spike. This mode increase the current stress of the switch and also decrease the voltage gain of the converter.

- The third mode shown by Figure 3.4 for $h = 0$, is the ideal for the proposed converter, the voltage of the switch reaches zero at turn ON and turn OFF, the current of the switch starts to zero when the switch is turning ON. In addition, this option achieves high voltage gain.

To demonstrate in detail the mathematical analysis, voltage gain, voltage and current stresses in semiconductors, the third mode is chosen to evaluate the Quadratic ZVS Boost Flyback Converter.

Figure 3.2 – Switch Current and Voltage waveforms when $h < 0$.

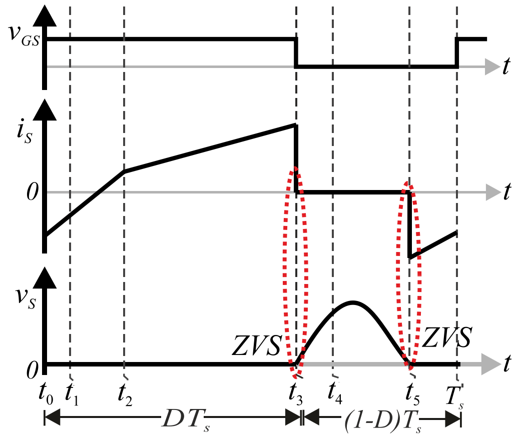

Source: Author

Figure 3.3 – Switch Current and Voltage waveforms when $h > 0$.

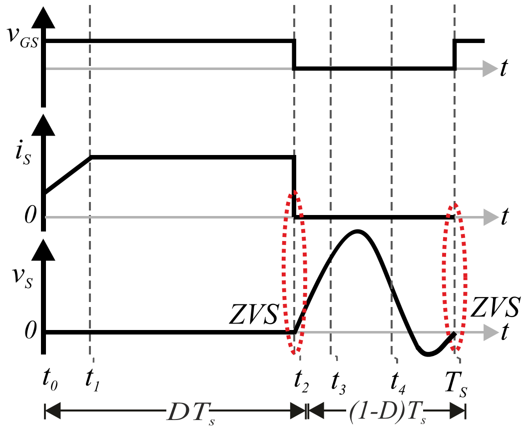

Source: Author

3.2 OPERATING PRINCIPLE IN CONTINUOUS CONDUCTION MODE

To facilitate the analysis of the converter, some of the following assumptions are stated.

Figure 3.4 – Switch Current and Voltage waveforms when $h = 0$.

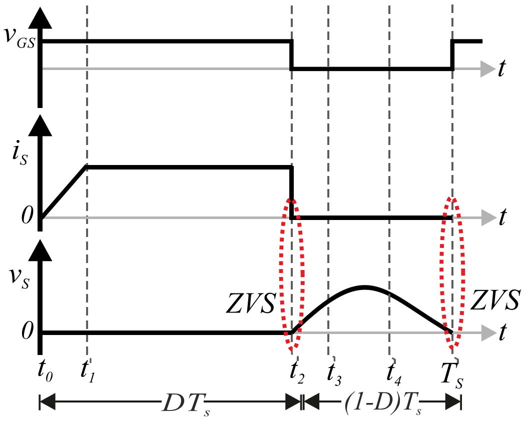

Source: Author

a) All components are considered ideal, except for the leakage inductor in the secondary winding of the coupled inductor.

b) All capacitors are large enough, and their voltages are considered to be constant over a switching period.

c) The turns ratio N of the coupled is equal to N_2/N_1 with N_1, the turn number of the primary winding and N_2, the turn number of the secondary winding.

Figure 3.5 presents the operating stages of the Quadratic ZVS Boost-Flyback converter at turn ON switching, Figure 3.6 presents the operating stages of the Quadratic ZVS Boost-Flyback converter at turn OFF switching and Figure 3.7 presents the main waveforms of the converter operating in continuous conduction mode.

3.2.1 Stage 1: $(t_0 \leq t \leq t_1)$

During the first stage, the switch S is conducting. The energy of the DC source V_i is transferred to the input inductor L_i through the diode D_1 in which, total input current is flowing. Thus, the inductor L_m is magnetized by the input filter capacitor C_i and transfers its energy to the Flyback charging capacitor C_f through the secondary leakage inductor L_k. Diodes D_2 and D_b are reverse biased and resonant capacitor is clamped by turn-ON switching. In the same time, current in secondary winding of the coupled inductor starts to decrease linearly until reaching zero value, then starts instantaneously the second stage of operation. Figure 3.5(a) shows the equivalent circuit of this stage.

By using Kirchhoff Voltage Law, voltage in the secondary winding V_{N_2} of the coupled inductor can be obtained.

$$V_i - L_i\frac{di_i}{dt} - L_m\frac{di_{L_m}}{dt}L_r\frac{di_{L_r}}{dt} = 0 \tag{3.6}$$

By applying Kirchhoff Voltage Law in the Flyback loop;

$$V_{N_2} - V_{L_k} + V_{C_f} = 0 \tag{3.7}$$

Inductance of the leakage inductor is very low and with low ripple current, then;

$$V_{N_2} = V_{L_k} - V_{C_f} \approx -V_{C_f} \tag{3.8}$$

Voltage in secondary winding of the coupled inductor is equal to the turn ratio N times the the primary winding voltage V_{L_m}, given that the voltage of the secondary winding V_{N_2} is reversed, then:

$$\begin{cases} V_{N_2} = NV_{L_m} = -V_{C_f} \\ V_{L_m} = \frac{-V_{C_f}}{N} \end{cases} \tag{3.9}$$

The magnetizing current is defined as;

$$i_{L_m}(t) = \frac{V_{L_m}}{L_m}t + I_{L_m}(t_0) = \frac{-V_{C_f}}{NL_m}t + I_{L_m}(t_0) \tag{3.10}$$

By applying voltage divider, the resonant inductor voltage is obtained by (3.11) or (3.12);

$$v_{L_r} = \frac{L_r}{L_m + L_i + L_r}V_i = k_1V_i \tag{3.11}$$

or

$$v_{L_r} = \frac{L_r}{L_m + L_r}V_{C_i} = k_2V_{C_i} \tag{3.12}$$

with $k_1 = L_r/(L_m + L_i + L_r)$ and $k_2 = L_r/(L_m + L_r)$

Then, the resonant inductor current can be expressed as follow;

$$i_{L_r}(t_1) = \frac{k_1V_i}{L_r}(t_1 - t_0) + I_{L_r}(t_0) = \frac{k_2V_{C_i}}{L_r}(t_1 - t_0) + I_{L_r}(t_0) \tag{3.13}$$

i_{L_r} can be defined also as;

$$i_{L_r} = i_{L_m} - i_{p_1} \tag{3.14}$$

with i_{p_1}, the primary winding current of the coupled inductor.

By using (3.14),(3.13) and (3.10), the current in the secondary winding of the coupled inductor is defined as;

$$i_{L_k}(t) = \frac{i_{p_1}(t)}{N} = \frac{i_{L_m}(t) - i_{L_r}(t)}{N} \tag{3.15}$$

$$i_{L_k}(t) = \frac{\frac{V_{C_f}}{NL_m}t + I_{L_m}(t_0) - \frac{k_2 V_{C_i}}{L_r}t - I_{L_r}(t_0)}{N} \tag{3.16}$$

$$i_{L_k}(t_1) = \frac{\left(L_r V_{C_f} - NL_m k_1 V_i\right)(t_1 - t_0) + N^2 L_m L_r \left(IL_m\left(t_0\right) - IL_r\left(t_0\right)\right)}{N^2 L_m L_r} \tag{3.17}$$

At the end of this stage, (3.17) is equal to zero, then the duration of the first stage is given by (3.18)

$$(t_1 - t_0) = \frac{N^2 L_m L_r \left(I_{L_r}(t_0) - I_{L_m}(t_0)\right)}{L_r V_{C_f} - NL_m k_1 V_i} \tag{3.18}$$

3.2.2 Stage 2: $(t_1 \leq t \leq t_2)$

The second stage of operation starts when the current of the Flyback output diode reaches zero value. The switch remains conducting. Instantaneously, a part of the input current is flowing across diode D_2 by increasing linearly. In contrast, the inductor L_m continues to be magnetized by the input capacitor C_i. Output Flyback and Boost diodes D_f and D_b are reverse biased and capacitors C_f and C_b supply energy to the load. When the current across diode D_1 achieves zero value, this stage ends and immediately starts the last stage of turn-ON switching. The equivalent topology for this stage is shown by Figure 3.5(b).

Voltages of input capacitor, resonant inductor and magnetizing inductor are defined by (3.19), (3.20) and (3.21) respectively.

$$V_{C_i} = V_i - V_{L_i} \tag{3.19}$$

$$V_{L_r} = V_i - V_{L_i} \tag{3.20}$$

$$V_{L_m} = V_{C_i} - V_{L_r} \tag{3.21}$$

In the second stage of operation, input current divided into two parts, i_{D_1} which started to increase linearly and i_{D_2} which started instantaneously decreasing linearly as defined by;

$$i_i = i_{D_1} + i_{D_2} \tag{3.22}$$

Current in semiconductors are defined by these equations below;

$$i_{D_b} = 0 \tag{3.23}$$

$$i_{D_f} = 0 \tag{3.24}$$

$$i_S(t) = i_{L_r}(t) \tag{3.25}$$

3.2.3 Stage 3: $(t_2 \leq t \leq t_3)$

At t_2, the switch is still ON, diode D_1 stops to conduct and diode D_2 continues to increase linearly until reaching its maximum value. Diodes D_b and D_f remains OFF and output capacitors continue to supply energy to the load. At the end of this stage, the switch is turned OFF. Figure 3.5(c) shows the equivalent circuit of this stage.

Equations (3.26) and (3.27) are obtained by applying Kirchhoff Voltage law;

$$V_i - V_{L_i} - V_{L_r} = 0 \tag{3.26}$$

$$V_{C_i} - V_{L_m} - V_{L_r} = 0 \tag{3.27}$$

Using voltage divider, voltages voltages V_{L_r}, V_{L_r} and V_{L_r} are expressed as below

$$V_{L_i} = \frac{L_i}{L_i + L_r} V_i = k_3 V_i \tag{3.28}$$

$$V_{L_r} = \frac{L_r}{L_i + L_r} V_i = (1 - k_3) V_i \tag{3.29}$$

$$V_{L_m} = \frac{L_m}{L_m + L_r} V_{C_i} = k_4 V_{C_i} \tag{3.30}$$

$$V_{L_r} = \frac{L_r}{L_m + L_r} V_{C_i} = (1 - k_4) V_{C_i} \tag{3.31}$$

where, k_3 is the coefficient given by the ratio between input inductor L_i and the sum of resonant inductor L_r and the input inductor. k_4 is the coefficient given by the ratio between magnetizing inductor L_m and the sum of the resonant inductor L_r and the magnetizing inductor.

By substituting (3.29) in (3.31), then the input capacitor voltage can be obtained by (3.32)

$$V_{C_i} = \frac{L_m + L_r}{L_i + L_r} V_i \tag{3.32}$$

By combining (3.30) and (3.32), the magnetizing current is defined by (3.33).

$$i_{L_m}(t_3) = \frac{V_{L_m}}{L_m} t + I_{L_m}(t_2) = \frac{V_i}{L_i + L_m} (t_3 - t_2) + I_{L_m}(t_2) \tag{3.33}$$

By using (3.28), the resonant inductor current is defined by (3.34).

$$i_{L_r}(t_3) = \frac{V_{L_r}}{L_r} t + I_{L_r}(t_2) = \frac{V_i}{L_i + L_r} (t_3 - t_2) + I_{L_r}(t_2) \tag{3.34}$$

Current across semiconductors;

$$i_{D_1} = 0 \tag{3.35}$$

$$i_{D_2} = i_i = \frac{P_o}{V_i} \tag{3.36}$$

$$i_S(t_3) = i_{L_r}(t_3) = \frac{V_{L_r}}{L_r} t + I_{L_r}(t_2) = \frac{V_i}{L_i + L_r} (t_3 - t_2) + I_{L_r}(t_2) \tag{3.37}$$

$$i_{D_b} = 0 \tag{3.38}$$

$$i_{D_f} = 0 \tag{3.39}$$

Voltage across diode D_1 is defined by (3.40).

$$V_{D_1} = V_i - V_{L_i} - V_{C_i} = \frac{L_m}{L_i + L_r} V_i \tag{3.40}$$

Figure 3.5 – TURN ON Stages of operation of Quadratic ZVS Boost-Flyback converter. (a) First Stage ($t_0 \leq t \leq t_1$). (b) Second Stage ($t_1 \leq t \leq t_2$). (c)Third Stage ($t_2 \leq t \leq t_3$).

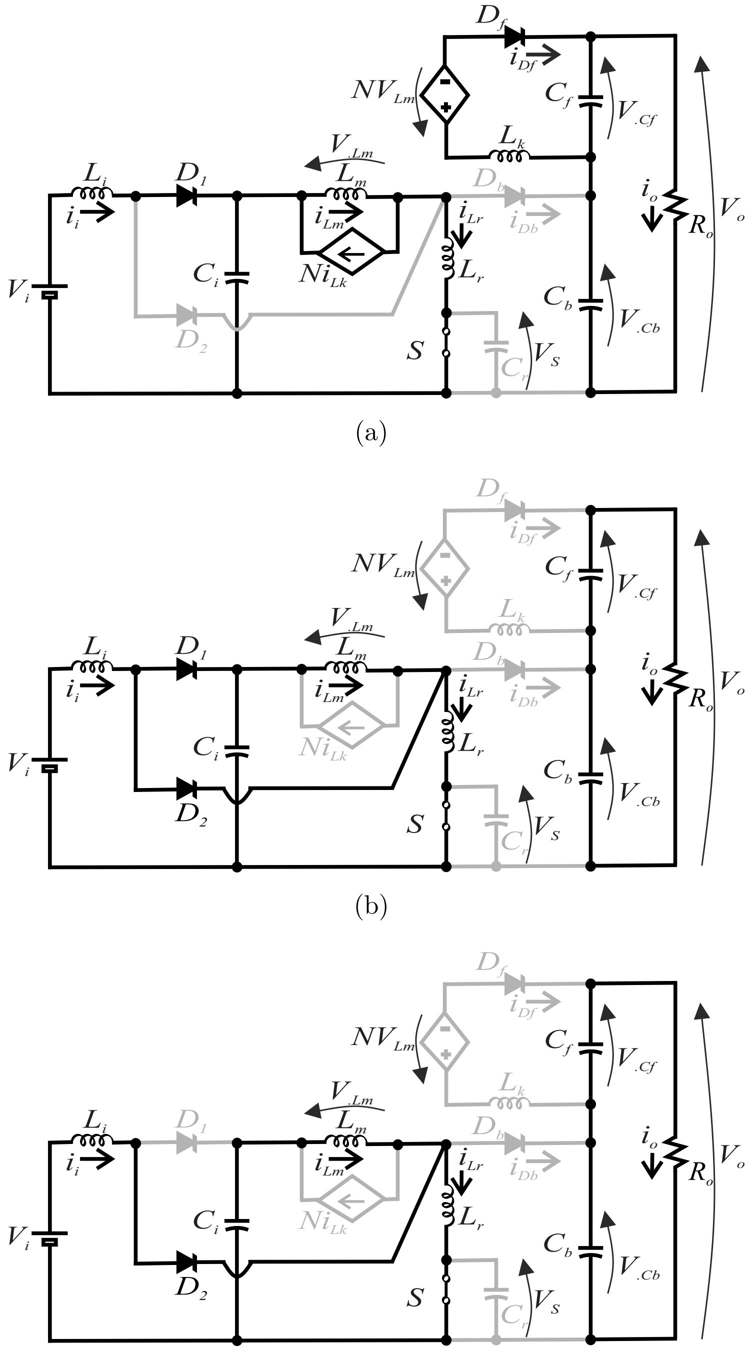

(a)

(b)

(c)

Source: Author

3.2.4 Stage 4: $(t_3 \leq t \leq t_4)$

At t_3, this stage begins when the switch is turned OFF. Only diode D_2 is conducted and all other diodes D_1, D_b and D_f are reverse biased. Energy from the DC source V_i is still stored in the input inductor L_i through diode D_2. The energy that charged the capacitor C_i is always supplied to the magnetizing inductor L_m. During this interval, starts the resonant stage of operation where the resonant capacitor starts to charge linearly and the resonant inductor current is constant during this time. Energy stored in capacitors C_b and C_f continues to be discharged to the load R_o. This mode is ended when diode D_1 starts to conduct. The equivalent circuit of this stage is shown in Figure 3.6(a).
At the beginning of this stage, the switch is turned OFF. The resonant capacitor starts to charge linearly.

The resonant circuit of the converter can be described by the formulas in (3.41), (3.42) and (3.43).

- Characteristic impedance of the resonant circuit

$$Z_r = \sqrt{\frac{L_r}{C_r}} \tag{3.41}$$

- The resonant angular frequency

$$w_r = \frac{1}{\sqrt{L_r C_r}} \tag{3.42}$$

- The resonant frequency

$$f_r = \frac{1}{2\pi\sqrt{L_r C_r}} \tag{3.43}$$

The switch is turned OFF, circuit topology of other semiconductor components in Figure 3.6(a) of the fourth stage is the same as in Figure 3.5(c) of the third stage. In fact , the resonant current and the magnetizing current keep constant. Then:

$$i_{L_m}(t_4) = \frac{V_{L_m}}{L_m} t + I_{L_m}(t_2) = \frac{V_i}{L_i + L_m}(t_4 - t_3) + I_{L_m}(t_2) \tag{3.44}$$

$$I_{L_r}(t_4) = \frac{V_{L_r}}{L_r} t + I_{L_r}(t_2) = \frac{V_i}{L_i + L_r}(t_4 - t_3) + I_{L_r}(t_2) \tag{3.45}$$

Current in semiconductors except diode D_2 is null, in fact:

$$i_{D_f} = 0 \tag{3.46}$$

$$i_{D_b} = 0 \tag{3.47}$$

$$i_{D_1} = 0 \tag{3.48}$$

$$i_S = 0 \tag{3.49}$$

Only semiconductor diode D_2 is conducting, then;

$$V_{D_2} = 0 \tag{3.50}$$

3.2.5 Stage 5: $(t_4 \leq t \leq t_5)$

During this stage, switch S , diodes D_b and D_f are still off. Diode D_1 is turned ON and diode D_2 is keep conducted. Current flowing through diode D_2 is decreasing linearly and the maximum part of input current i_i is flowing across diode D_1 linearly. The DC input source V_i, connected in series with the input inductor L_i, both continue to charge the input capacitor C_i through diode D_1. Then, the resonant capacitor is keep charged by the magnetizing energy from the inductor L_m and the resonant inductor L_r. Output capacitors C_b and C_f continue to be constantly discharged to the load. This stage is ended when diode D_2 is turned off. The equivalent circuit of this stage is shown in Figure 3.6(b).

3.2.6 Stage 6: $(t_5 \leq t \leq t_6)$

In this stage, switch S remains off and diode D_2 is turned off, diode D_1 is still conducted and diodes D_b and D_f start to conduct. The DC input source V_i is serially connected to the input inductor L_i to charge the input capacitor C_i. The magnetizing inductor L_m continues to transfer its energy through coupled inductor to the leakage inductor L_k in the secondary winding and then to charge the output Flyback capacitor C_f. During this interval, the resonant capacitor is uncharging to the Boost output capacitor. This stage is ended when the diode D_b is turned off, in the same time, current flowing in the secondary winding of the coupled inductor reaches its peak value. The equivalent circuit of this stage is shown in Figure 3.6(c).

By applying KVL, these expressions below are obtained;

$$V_{L_i} = V_i - V_{C_i} \tag{3.51}$$

$$V_{L_m} = V_{C_i} - V_{C_b} \tag{3.52}$$

Due to the stacked connection, the output voltage V_o, is the sum of output Boost and Flyback voltages V_{C_b} and V_{C_f}, then;

$$V_{C_b} = V_o - V_{C_f} \tag{3.53}$$

By substituting (3.53) in (3.52), then;

$$V_{L_m} = V_{C_i} - \left(V_o - V_{C_f}\right) \tag{3.54}$$

Output Flyback voltage can be obtained in terms of the turn ratio N of the coupled inductor by neglecting the leakage inductor in the secondary winding.

$$V_{C_f} = -NV_{L_m} \tag{3.55}$$

By substituting (3.54) in (3.55), then;

$$V_{C_f} = \frac{N}{N+1}\left(V_o - V_{C_i}\right) \tag{3.56}$$

Then, output Boost voltage in equation (3.53) becomes;

$$V_{C_b} = \frac{V_o + NV_{C_i}}{N+1} \tag{3.57}$$

3.2.7 Stage 7: $(t_6 \leq t \leq T_s)$

The last stage of operation begins instantaneously when Boost output diode D_b is reverse biased. The switch S and diode D_2 are still off. Diodes D_1 and D_f remain conducted. Magnetizing inductor L_m continues to transfer energy to Flyback output capacitor via the coupled inductor. Resonant capacitor continues to discharge until reaching zero value. Energy stored in output capacitors C_b and C_f are discharged to the load. At the end of this stage, the switch is turned ON and then begins a new switching period. The equivalent circuit of this stage is shown in Figure 3.6(d).

3.3 VOLTAGE STRESS OF THE COMPONENTS

- Input capacitor voltage, V_{C_i};

Using equations (3.28) and (3.51), volt-second balance principle can be applied to the input inductor L_i to find the expression of the input capacitor voltage.

$$\int_0^{DT_s} V_{L_i} + \int_{DT_s}^{T_s} V_{L_i} = 0 \tag{3.58}$$

$$\int_0^{DT_s} \frac{L_i}{L_i + L_r} V_i + \int_{DT_s}^{T_s} V_i - V_{C_i} = 0 \tag{3.59}$$

$$\left(\frac{L_i}{L_i + L_r} V_i \right) DT_s + \left(V_i - V_{C_i}\right)\left(T_s - DT_s\right) = 0 \tag{3.60}$$

$$V_{C_i}\left(1 - D\right) = \left(\frac{L_i + \left(1 - D\right) L_r}{L_i + L_r} \right) V_i \tag{3.61}$$

The input capacitor voltage is obtained by equation (3.62).

$$V_{C_i} = \frac{1}{\left(1 - D\right)} \left(\frac{L_i + \left(1 - D\right) L_r}{L_i + L_r} \right) V_i \tag{3.62}$$

- Output Boost capacitor voltage, V_{C_b};

Using equations (3.30) and (3.52), volt-second balance principle can be applied to the magnetizing inductor L_m to find these following equations.

$$\int_0^{DT_s} V_{L_m} + \int_{DT_s}^{T_s} V_{L_m} = 0 \tag{3.63}$$

$$\int_0^{DT_s} \frac{L_m}{L_m + L_r} V_{C_i} + \int_{DT_s}^{T_s} V_{C_i} - V_{C_b} = 0 \tag{3.64}$$

$$\left(\frac{L_m}{L_m + L_r} V_{C_i} \right) DT_s + \left(V_{C_i} - V_{C_b}\right)\left(T_s - DT_s\right) = 0 \tag{3.65}$$

$$V_{C_b}\left(1 - D\right) = \left(\frac{L_m + \left(1 - D\right) L_r}{L_m + L_r} \right) V_{C_i} \tag{3.66}$$

By substituting (3.61) in (3.66), these expressions below are obtained

$$V_{C_b} = \frac{1}{(1-D)}\left(\frac{L_m + (1-D)\,L_r}{L_m + L_r}\right)\frac{1}{(1-D)}\left(\frac{L_i + (1-D)\,L_r}{L_i + L_r}\right)V_i \tag{3.67}$$

$$V_{C_b} = \frac{1}{(1-D)^2}\frac{[L_m + (1-D)\,L_r]\,[L_i + (1-D)\,L_r]}{(L_m + L_r)\,(L_i + L_r)}V_i \tag{3.68}$$

Then;

$$V_{C_b} = \frac{1}{(1-D)^2}\frac{(1-D)\,L_r\,[L_m + L_i + (1-D)\,L_r] + L_mL_i}{(L_m + L_r)\,(L_i + L_r)}V_i \tag{3.69}$$

- Output Flyback capacitor voltage, V_{C_f};

According to equations (3.9) and (3.52);

$$V_{C_f} = -NV_{L_m} = -N\,(V_{C_i} - V_{C_b}) \tag{3.70}$$

By substituting equations (3.62) and (3.68) in (3.71), equation (3.72) is obtained.

$$V_{C_f} = -NV_{L_m} = -N\,(V_{C_i} - V_{C_b}) \tag{3.71}$$

$$V_{C_f} = \frac{N}{(1-D)^2}\frac{[L_m + (1-D)\,L_r]\,[L_i + (1-D)\,L_r]}{(L_m + L_r)\,(L_i + L_r)}V_i - \frac{N}{(1-D)}\left(\frac{L_i + (1-D)\,L_r}{L_i + L_r}\right)V_i \tag{3.72}$$

$$V_{C_f} = \frac{N\,[L_m + (1-D)\,L_r]\,[L_i + (1-D)\,L_r] - N\,(1-D)\,(L_m + L_r)\,[L_i + (1-D)\,L_r]}{(1-D)^2\,(L_m + L_r)\,(L_i + L_r)}V_i \tag{3.73}$$

Suppose that V_{C_f} is written as;

$$V_{C_f} = \frac{\psi_1 + \psi_2}{(1-D)^2\,(L_m + L_r)\,(L_i + L_r)}V_i \tag{3.74}$$

with;

$$\psi_1 = N\,[L_m + (1-D)\,L_r]\,[L_i + (1-D)\,L_r] \tag{3.75}$$

and

$$\psi_2 = -N\left(1-D\right)\left(L_m+L_r\right)\left[L_i+\left(1-D\right)L_r\right] \tag{3.76}$$

By doing some mathematical analysis;

$$\psi_1 = NL_mL_i + NL_mL_r - NDL_mL_r + NL_rL_i + NL_r^2 - 2NDL_r^2 - NDL_rL_i + ND^2L_r^2 \tag{3.77}$$

$$\psi_1 + \psi_2 = NDL_mL_i - ND^2L_mL_r + NDL_mL_r = ND\left[L_mL_i + \left(1-D\right)L_mL_r\right] \tag{3.78}$$

By substituting equation (3.78) in (3.74), output Flyback voltage is given by equation (3.79).

$$V_{C_f} = \frac{ND}{\left(1-D\right)^2}\frac{\left[\left(1-D\right)L_mL_r + L_mL_i\right]}{\left(L_m+L_r\right)\left(L_i+L_r\right)}V_i \tag{3.79}$$

- Voltage Gain, M;

Output voltage V_o given in equation (3.80) is obtained by adding equations (3.68) and (3.79)

$$V_o = \frac{\left(1+ND\right)L_mL_i + \psi_3}{\left(1-D\right)^2\left(L_m+L_r\right)\left(L_i+L_r\right)}V_i \tag{3.80}$$

With;

$$\psi_3 = \left(1 - D + ND - ND^2\right)L_mL_r + \left(1-D\right)L_rLi + \left(1 - 2D + D^2\right)L_r^2 \tag{3.81}$$

In fact, the voltage gain is given by this expression below.

$$M = \frac{V_o}{V_i} = \frac{\left(1+ND\right)L_mL_i + \psi_3}{\left(1-D\right)^2\left(L_m+L_r\right)\left(L_i+L_r\right)} \tag{3.82}$$

- Boost diode voltage, V_{D_b};

According to the circuit topology of the the third stage of operation shown in Figure 3.5(c), KVL is applied to obtain the voltage stress of the diode D_b.

$$V_{D_b} \approx V_{C_b} = \frac{1}{\left(1-D\right)^2}\frac{\left[L_m + \left(1-D\right)L_r\right]\left[L_i + \left(1-D\right)L_r\right]}{\left(L_m+L_r\right)\left(L_i+L_r\right)}V_i \tag{3.83}$$

- Voltage stress of the switch, V_S;

By applying KVL to the circuit topology depicted by Figure 3.6(b), then;

$$V_S \approx V_{C_b} + V_{D_b} \tag{3.84}$$

According to equation 3.83, the voltage stress of the switch is expressed as;

$$V_S \approx V_{C_b} + V_{D_b} = \frac{2}{(1-D)^2} \frac{[L_m + (1-D)\,L_r]\,[L_i + (1-D)\,L_r]}{(L_m + L_r)\,(L_i + L_r)} V_i \tag{3.85}$$

- Flyback diode voltage, V_{D_f};

$$V_{D_f} = NV_{L_m} + V_{C_f} = NV_{C_i} - NV_{C_b} + V_{C_f} \tag{3.86}$$

By substituting (3.62), (3.68) and (3.79) in (3.86), The voltage stress across Flyback Diode can be obtained.

$$V_{D_f} = \frac{N}{1-D} \frac{\gamma_1 + \gamma_2 - \gamma_3}{(1-D)\,(L_m + L_r)\,(L_i + L_r)} \tag{3.87}$$

With;

$$\gamma_1 = (1-D)\,(L_m + L_r)\,[L_i + (1-D)\,L_r] \tag{3.88}$$

$$\gamma_2 = D\,[(1-D)\,L_m L_r + L_m L_i] \tag{3.89}$$

$$\gamma_3 = [L_m + (1-D)\,L_r]\,[L_i + (1-D)\,L_r] \tag{3.90}$$

Figure 3.7 shows the main waveforms of the proposed converter during a switching period T_s.

Figure 3.6 – TURN OFF Stages of operation of Quadratic ZVS Boost-Flyback converter. (a) Fourth Stage ($t_3 \leq t \leq t_4$). (b) fifth Stage ($t_4 \leq t \leq T_5$). (c) sixth Stage ($t_5 \leq t \leq T_6$). (d) seventh Stage ($t_6 \leq t \leq T_s$).

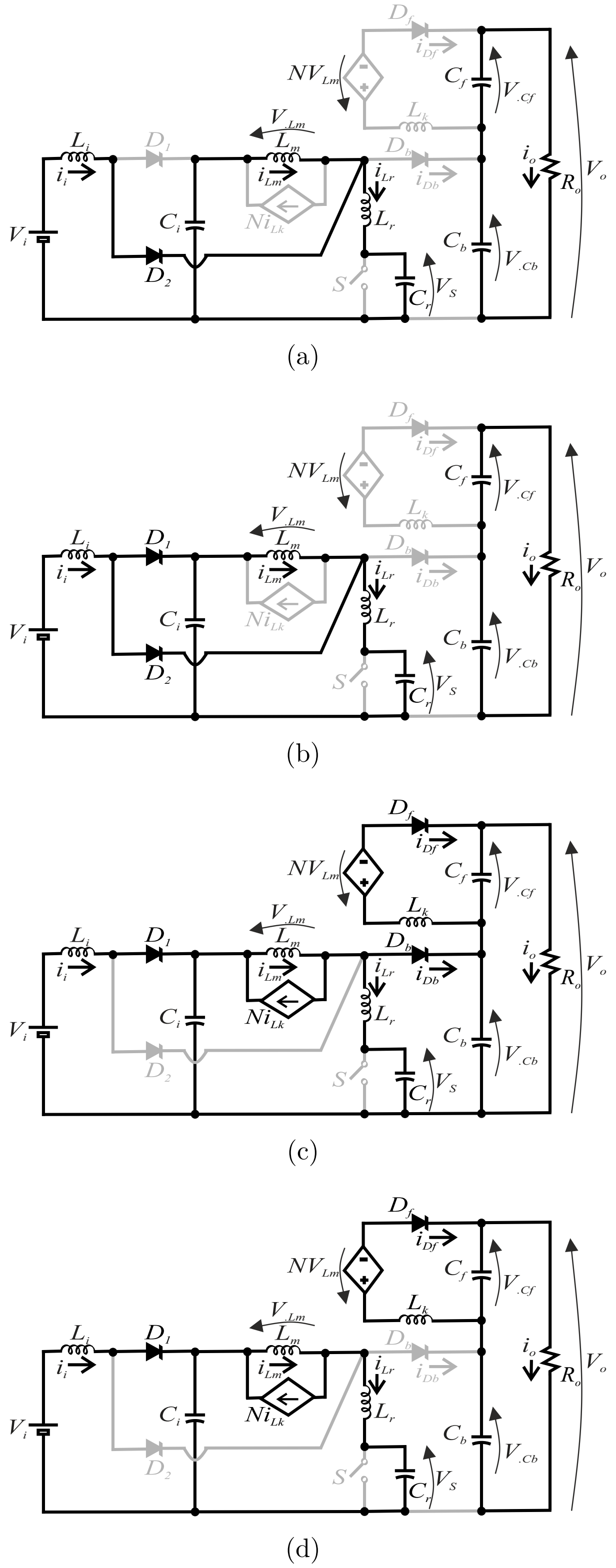

(a)

(b)

(c)

(d)

Source: Author

Figure 3.7 – Main waveforms of the QZVSBF converter during a switching period

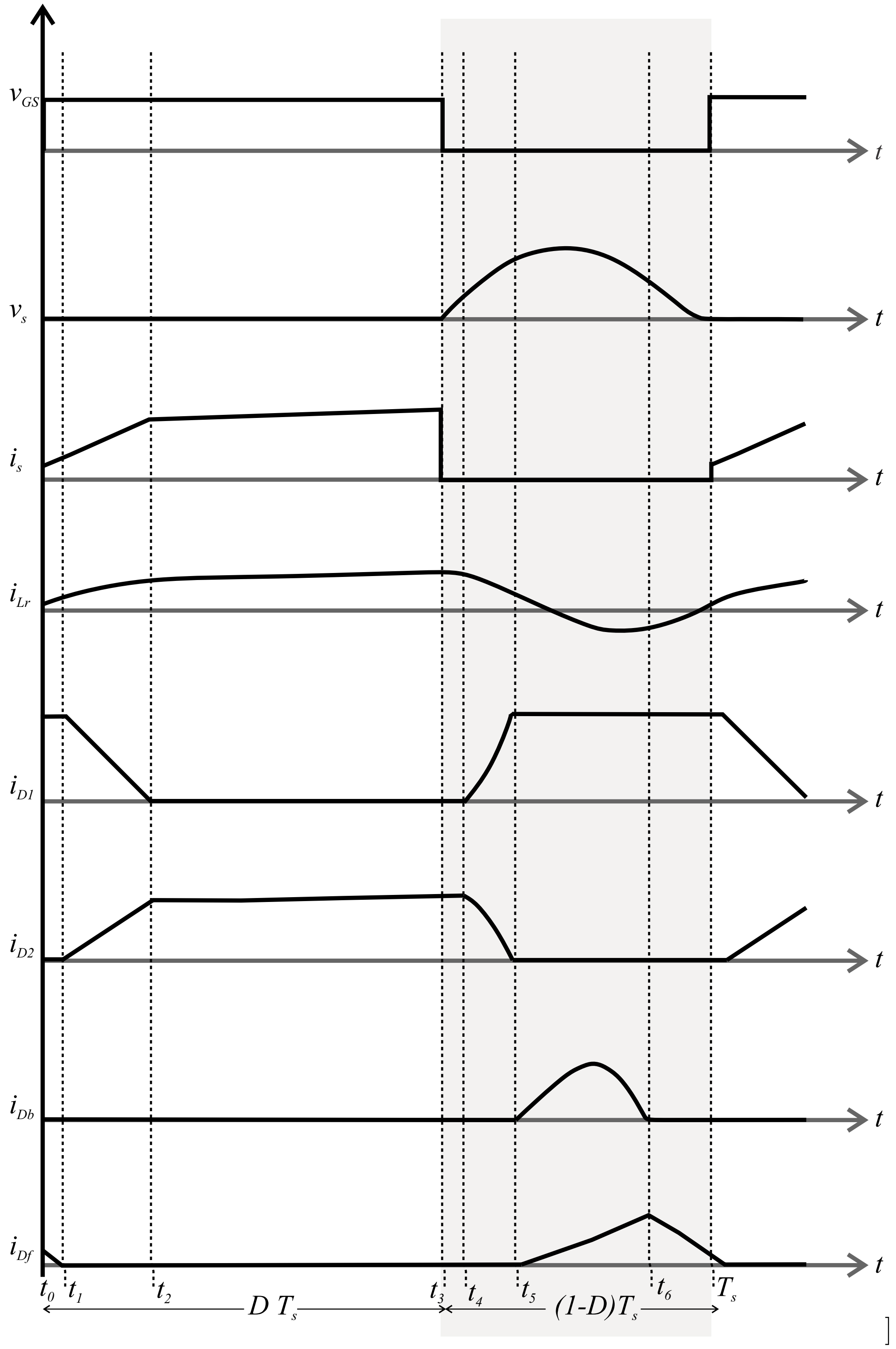

3.4 DESIGN GUIDELINES

From these data, the design specifications for the converters are defined, which are described in Table 3.1. In order to know the region in which the converter can reach the

Table 3.1 – Nominal Design Parameters of the proposed converter.

Parameter	Symbol	Value
Switching Frequency	f_s	100 kHz
Input Voltage	V_i	37,4 V
Output Voltage	V_o	400 V
Input Power	P_i	200 W
Duty Cycle	D	0,6
Turn ratio	N	3
Normalized Frequency	A	0,464

ZVS, it is necessary to initially determine some design parameters such as: The resonant frequency which will later allow to calculate the values of the resonant inductor and the resonant capacitor, the level of current flowing in the switch when it is in ON state, the magnetizing inductor and the leakage inductor. Given that some of these data are not known yet at this design stage, it will be necessary to estimate them.

Considering that the value of the normalized frequency is $A = 0.484$, by using equation (3.2), then;

$$f_r = \frac{f_s}{A} = 215686 \cdot Hz \tag{3.91}$$

To determine the resonant capacitor, it is necessary to know the resonant inductor. In this case, as the best operating point of the converter is not known, a value of the resonant inductor is just fixed. The chosen value is $L_r = 16.5 \cdot 10^{-6} H$ Therefore, the resonant capacitor will be;

$$C_r = \frac{1}{4\pi^2 f_r^2 L_r} = 33 \cdot 10^{-9} F \tag{3.92}$$

To maintain the operation of the Quadratic ZVS Boost Flyback converter of duty cycle $D = 0.6$, the value of the transformation ratio was chosen as, $N = 3$. Table 3.2 shows a summary of the component parameters defined for this design from the mathematical analysis expressions.

Table 3.2 – Simulation Parameters.

Parameter	Symbol	Value
Switching Frequency	f_s	100 kHz
Input Voltage	V_i	37,4 V
Output Voltage	V_o	400 V
Input Power	P_i	200 W
Duty Cycle	D	0,6
Turn ratio	N	3
Normalized Frequency	A	0,464
Resonant Inductor	L_r	$16.5 \cdot 10^{-6}$ H
Resonant Capacitor	C_r	$33 \cdot 10^{-9}$ F
Magnetizing Inductor	L_m	$350 \cdot 10^{-6}$ H
Output Capacitors	C_b and C_f	$9 \cdot 10^{-6}$ F
Input Inductor	L_i	$220 \cdot 10^{-6}$ H
Input Capacitor	C_i	$70 \cdot 10^{-9}$ F
Diode Voltage	D_1	$V_{max} = 100$ V
Diode Voltage	D_2	$V_{max} = 150$ V
Boost diode Voltage	D_b	$V_{max} = 200$ V
Flyback diode Voltage	D_f	$V_{max} = 500$ V
MOSFET	S	$V_{max} = 400$ V
Voltage Gain	M	10,695

3.5 PARTIAL CONCLUSION

In this chapter, the proposed Quadratic ZVS Boost-Flyback converter with coupled inductor and resonant cell has been analyzed. Operation in continuous conduction mode has been presented, the main operation steps have been analyzed and subsequently the calculation of the static gain and semiconductor voltage stresses have been performed for the proposed converter.

4 SIMULATION AND EXPERIMENTAL RESULTS

In order to evaluate and validate the analysis of the proposed converter, a prototype of the proposed converter is implemented, with specifications shown in Table 3.2. These evaluations have done for $h = 0$, as mentioned in section 3.1. The main components and parameters of the prototype converter are shown in 3.2.

4.1 SIMULATION RESULTS

To demonstrate the proposed converter achieving ZVS, the simulation results are verified by PSIM® software. Due to the resonance between L_r and C_r, at turn ON switching, it can be seen instantaneously the voltage of the switch reaches zero. At turn OFF switching, in the fourth stage of operation, Zero Current Switching (ZCS) achieves the flyback diode. Boost diode also turn off two times at turn-off switching, ZCS for Boost diode is also achieved. Consequently, with the proposed converter, the resonant circuit allows to eliminate high peak voltage stress across semiconductors, not only the ZVS across the switch at turn ON, but also across Boost and Flyback diodes.

4.1.1 Voltage and Current Through the Switch.

Figure 4.1 shows the current and voltage of the switch. The voltage reaches zero at turn On and Turn OFF, validating the ZVS region. At turn ON switching, current of the switch starts from non zero value, then, the initial resonant inductor and switch currents h defined in equation (3.3) is then non null.

Figure 4.1 – Voltage and Current of the switch.

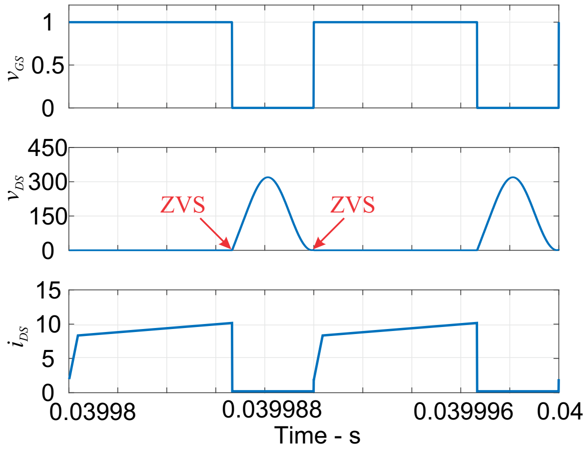

Source: Author

4.1.2 Voltage and Current Through the Boost Diode (D_b).

Figure 4.2 shows the simulation result for Current and voltage across Diode Boost D_b. Boost diode is conducting only in the sixth stage of operation and achieves ZCS at Turn ON and Turn OFF switching.

Figure 4.2 – Voltage and Current of the Boost diode D_b.

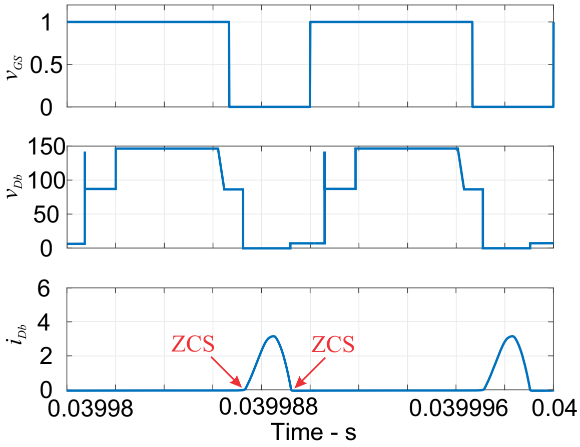

Source: Author

4.1.3 Voltage and Current of the Flyback Diode D_f

Current and voltage waveforms are shown in Figure 4.3, when the switch turns OFF, instantaneously starts the Flyback diode current from zero and its voltage achieves zero value, validating the soft switching losses.

Figure 4.3 – Voltage and Current of the Flyback diode D_f.

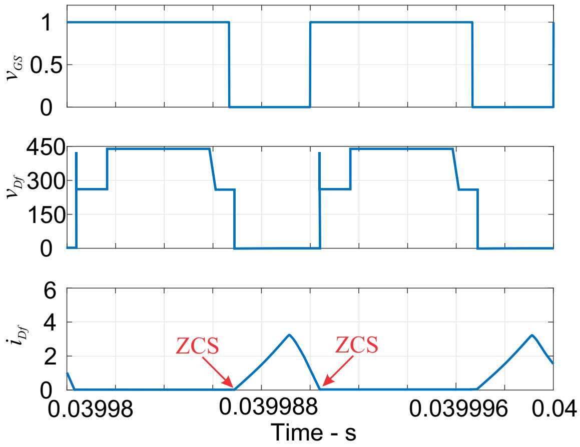

Source: Author

4.1.4 Voltage and Current of Diodes D_1 and D_2

Voltage and Current waveforms of diodes D_1 and D_2 are shown respectively by Figures 4.4 and 4.5, these diodes of the quadratic circuit prevent the resonant inductor current flowing back to the source, which could decrease the efficiency of the converter. As can be seen, all semiconductors diodes achieve ZCS, which allows the proposed converter to operate with soft switching losses.

Figure 4.4 – Voltage and Current of input diode D_1.

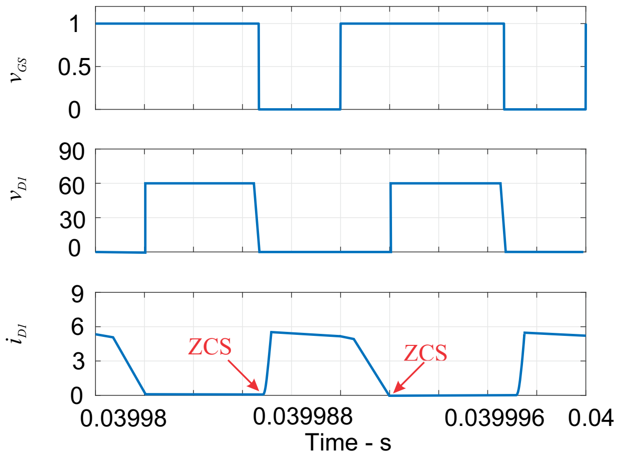

Source: Author

Figure 4.5 – Voltage and Current of input diode D_2.

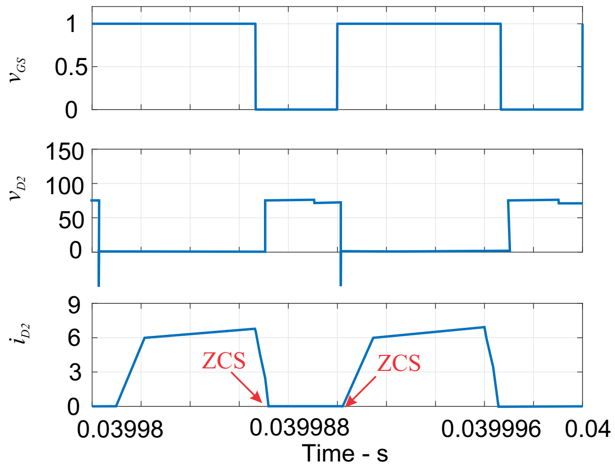

Source: Author

4.1.5 Input and Output Voltages

Input and Output voltages waveforms are shown in Figure 4.6, this converter operates with a high voltage gain, allows to step-up $37,4V$ of input voltage to $400V$ as output voltage.

Figure 4.6 – Voltage and Current of input diode D_2.

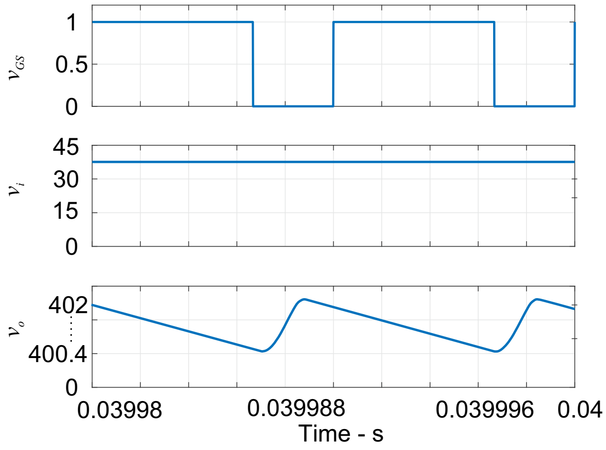

Source: Author

4.1.6 Output Boost and Flyback Capacitors

Figure 4.7 shows the Boost and Flyback output voltages. Due to the stacked connection Boost-Flyback capacitors, the output voltage of the QZVSBFC is the sum of the Boost and Flyback output voltages.

Figure 4.7 – Voltage and Current of input diode D_2.

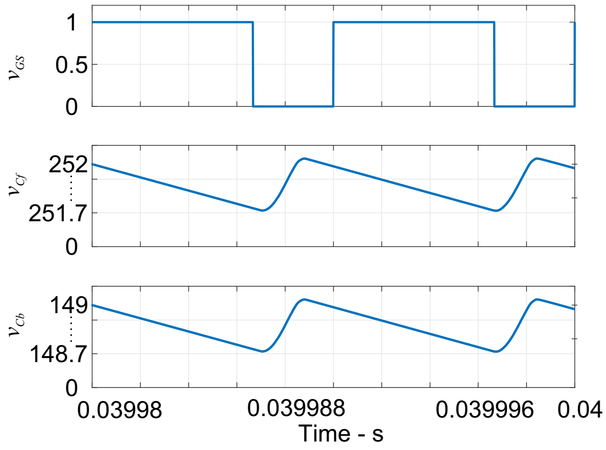

Source: Author

4.2 EXPERIMENTAL RESULTS

In the previous chapters, the study, design and simulation of the Quadratic zero voltage switching Boost Flyback converter have been done. Now, the experimental results of the proposed converter will be presented. The obtained experimental results provide the complete operation of the converter. The voltage and current waveforms of the ZVS region, the voltage waveforms on the semiconductors, the waveforms of the Boost and Flyback output voltages, the waveforms of the input voltage and the output voltage validating the static gain and the efficiency of the converter are presented. Figure 4.8 shows a picture of the prototype built for the Quadratic ZVS boost flyback converter in laboratory.

Figure 4.8 – Photo of the prototype Quadratic ZVS boost flyback converter.

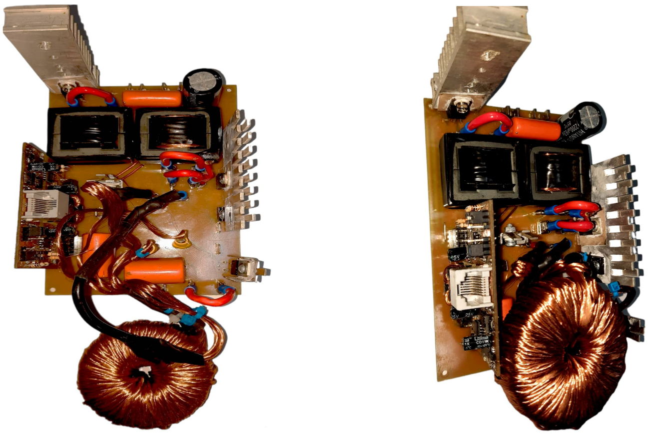

Source: Author

The following are the main waveforms of the Quadratic boost ZVS flyback converter operating with a nominal load, a duty cycle $D = 0.6$ and a switching frequency $f_s = 100$ kHz.

4.2.1 Input and Output Voltages Waveforms

Figure 4.9 shows the gate signal v_{GS} in dark blue, the input voltage v_i in light blue and the output voltage v_o in purple. As can bee seen in the figure 4.9, the input voltage is equal to 37.4 V ($10V/div$) and the output voltage reaches 400 V ($100V/div$). By dividing the output voltage and the input voltage, the proposed converter achieves the desired static gain ratio $M = 10.69$.

Figure 4.9 – Experimental waveforms of the converter: Input and output voltages.

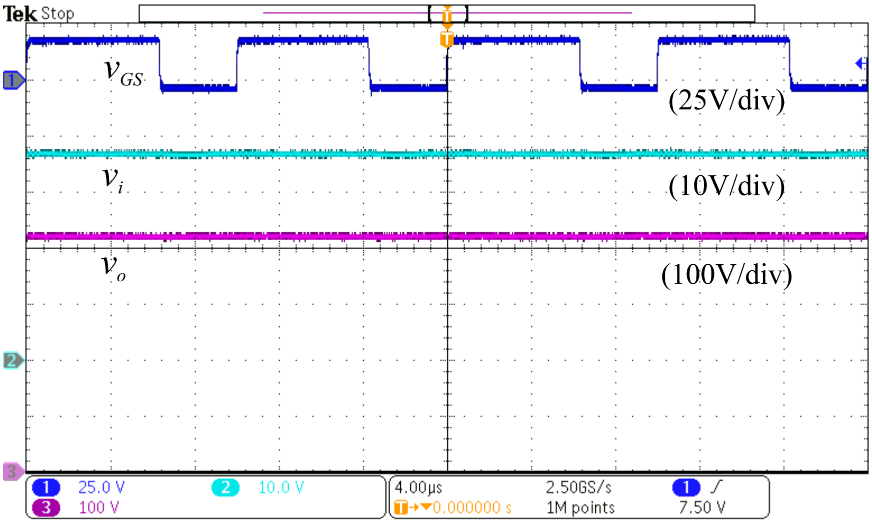

Source: Author

4.2.2 Input Capacitor, Output Boost and Flyback Capacitors Waveforms

Input capacitor voltage in dark blue v_{Ci}, output boost voltage in purple v_{Cb} and output flyback voltage in green v_{Cf} are shown in Figure 4.10. As can be seen in the figure, the output Boost capacitor reaches 251 V ($100V/div$) and the output flyback capacitor reaches 149 V ($100V/div$). The sum of v_{Cb} and v_{Cf} is equal to the output voltage v_o, thus validating the stacked connection of the proposed converter.

Figure 4.10 – Experimental waveforms of the converter: Input capacitor voltage, output boost and flyback capacitor voltage.

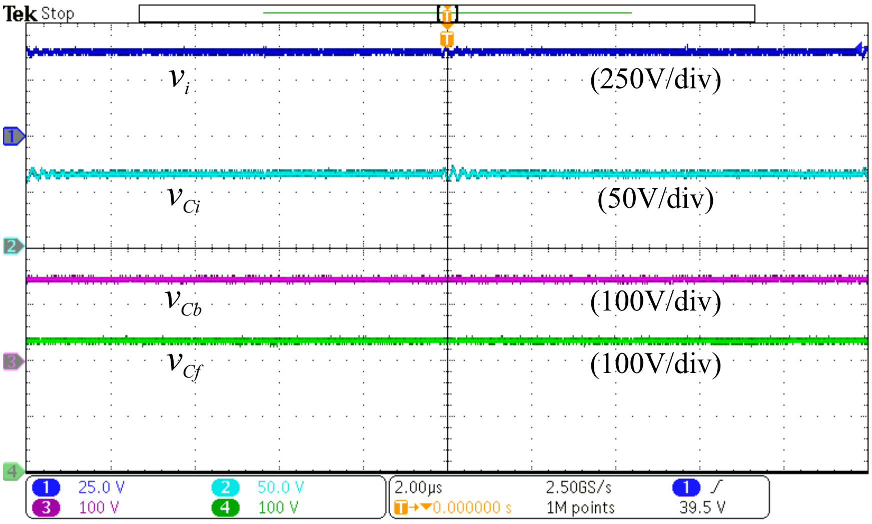

Source: Author

4.2.3 ZVS region: Switch Current and Voltage Waveforms

Figure 4.11(a) shows the PWM signal v_{GS}, the voltage and current of the switch (v_{DS} and i_{DS}) respectively in dark blue, light blue and purple. In Figure 4.11(b), at turn OFF switching, it can be observed that the voltage across the switch is zero, and at turn ON, it reaches zero value, at the same time the switch i_{DS} increases linearly from a value greater than zero, similar to the simulation result.. It is observed when the switch turns ON, the voltage is null and when it turns OFF, the current is null. Therefore the converter operates with Zero voltage switching.

Figure 4.11 – Experimental waveforms of the converter: (a) Voltage and current of the switch. (b) ZVS region at turn ON and turn OFF switching.

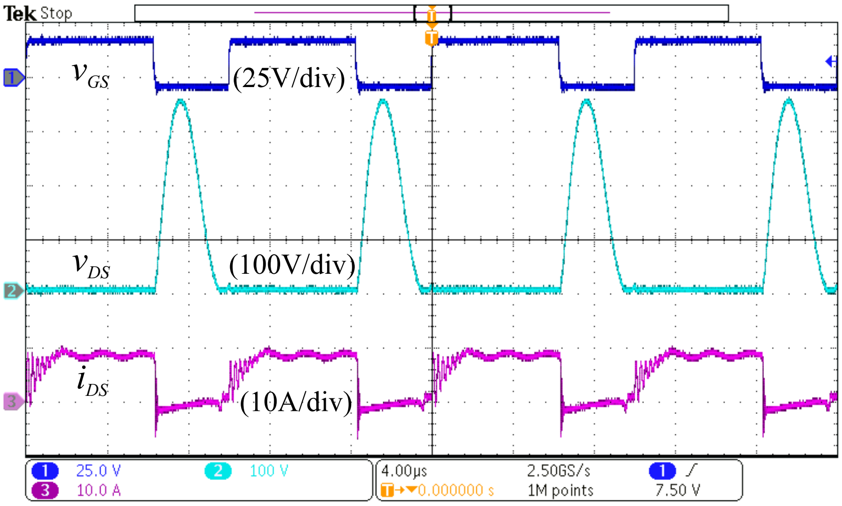

(a)

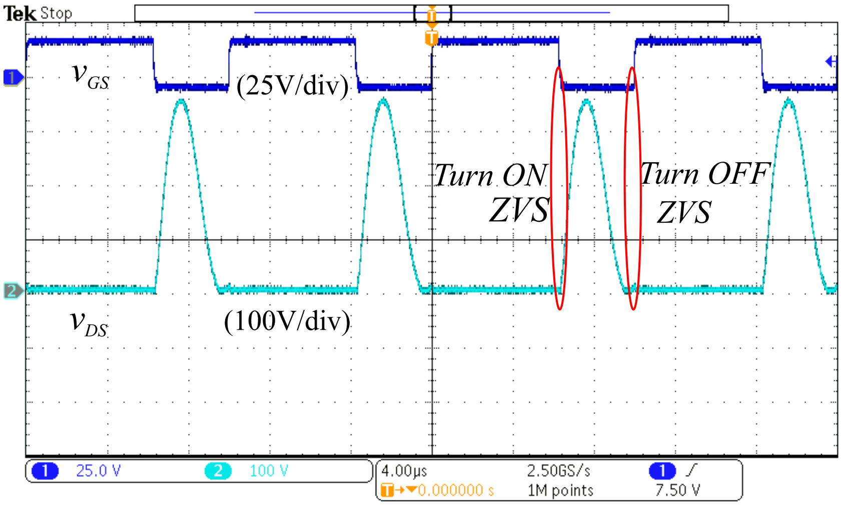

(b)

Source: Author

Figure 4.12(a) shows a zoom of i_{DS} and v_{DS} behavior at turn ON switching and Figure 4.12(b) shows their behavior at turn OFF switching.

Figure 4.12 – Experimental waveforms of the converter: (a) ZVS region at turn ON switching. (b) ZVS region at turn OFF switching.

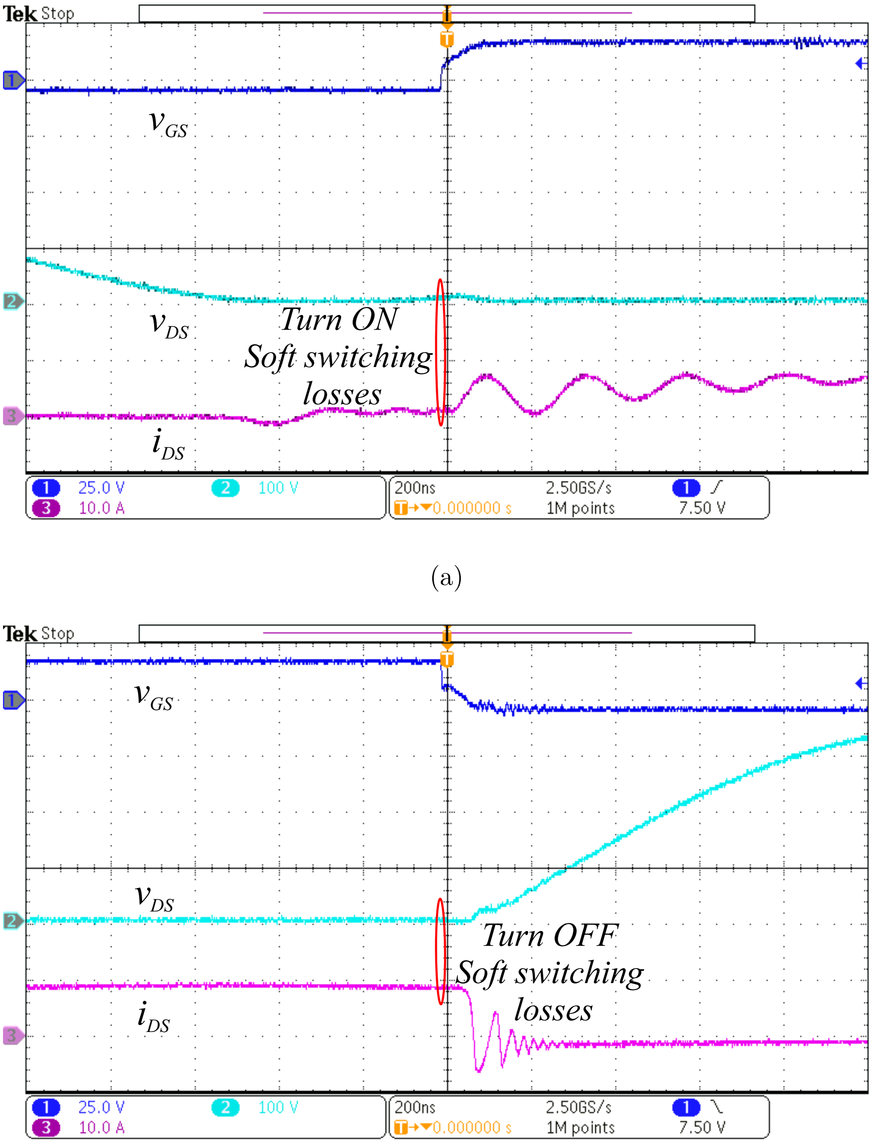

(a)

(b)

Source: Author

4.2.4 Voltage and Current Waveforms of Diodes D_b and D_f

Experimental waveforms of the voltage and current flowing through the Boost and Flyback diodes are shown in Figure 4.13(a). Boost diode voltage v_{Db} is shown in dark blue, current of boost diode i_{Db} in light blue, flyback diode voltage v_{Df} is shown in purple and current of flyback diode i_D in green. As can be seen in Figure 4.13(b), when the voltage across the diodes is different of zero, their current automatically shifts to zero as shown the ZCS regions drawn in red ellipses. Then, these behaviors allow a significant reduction of the switching losses of semiconductor diodes, hence the Zero Current switching at turn ON and turn OFF switching.

Figure 4.13 – Experimental waveforms of the converter: (a) Current and voltages of boost and flyback diodes. (b) ZCS region of semiconductors boost and flyback diodes.

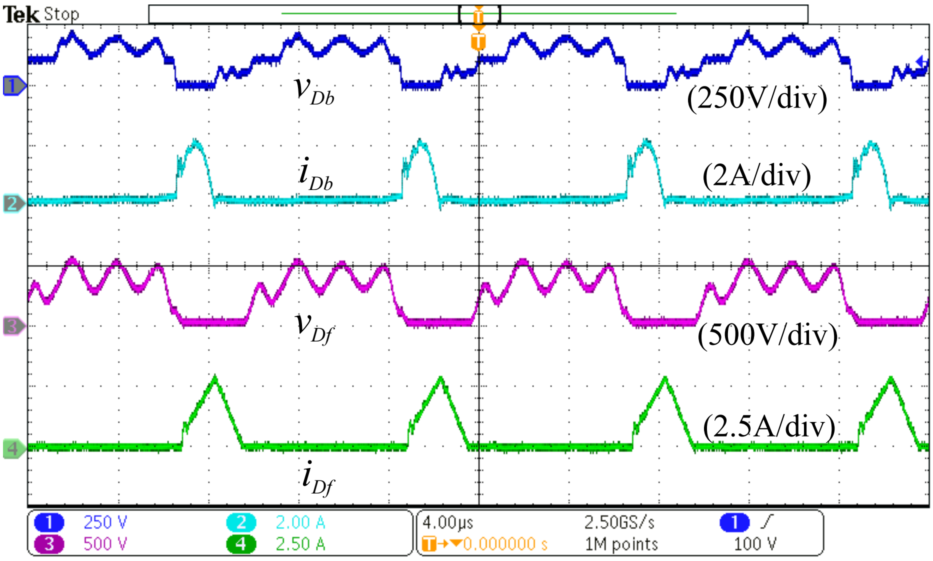

(a)

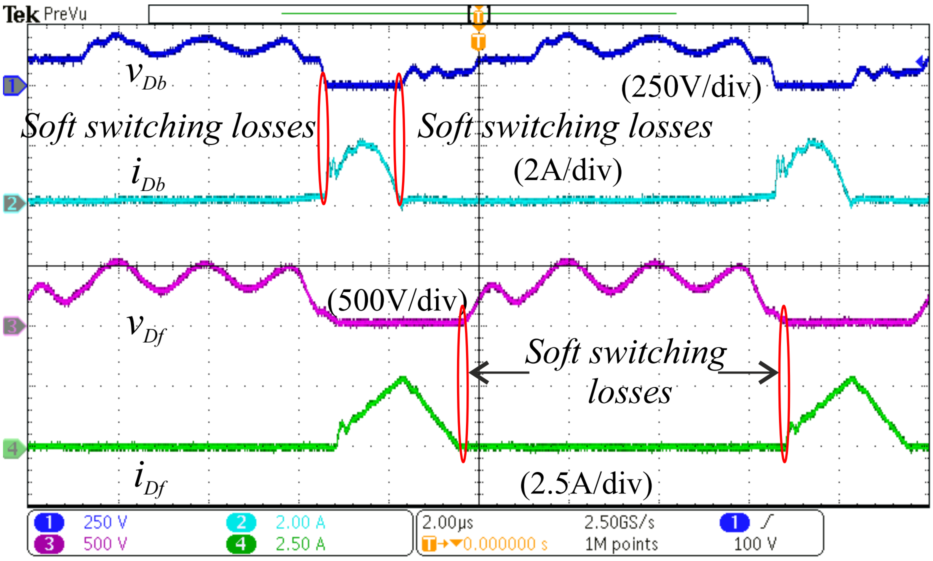

(b)

Source: Author

4.2.5 Voltage Waveforms of Diodes D_b and D_f

Figure 4.14 shows the PWM signal in dark blue, the boost diode voltage V_{Db} in light blue and the flyback diode voltage V_{Df} in purple. It can be seen that the boost diode achieves an average value of 150 V which is quasi equal to the output capacitor voltage V_{Cb}, validating the mathematical analysis and the simulation results. Regarding to the flyback diode, its average voltage is about 450 V referring to the figure 4.14.

Figure 4.14 – Experimental waveforms of the converter: (a) PWM signal, boost diode voltage and flyback diode voltage (b) PWM signal, boost diode voltage and flyback diode voltage (Zoom).

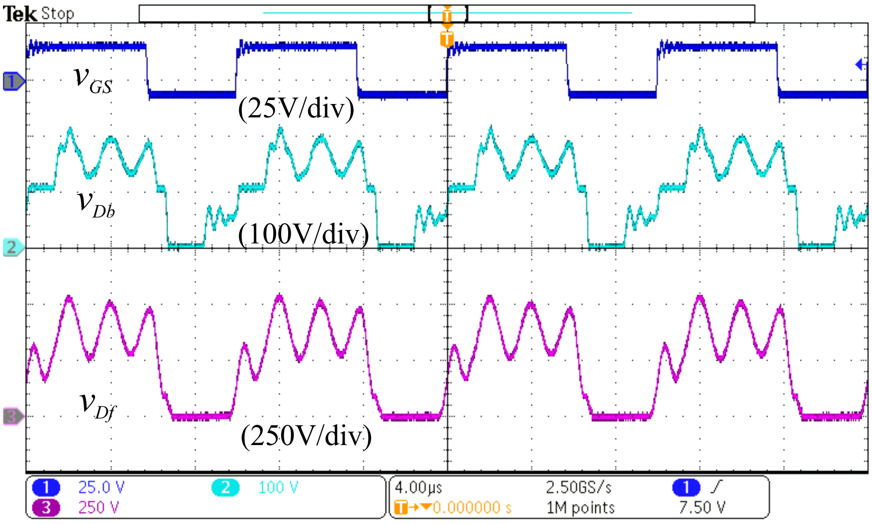

(a)

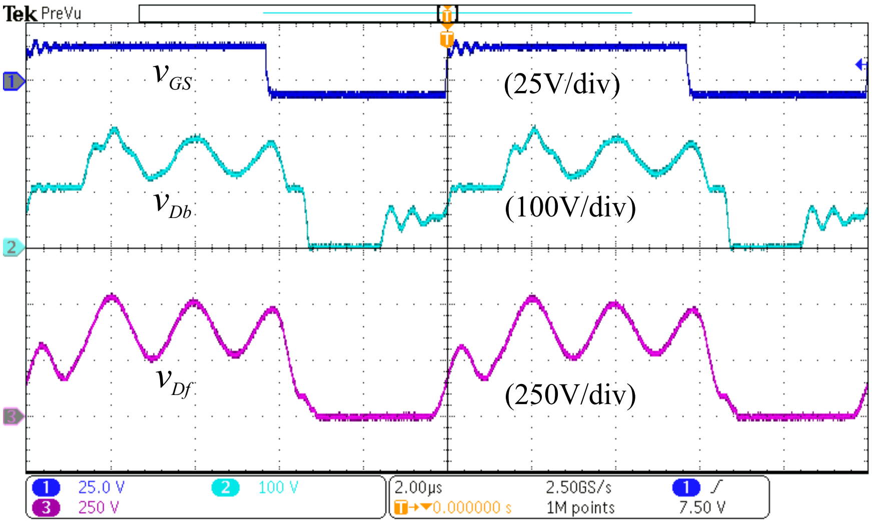

(b)

Source: Author

4.3 EFFICIENCY

To evaluate the efficiency of the proposed converter, laboratory tests were performed by varying the power. Figure 4.15 shows the efficiency curve obtained for tests ranging from 50 W to 201 W. It can be seen that for any power between 150 W and 200 W, the converter topology has an efficiency ranging from 80% to 87.7%.

Figure 4.15 – Photo of the prototype Quadratic ZVS boost flyback converter.

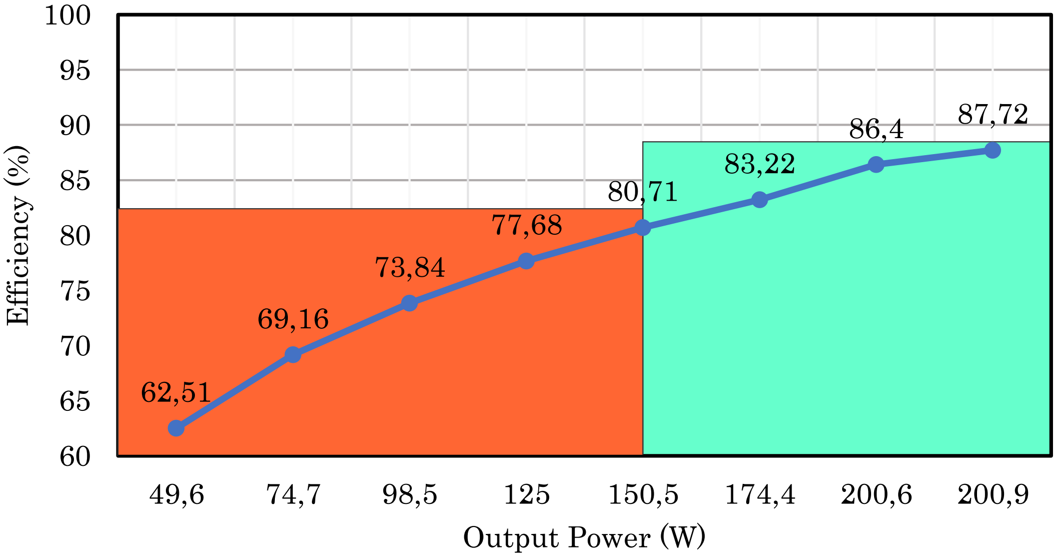

Source: Author

5 CONCLUSION

Global warming is the most pressing environmental challenge of the 21st century due to the growth in global energy demand and the world's continued dependence on fossil fuels as energy sources. As a result, demand is likely to increase as the world's population grows and greenhouse gas levels continue to rise steadily in the atmosphere and warm the Earth. As a result, to avoid the continued rise in temperature that can lead to the destruction of ecosystems and the extinction of species around the world, clean and renewable energy sources are becoming more common. Among these renewable energies, solar energy is an abundant and inexhaustible resource that can meet a large part of the planet's energy demands and has therefore been the subject of scientific attention for many years. However, the conversion of solar energy into usable electrical energy is a formidable technical and economic challenge. Generally, the output voltages of power sources are low, despite the fact that most of their loads require a high voltage level. Therefore, a high gain DC-DC converter is needed in these systems not only to increase their output voltage to the appropriate value but also needs to be improved to offer high efficiency and power density at low cost.

The basic topology which started this work was the configuration of the stacked Boost-Flyback converter with a resonant cell shown in Figure 2.9, and it was all evaluated and designed, but in practice there was a return of current to the input.

But, by adding an input boost cell, an improvement of the Boost-Flyback converter with only one resonant cell was achieved. Besides finding difficulties in the most basic Boost-Flyback converter, was able to improve it to have a very interesting topology.

So, this input boost cell will prevent the current from resonant inductot L_r flowing back to the input. So, this inductor L_r starts to reprocess energy and then some losses are generated. The main losses are located in the resonant inductor L_r, due to the high maximum current, and because of the reprocessing of energy by inverting the current that will flow through it.

Some issues observed on the board in the lab need to be improved, such as the jumpers used to make current measurements, which created parasitic inductances in the circuit and thus affected the resonance, and also generated low transient voltages. Several inductors were designed, both resonant and coupled inductors, to find the best operating point and allowed to reach both ZVS in the switch and ZCS in diodes.

Once all theoretical analyses were developed and validated, a 200W prototype was designed and built for testing. After testing, it was found that the experimental results were consistent with the simulation results obtained from PSIM® software. The prototype converter achieved a high voltage gain about 10.7 and showed an efficiency of 88% in terms of performance.

5.1 PROPOSAL FOR FUTURE WORK

- Change the passive resonant cell to an active cell to allow the converter working over all power ranges with soft-switching.
- Remove the resonant inductor L_r and replace it by the leakage inductor of the primary winding of the coupled inductor in order to resonate with capacitor C_r to increase the efficiency of the proposed converter.

REFERENCES

ABRAMOVITZ, A.; SHMILOVITZ, D. Short survey of architectures of photovoltaic arrays for solar power generation systems. **Energies**, v. 14, n. 16, Aug. 2021.

AHMAD, S.; SINGH, K. P. Simulation of step down/step-up converter implemented with zcs soft switching. **VSRD International Journal of Electrical, Electronics & Communication Engineering**, v. 2, p. 695–704, 2012.

ALLUHAYBI, K.; BATARSEH, I.; HU, H. Comprehensive review and comparison of single-phase grid-tied photovoltaic microinverters. **IEEE JOURNAL OF EMERGING AND SELECTED TOPICS IN POWER ELECTRONICS**, v. 8, n. 2, p. 1310–1329, Jun. 2020.

ANDRADE, A. M. S. S.; MARTINS, M. L. da S. Quadratic-boost with stacked zeta converter for high voltage gain applications. **IEEE JOURNAL OF EMERGING AND SELECTED TOPICS IN POWER ELECTRONICS**, v. 5, n. 4, p. 1787–1796, Dec 2017.

ANDRADE, A. M. S. S.; SCHUCH, L.; MARTINS, M. L. da S. High step-up pv module integrated converter for pv energy harvest in freedm systems. **IEEE Transactions on Industry Applications**, v. 53, n. 2, p. 1138 – 1148, Mar.-Apr. 2017.

ANSARI, S. A.; MOGHANI, J. S.; MOHAMMADI, M. Analysis and implementation of a new zero current switching flyback inverter. **International Journal of Circuit Theory and Applications**, v. 47, n. 1, p. 103–132, 2019.

AXELROD, B.; BERKOVICH, Y.; IOINOVICI, A. Switched-capacitor/switched-inductor structures for getting transformerless hybrid dc–dc pwm converters. **IEEE Transactions on Circuits and Systems**, v. 55, n. 2, p. 687–696, Mar. 2008.

AYADI, F.; COLAK, I. G. I.; BULBUL, H. I. Impacts of renewable energy resources in smart grid. **8th International Conference on Smart Grid**, p. 183–188, Jun. 2020.

BELT, J.; KASHI, J. M. B.; ALLIEN, N. Analyse coûts-avantages de la réforme du secteur de l'énergie en haïti. **Copenhagen Consensus Center**, p. 1–44, Apr. 2017.

BOURAIOU, A. et al. Analysis and evaluation of the impact of climatic conditions on the photovoltaic modules performance in the desert environment. **Energy conversion and management**, v. 106, p. 1345–1355, Nov. 2015.

BRITISH PETROLEUM. Londres, UK, 2021. Disponível em: <https://www.bp.com/en/global/corporate/energy-economics/statistical-review-of-world-energy.html>. Acesso em: January 15, 2022.

CHEN, S. M.; LIANG, L. S. Y. T. J.; CHEN, J. F. A boost converter with capacitor multiplier and coupled inductor for ac module application. **IEEE Transactions on Industrial Electronics**, v. 60, n. 4, p. 1503–1511, Sep. 2011.

CHEN, Y.; SMEDLEY, K. A cost-effective single-stage inverter with maximum power point tracking. **IEEE Transactions on Power Electronics**, v. 19, n. 5, p. 1289–1294, Sep. 2004.

CUBAS, J.; PINDADO, S.; VICTORIA, M. On the analytical approach for modeling photovoltaic systems behavior. **Journal of Power Sources**, v. 247, p. 467–474, Sep. 2014.

DABO, G. et al. Global supply-chain effects of covid-19 control measures. **Nature Human Behaviour**, v. 4, p. 577–587, Jun. 2020. Disponível em: <https://www.nature.com/articles/s41562-020-0896-8.pdf>.

DABOU, R. et al. Monitoring and performance analysis of grid connected photovoltaic under different climatic conditions in south algeria. **Energy conversion and management**, v. 130, p. 200–206, Nov. 2016.

DANIEL, M.; ULI, J. Keeping cool with the sun. **International Sustainable Energy Review**, v. 6, p. 28–30, 2012.

DEMIRBAS, A. Potential applications of renewable energy sources, biomass combustion problems in boiler power systems and combustion related environmental issues. **Progress in Energy and Combustion Science**, v. 31, p. 171–192, 2005.

DICKERMAN, L.; HARRISON, J. A new car, a new grid. **IEEE Power and Energy Magazine**, v. 8, p. 55–61, Mar. 2010. ISSN 1540-7977.

FAYE, M. M. Cadre de gestion environnementale et sociale. projet de renforcement du secteur de l'energie et d'expansion de l'accès en haïti. **MTPTC/EDH, Haiti**, 2012.

GOETZBERGERA, A.; HEBLINGA, C.; SCHOCKB, H.-W. Photovoltaic materials, history, status and outlook. **Materials Science and Engineering R**, p. 1–46, 2003.

GRIGSBY, L. L.; HARLOW, J. H.; MCDONALD, J. D. **Electric Power Generation, Transmission and Distribution**. 3. ed. Boca Raton: Taylor & Francis Group, LLC, 2011. 769 p. ISBN 978-1-4398-5637-6.

HAITILIBRE. Port-au-Prince, HTI, 2018. Disponível em: <https://www.haitilibre.com/article-23665-haiti-politique-haiti-a-les-taux-deconsommation-d-electricite-les-plus-bas-au-monde.html>. Acesso em: April 19, 2022.

HAIZHU, Y.; JIE, L. Research on maximum power point tracking control based on the low power photovoltaic grid-connected inverter. **IEEE 6th International Power Electronics and Motion Control Conference**, p. 2165–2169, 2009.

HOOGWIJK, M.; GRAUS, W. **Global potential of renewable energy sources: a literature assessment**. Paris: REN21 - Renewable Energy Policy Network for the 21st Century, 2008. 45 p.

HUANG, D.; FU, D.; LEE, F. C. Classification and selection methodology for multi-element resonant converters. **2011 Twenty-Sixth Annual IEEE Applied Power Electronics Conference and Exposition (APEC)**, p. 558–565, Mar. 2011.

HUI, S.; CHENG, K. E.; PRAKASH, S. N. A fully soft switched extended-period quasi-resonant power-factor correction circuit. **IEEE transactions on power electronics**, v. 12, n. 5, p. 922–930, 1997.

INTERNATIONAL ENERGY AGENCY. Paris, France, 2010. Disponível em: <https://iea.blob.core.windows.net/assets/1b090169-1c58-4f5d-9451-ee838f6f00e5/weo2010.pdf>. Acesso em: January 27, 2022.

_____. Paris, France, 2012. Disponível em: <https://iea.blob.core.windows.net/assets/ebe15dfb-30c8-42cf-8733-672b3500aed7/WEO2012_free.pdf>. Acesso em: January 26, 2022.

INTERNATIONAL ENERGY AGENCY - PHOTOVOLTAIC POWER SYSTEMS PROGRAMME. Paris, France, 2001. Disponível em: <https://iea-pvps.org/annual-reports/annual-report-test-1/annual-report-test-2/>. Acesso em: February 2, 2022.

INTERNATIONAL RENEWABLE ENERGY AGENCY. Abu Dhabi, UAE, 2021. Disponível em: <https://irena.org/-/media/Files/IRENA/Agency/Publication/2021/Aug/IRENA_Renewable_Energy_Statistics_2021.pdf>. Acesso em: January 18, 2022.

JAHANGIRI, H.; MOHAMMADPOUR, S.; AJAMI, A. A high step-up dc-dc boost converter with coupled inductor based on quadratic converters. **9th Annual Power Electronics, Drives Systems and Technologies Conference (PEDSTC)**, p. 20–25, Feb. 2018.

JAIN, S.; AGARWAL, V. A single-stage grid connected inverter topology for solar pv systems with maximum power point tracking. **IEEE Transactions on Power Electronics**, v. 2, n. 5, p. 1928–1940, Sep. 2007.

KASA, N.; LIDA, T.; CHEN, L. Flyback inverter controlled by sensorless current mppt for photovoltaic power system. **IEEE Transactions on Industrial Electronics**, v. 52, n. 4, p. 1145–1152, Aug. 2005.

KENNERUD, K. L. Analysis of performance degradation in cds solar cells. **IEEE TRANSACTIONS ON AEROSPACE AND ELECTRONIC SYSTEMS**, v. 5, n. 6, p. 912–917, Nov. 1969.

KHATIB, H. Trends and future demand for electric power generation. **IEE International Conference on Opportunities and Advances in International Power Generation**, n. 419, Mar. 1996.

KJAER, S. B.; PEDERSEN, J. K.; BLAABJERG, F. A review of single-phase grid-connected inverters for photovoltaic modules. **IEEE TRANSACTIONS ON INDUSTRY APPLICATIONS**, v. 41, n. 5, p. 1292–1306, Sep. 2005.

LEYVA-RAMOS, J.; ORTIZ-LOPEZ, L. D.-S. M.; MORALES-SALDAñA, J. Switching regulator using a quadratic boost converter for wide dc conversion ratios. **IET Power Electronics**, v. 2, n. 5, p. 605–613, Sep. 2009.

LISERRE, M.; TEODORESCU, R.; BLAABJERG, F. Stability of grid-connected pv inverters with large grid impedance variation. **35th IEEE Annual Power Electronics Specialists Conference**, v. 6, p. 4773–4779, Jun. 2004.

LIU, H.; AIAND, J.; LI, F. A novel high step-up converter with a switched-coupled-inductor capacitor structure for sustainable energy system. **Journal of Power Electronics**, v. 16, n. 2, p. 436–446, Mar. 2016.

LIU, H. et al. Overview of high-step-up coupled-inductor boost converters. **IEEE Journal of Emerging and Selected Topics in Power Electronics**, v. 4, n. 2, p. 689–704, Jun. 2016.

MALEWSKI, R. et al. Instruments for hv insulation testing in substations. **CIGRE-2000**, v. 33, n. 12, Aug. 2000.

MARTINS, D.; DEMONTI, R. Grid connected pv system using two energy processing stages. **29th IEEE Photovoltaic Specialists Conference, 2002.**, p. 1649–1652, Apr. 2003. ISSN 1060-8371.

MEINHARDT, M.; CRAMER, G. Past, present and future of grid connected photovoltaic and hybrid power systems. **Power Engineering Society Summer Meeting**, v. 2, p. 1283–1288, Jul. 2000.

MINISTèRE DES TRAVAUX PUBLICS, TRANSPORTS ET COMMUNICATIONS. Port-au-Prince, HTI, 2006. Disponível em: <http://www.bme.gouv.ht/energie/Haiti%20Plan%20National%20d'EnergieVRFrenchR1.pdf>. Acesso em: April 19, 2022.

MYRZIK, J. M. A.; CALAIS, M. String and module integrated inverters for single-phase grid connected photovoltaic systems - a review. **IEEE Bologna Power Tech Conference Proceedings**, v. 2, Jun. 2003.

NAVEEN R.AND P. P. REVANKAR, S. R. Integration of renewable energy systems for optimal energy needs- a review. **International Journal of Renewable Energy Research**, v. 10, n. 2, Jun. 2020.

OJO, A. A.; AWOGBEMI, O.; OJO, A. O. An overview of the exploitation of renewable energy resources in nigeria, south africa, and the united kingdom. **INTERNATIONAL JOURNAL of RENEWABLE ENERGY RESEARCH**, v. 10, n. 2, p. 843–860, Jun. 2020.

ORGANIZATION FOR ECONOMIC COOPERATION AND DEVELOPMENT. Paris, FR, 2011. Disponível em: <https://www.oecd-ilibrary.org/development/development-co-operation-report-2011_dcr-2011-en>. Acesso em: January 15, 2022.

_____. Paris, FR, 2012. Disponível em: <https://read.oecd-ilibrary.org/development/development-co-operation-report-2012_dcr-2012-en#page12>. Acesso em: January 15, 2022.

PATIDAR, K.; C.UMARIKAR, A. High step-up converters based on quadratic boost converter for micro-inverter. **Electric Power Systems Research**, v. 119, p. 168–177, Feb. 2015.

PAULA, A. N.; PEREIRA, W. J. d. P. Dênis de C.; TOFOLI, F. L. 11th ieee/ias international conference on industry applications. **11th IEEE/IAS International Conference on Industry Applications**, Dec. 2014.

RINA. Washington DC, USA, 2019. Disponível em: <http://www.ute.gouv.ht/bm/documents/SEA_FINAL_002.pdf>. Acesso em: January 15, 2022.

SAADAT, P.; ABBASZADEH, K. A single switch high step up dc-dc converter based on quadratic boost. **IEEE TRANSACTIONS ON INDUSTRIAL ELECTRONICS**, v. 63, n. 12, p. 7733–7742, Dec 2016.

SAVAKHANDE, V. B.; BHATTAR, C. L.; BHATTAR, P. L. Voltage-lift dc-dc converters for photovoltaic application-a review. **International Conference on Data Management, Analytics and Innovation (ICDMAI)**, p. 172–176, Feb. 2017.

SHIMIZU, T.; WADA, K.; NAKAMURA, N. Flyback-type single-phase utility interactive inverter with power pulsation decoupling on the dc input for an ac photovoltaic module system. **IEEE Transactions on Power Electronics**, v. 21, n. 5, p. 1264–1272, Sep. 2006.

SHINJO, F.; WADA, K.; SHIMIZU, T. A single-phase grid-connected inverter with a power decoupling function. **IEEE Power Electronics Specialists Conference**, p. 1245–1249, Oct. 2007.

TABISZ, W.; LEE, F. Zero-voltage-switching multiresonant technique-a novel approach to improve performance of high-frequency quasi-resonant converters. **IEEE Transactions on Power Electronics**, v. 4, n. 4, p. 450–458, Oct. 1989.

TOMASZUK, A.; KRUPA, A. High efficiency high step-up dc/dc converters – review. **Bulletin of the Polish Academy of Sciences, Technical Sciences**, Dec. 2011.

UNITED NATIONS ENVIRONMENT PROGRAMME. Nairobi, Kenya, 2020. Disponível em: <https://www.unep.org/fr/emissions-gap-report-2020>. Acesso em: January 20, 2022.

VITHAYATHIL, J. **Power Electronics: Principles and Applications**. New York: McGraw-Hill Education (ISE Editions), 1995. 632 p. ISBN 978-0070675551.

VLATKOVIC, V. Alternative energy: State of the art and implications on power electronics. **Nineteenth Annual IEEE Applied Power Electronics Conference and Exposition**, v. 1, p. 45–50, Feb. 2004.

WALKER, G. R.; PIERCE, J. C. Photovoltaic dc-dc module integrated converter for novel cascaded and bypass grid connection topologies — design and optimization. **37th IEEE Power Electronics Specialists Conference**, Jun. 2006.

WANG, Y.-J.; HSU, P.-C. An investigation on partial shading of pv modules with different connection configurations of pv cells. **Energy**, v. 36, p. 3069–3078, May 2011.

WIJERATNE, D. S.; MOSCHOPOULOS, G. Quadratic power conversion for power electronics: principles and circuits. **EEE TRANSACTIONS ON CIRCUITS AND SYSTEMS**, v. 59, n. 2, p. 426–438, Feb. 2012.

WILLIAMS, J. W.; JACKSON, S. T.; KUTZBACH, J. E. Projected distributions of novel and disappearing climates by 2100 ad. **PNAS**, v. 104, n. 14, p. 5738–5742, Apr. 2007.

WOLF, M.; RAUSCHENBACH, H. Series resistance effects on solar cell measurements. **Advanced Energy Conversion**, v. 3, p. 455–479, 1963.

YOGESH, R. N.; THORAT, A. R. A review on photovoltaic module based grid connected power inverter. **International Conference on Power, Energy and Control (ICPEC)**, p. 272–276, Feb. 2013.

ZHAO, Q.; LEE, F. High-efficiency, high step-up dc-dc converters. **IEEE Transactions on Power Electronics**, v. 18, n. 1, p. 65–73, Jan. 2003.